N74-18152

NASA CR-121264
AiResearch 73-9489

APPLICATION OF HOLOGRAPHY TO FLOW VISUALIZATION WITHIN ROTATING COMPRESSOR BLADE ROW

Final Report

February 1974

by R.F. Wuerker, R.J. Kobayashi, L.O. Heflinger, and T.C. Ware

AIRESEARCH MANUFACTURING COMPANY,
A DIVISION OF
THE GARRETT CORPORATION
Los Angeles, California

Prepared for

NATIONAL AERONAUTICS AND SPACE ADMINISTRATION

Lewis Research Center
Contract NAS 3-15336

1. Report No.
NASA CR-121264

2. Government Accession No.

3. Recipient's Catalog No.

4. Title and Subtitle
APPLICATION OF HOLOGRAPHY TO FLOW VISUALIZATION WITHIN ROTATING COMPRESSOR BLADE ROW

5. Report Date
February 1974

6. Performing Organization Code

7. Author(s)
R. F. Wuerker, R. J. Kobayashi, L. O. Heflinger, and T. C. Ware

8. Performing Organization Report No.
73-9489

10. Work Unit No.

9. Performing Organization Name and Address
AiResearch Manufacturing Company
A Division of The Garrett Corporation
Los Angeles, California 90509

11. Contract or Grant No.
NAS 3-15336

12. Sponsoring Agency Name and Address
National Aeronautics and Space Administration
Washington, D. C. 20546

13. Type of Report and Period Covered
Contractor Report

14. Sponsoring Agency Code

15. Supplementary Notes
Project Manager, E. E. Bailey, Fluid System Components Division
NASA-Lewis Research Center, Cleveland, Ohio 44135

16. Abstract

Two holographic interblade row flow visualization systems were designed to determine the three-dimentional shock patterns and velocity distributions within the rotating blade row of a transonic fan rotor utilizing the techniques of pulsed laser transmission holography. Both single- and double-exposure bright-field holograms and dark-field scattered-light holograms were successfully recorded. Two plastic windows were installed in the rotor tip casing and outer casing forward of the rotor to view the rotor blade passage. The viewing angle allowed detailed investigation of the leading-edge shocks and shocks in the midspan damper area; limited details of the trailing edge shocks also were visible. A technique was devised for interpreting the reconstructed holograms by constructing three-dimensional models that allowed identification of the major shock systems. The models compared favorably with theoretical predictions and results of the overall and detail blade element data. Most of the holograms were made using the rapid double-pulse technique. For fan speeds greater than 90 percent of design, the holograms showed the passage shock emanating from the blade leading edge and a conical shock originating at the intersection of the midspan damper leading edge and the blade suction surface. A second damper shock, which appeared to emanate from the intersection of the midspan damper and the pressure surface of the blade, was observed on some of the holograms. The shocks associated with the midspan damper were not considered in the rotor design. Scattered-light holography techniques were found to provide meaningful qualitative velocity measurements. Static pressure contours obtained from high-response tip pressure transducers were in accord with shock patterns defined by the hologram.

The rotor used for this study was that of the transonic fan stage designed and tested for a program on a "High-Tip-Speed, Low-Loading Transonic Fan Stage" under NASA Contract NAS 3-13498.

17. Key Words (Suggested by Author(s))
Flow Visualization
Holography
Three-Dimensional Shock Patterns

18. Distribution Statement
Unclassified-unlimited

19. Security Classif. (of this report)	20. Security Classif. (of this page)	21. No. of Pages	22. Price*
Unclassified	Unclassified	132	

* For sale by the National Technical Information Service, Springfield, Virginia 22151

FOREWORD

The pulsed laser holographic technique discussed in this report was applied to a high-tip-speed, low-loading transonic fan stage designed and tested for NASA Lewis Research Center by the AiResearch Manufacturing Company of California, a division of The Garrett Corporation. The holographic work was conducted by the Optical Elements Group of TRW Systems, El Segundo, California, under subcontract to AiResearch.

Messrs. R. J. Kobayashi and T. C. Ware are affiliated with the AiReseach Manufacturing Company. Dr. R. F. Wuerker and Dr. L. O. Heflinger are affiliated with TRW systems. Mr. E. E. Bailey of NASA Lewis Research Center Fluid Systems Components Division was project manager.

Page intentionally left blank

TABLE OF CONTENTS

TABLE OF CONTENTS (Continued)

LIST OF ILLUSTRATIONS

LIST OF ILLUSTRATIONS (Continued)

LIST OF ILLUSTRATIONS (Continued)

SUMMARY

Two holographic interblade row flow visualization systems were designed to determine the three-dimensional shock patterns and velocity distributions within the rotating blade row of a transonic fan rotor operating at a tip speed of 1600 ft/sec (488.6 m/sec). The systems utilized the techniques of pulsed laser transmission holography. Both single- and double-exposure bright-field holograms and dark-field scattered-light holograms were successfully recorded. Double-exposure holograms were of both short pulse modes for which laser pulse separation varied from 2 to 5 μsec, and long pulse modes, for which separation varied from 5 to 7 min.

The rotor utilized for this study was that of a transonic fan stage designed and tested under NASA contract NAS 3-13498. The stage is a low-loading, high-tip-speed fan designed with weak oblique shocks at the rotor tip to minimize losses. The only modification to the rig structure was the installation of two Plexiglas windows, one over the rotor tip casing and the other in the outer casing forward of the rotor. The view of the rotor blade passage included the area from the blade leading edge to trailing edge, forward and around the midspan damper, and across the blade tip. The viewing angle allowed detailed investigation of the leading-edge shocks and shocks in the midspan damper area; limited details of the trailing-edge shocks also were visible.

A technique for interpreting the reconstructed holograms was devised, and models were constructed of the major shock systems identified. The models compared favorably with theoretical predictions and results of the overall and detail blade element data. Most of the holograms were made using the rapid double-pulse technique. During rapid double pulsing, the shock fringes moved slightly, thereby enhancing display of the shock patterns. For speeds greater than 90 percent of design, the holograms showed the passage shock emanating from the blade leading edge and a conical shock originating at the intersection of the midspan damper leading edge and the blade suction surface and extending across the passage. A second shock was observed in some of the holograms that appeared to emanate from the intersection of the midspan damper and the pressure surface of the blade. This shock appeared to be almost normal to the blade surface. The shocks associated with the midspan damper were not considered in the rotor design. Due to the limited viewing angle, only faint indications of trailing-edge shocks were observed on some of the holograms. The aerodynamic measurements made in conjunction with the holographic tests indicate that this shock system is weak. Apparent tip leakage vortices were detected emanating from the suction surface leading edge and extending approximately to midchannel. The vortices obscured shock definition in the blade tip region.

Double-exposure scattered-light holography techniques were found to provide meaningful qualitative velocity measurements. Because of the 50-nsec pulse limitation of the laser used, the recordings were limited to very low rotor speeds on the order of 8 percent.

The transition of the rotor mode from transonic to supersonic (unstart to started) was clearly evident from the holograms. Acceleration along a constant

throttle line showed a strong detached bow shock at 80 percent design speed, a strong normal shock at 90 percent design speed, and finally, the transition to an oblique shock at approximately 92 percent design speed when fully supersonic. The strong normal shock is consistent with the decay in peak efficiency observed at 90 percent design speed.

The static pressure contours obtained from high-response tip pressure transducers did not explicitly define shock locations; however, the region of the tip leakage vortices, maximum static pressure, and trailing-edge shock are in accord with shock patterns defined by the hologram. The tip leakage vortices, wall boundary layers, and designed shock weakness at the rotor tip section made the isolation of shock fronts difficult.

INTRODUCTION

Flow visualization of gases has provided a valuable tool in the advancement of aerodynamic understanding. Interferometry, Schlieren, and shadowgraph are classical techniques that have been used to study two dimensional flow through cascades and isolated airfoils. Later developments led to three-dimensional visualization studies in which smoke was injected in low-velocity cascade flow to make visible secondary flow in single- and double-flow cascades. With the advent of holography in recent years a new dimension in flow visualization techniques was introduced. Holograms are a product of coherent optics that yield three-dimensional optical images with continuously changing parallax. In addition, one can make interferometric comparisons. Holographic interferometry does not require the optical precision of classical interferometry such as Mach Zehnder.

The use of holography and coherent optical techniques to record the aerodynamic phenomena in and around a rotating blade row was undertaken. The development of holographic equipment that permits recording of high-quality holograms with pulsed ruby lasers of low temporal coherence was a TRW Systems contribution. Holograms made in these optical devices are as bright as holograms made with coherent gas lasers. This device is referred to as a holocamera. The three different types of optical techniques undertaken were: (1) pulsed laser transmission holography (single- and double-exposure), (2) pulsed laser transmission holographic interferometry, and (3) pulsed laser scattered-light holography. Holograms can be recorded in the presence of vibration, turbulent flow, etc. with a Q-switched ruby laser. These lasers are unique in that they emit on the order of a calorie of light in time intervals of 50 nsec. This short time interval enables stopping motion at any instant of time.

The holographic configuration developed for this application is referred to as a path-and-transversing match holocamera (Ref. 1). Although somewhat more complicated, this type of holographic arrangement is essentially insensitive to temporal and spatial coherence of the laser illuminator. A Q-switched ruby laser could be operated well above threshold at high output energies (one Joule). This type of holocamera has been successfully demonstrated in holograms of liquid-fuel combustion in rocket engines and holographic interferograms of ballistics. (Refs. 1, 2, 3, and 4.)

The program reported herein was conducted under NASA Contract NAS 3-15336. The program objectives were to demonstrate that three-dimensional shock waves could be detected and velocity measurements made within a transonic fan rotor blade row using holographic techniques. The development of the holocamera design, the technique utilized to record the holograms, and the results of the holograms are discussed. The analytical procedure for reconstruction and interpretation of the holograms and the development of the models showing the shock system follows. These results are then compared with the blade element performance and rotor tip static pressure contour plots.

TEST FACILITY AND TEST STAGE

General Description

The installation of the holographic apparatus on the fan test stage is shown in fig. 1. The laser power source and control panel were located immediately outside of the test cell and, therefore, do not appear in this figure. As seen, the holocamera assembly is mounted beneath the test stage. The entire holocamera assembly is supported by a steel structure that bridges the test stage and bedplate and is mounted on vibration isolation pads fastened to three piers anchored to the floor. The holocamera assembly is thus independently supported and free from vibration.

The holographic layout originally conceived transmitted the laser beam into the centerbody through a forward strut, directed it axially along the fixed centerbody, reflected it outboard through a window in the centerbody, through the blade tip region, and onto the holographic plate. This approach had several inherent disadvantages. One disadvantage was that the optics would have to be packaged within the fixed centerbody and supported independently of the test stage via the struts. More importantly, however, the field of view was limited primarily to the blade leading edge area, whereas the area of greatest interest is within the blade passage.

This scheme was therefore abandoned in favor of a system whereby the scene beam was directed diagonally across the fan inlet as shown schematically in fig. 2. In the final configuration, the scene beam enters through a large Plexiglas "scene" window in the outer casing forward of the rotor. The scene beam transmits diffused light diagonally across the inlet, beneath the fixed centerbody, through the blade tip region, and through a Plexiglas "viewing" window onto the holographic plate. By reorienting the scene beam from the centerbody to the outer wall, the unobstructed viewing area was greatly improved. The installation and relative location of the two windows are shown in fig. 3.

Transonic Fan Stage Description

The test stage utilized for this program was a high-tip-speed, low-loading, transonic fan stage designed and tested by the AiResearch Manufacturing Company, a Division of The Garrett Corporation, under NASA Contract NAS 3-13498. The fan stage (described in detail in ref. 5) was designed with weak oblique shocks in the rotor tip region to minimize losses. The inlet and outlet relative velocities

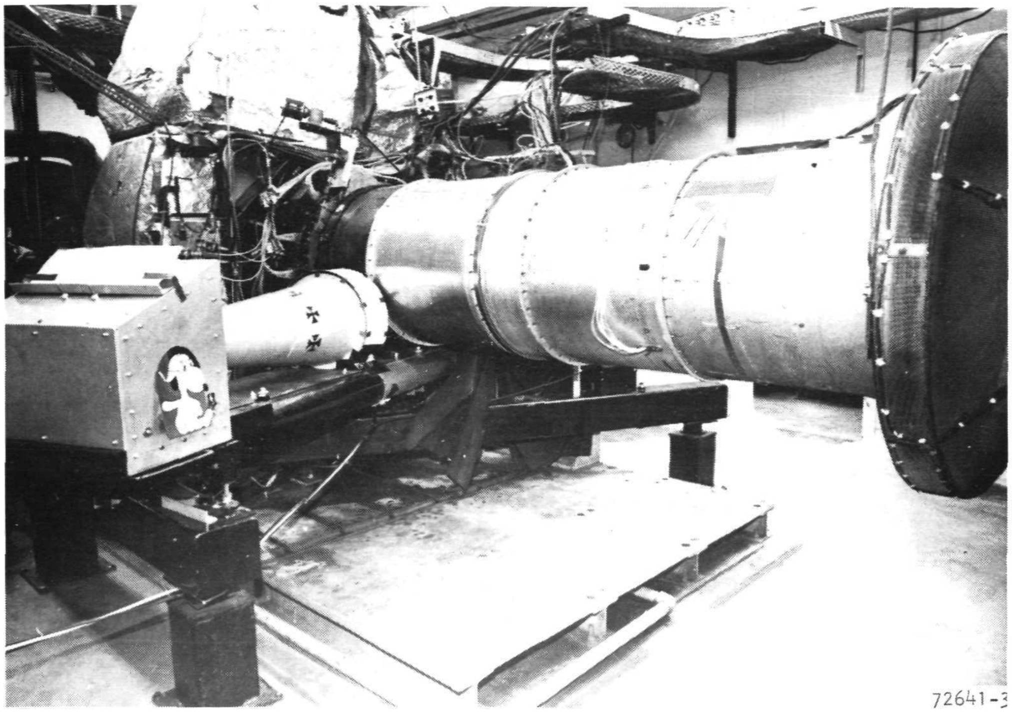

72641-3

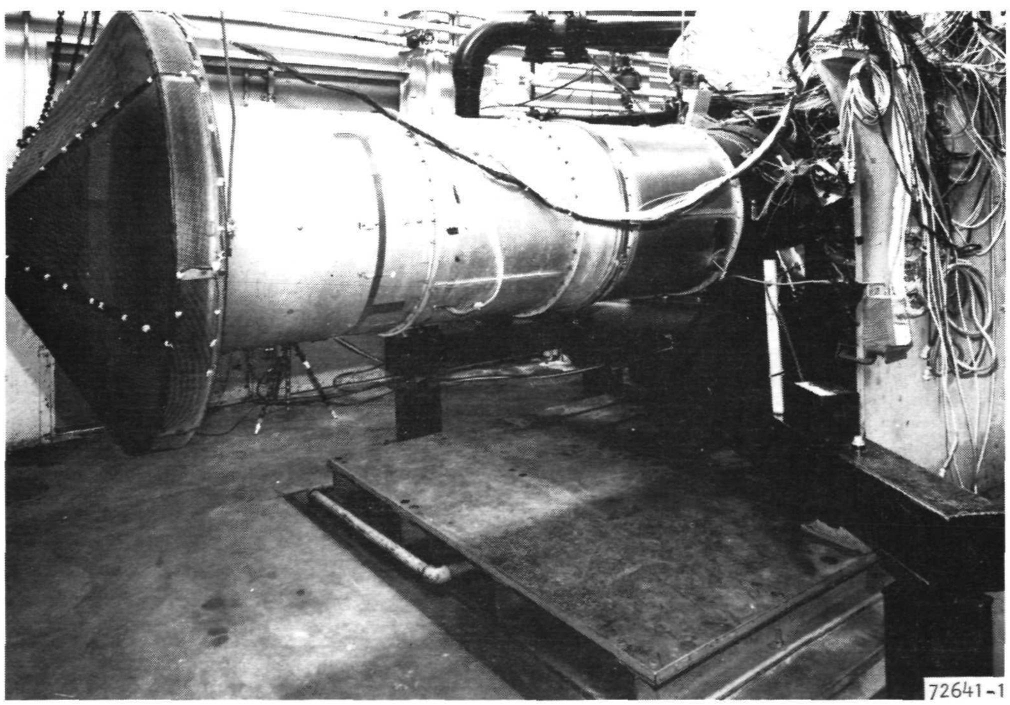

72641-1

F-18475

Figure 1.--Holocamera and Transonic Fan Stage Test Installation.

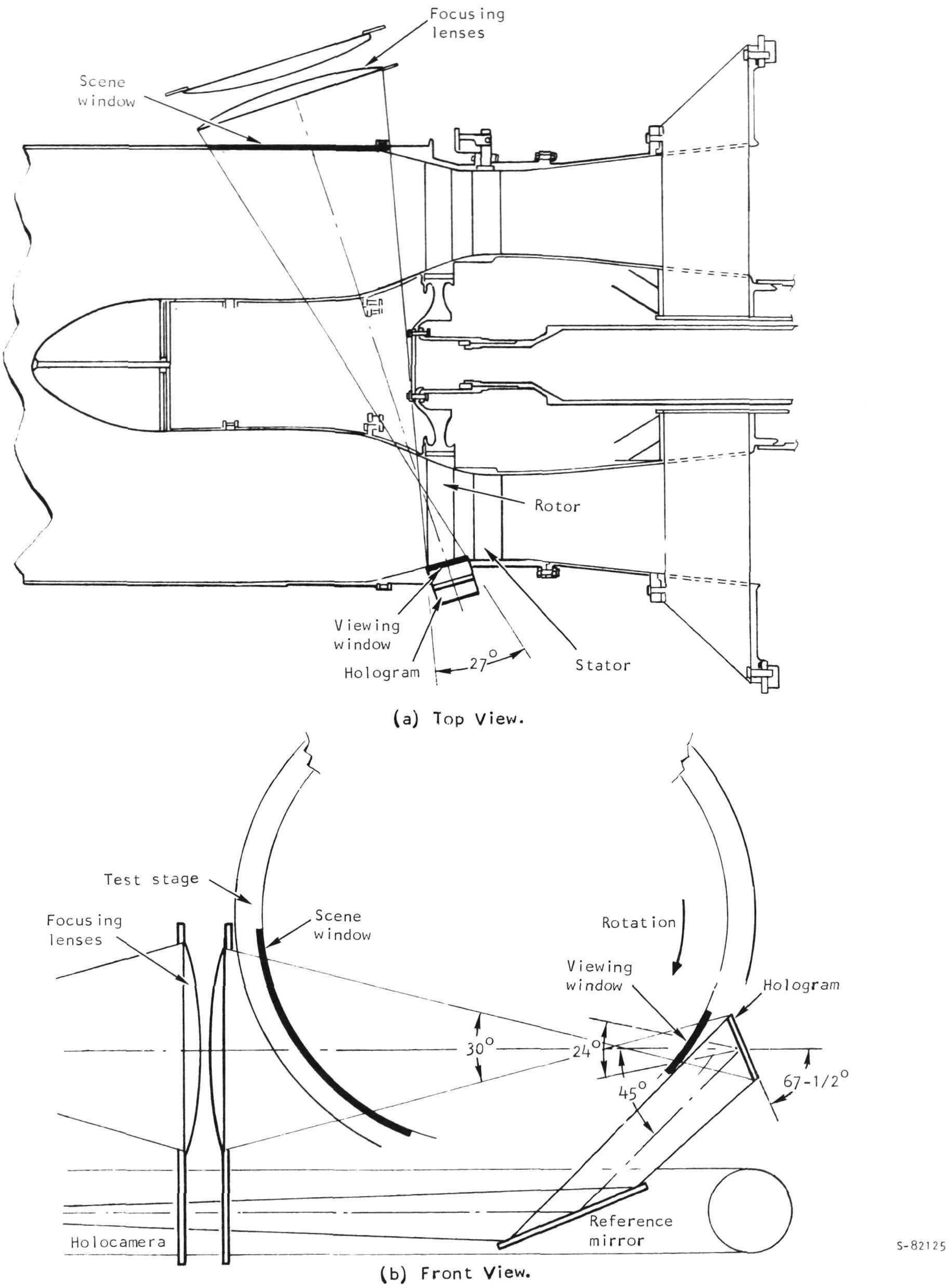

Figure 2.--Holocamera and Transonic Fan Stage Installation Schematic.

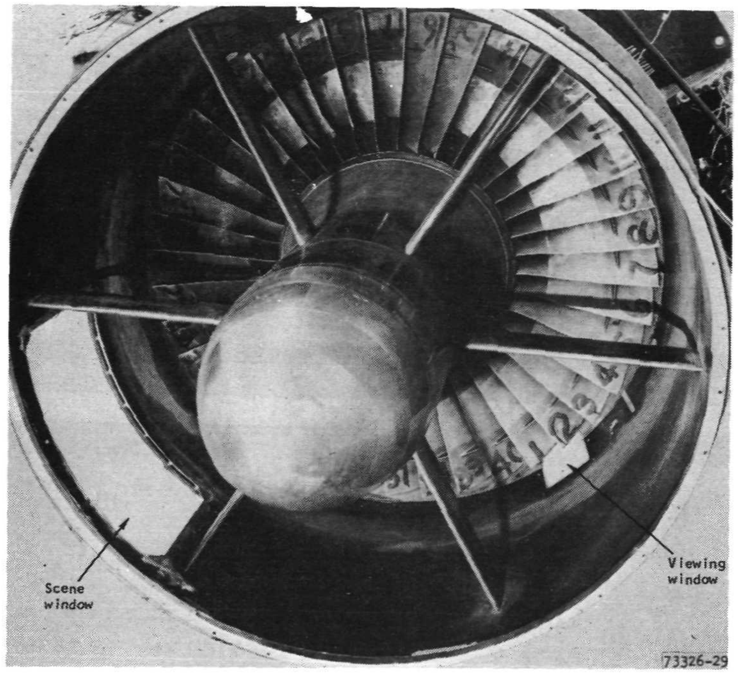

(a) View From Inlet.

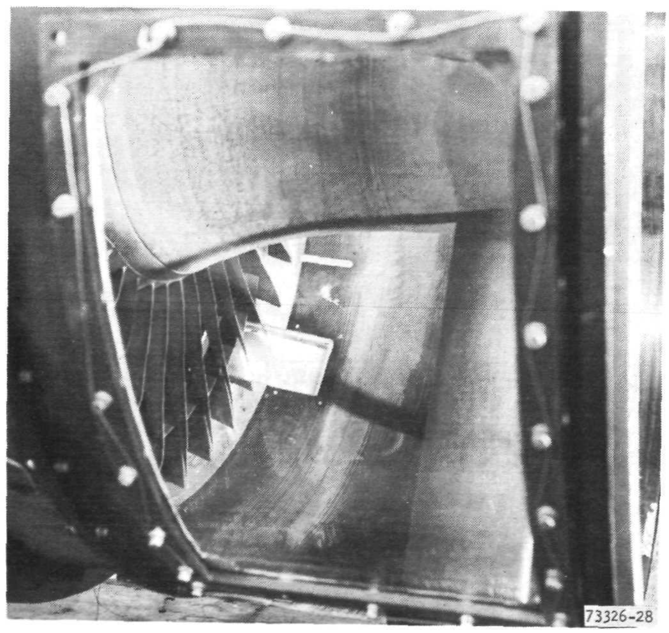

F-18480

(b) View From Scene Window.

Figure 3.--Installation showing Scene and Viewing Windows.

were supersonic in the outboard section, transonic in the central section, and conventionally subsonic in the inboard section. Design parameters are as follows:

Overall pressure ratio	1.5
Adiabatic efficiency	0.86
Equivalent total flow	148 lb/sec (67.1 kgm/sec)
Flow per unit annulus area	42.0 lb/sec-ft^2 (205.1 kgm/sec-m^2)
Equivalent tip speed	1600 ft/sec (488.6 m/sec)
Inlet hub-to-tip radius ratio	0.46
Tip diameter	28.74 in. (0.73 m)
Number of rotor blades	40

The test stage is a single-stage axial-flow design with no inlet guide vanes. The rotor blades consist of 40 arbitrary airfoil sections with an aspect ratio of 2.64 and midspan dampers located at 30 percent span from the rotor tip. The rotor inlet hub-to-tip ratio is 0.46. Nominal running tip clearance was 0.045 in. (1.14 mm) at design speed and 0.035 in. (0.89 mm) at 110 percent design speed.

The stator consists of 45 vanes with an aspect ratio of 3.10. Airfoil sections are double circular arc. The stator vane leading edge is located 1.420 in. (3.61 cm) downstream of the rotor hub trailing edge. During the aerodynamic performance test, it was determined that the best stage operating characteristics were obtained at a 3-deg-closed stator setting. This setting was maintained throughout the holographic testing. The details of the rotor design technique and the flowpath and stator design are given in ref. 5. The final rotor design is discussed in ref. 6 along with a description of the facility and instrumentation.

Test Stage Modifications Required for Holography

A 3 x 5 in. (7.6 x 12.7 cm), 0.75 in. (1.91 cm) thick Plexiglas viewing window was provided in the rotor outer case. The window was sized to sufficiently view one complete rotor blade passage from blade leading to trailing edge. Because of the midspan dampers, however, only approximately 3/4 of the blade passage was clearly visible. A large Plexiglas scene window formed as a 53-deg cylinder approximately 15.5 in. (39.4 cm) in radius, 9.75 in. (24.8 cm) wide, and 0.5 in. (1.27 cm) thick was installed in the outer casing forward of the rotor. The scene window provided a port through which the scene beam was transmitted into the flow annulus.

Electromagnetic pickups were installed on the fan main drive shaft and outer shroud adjacent to the rotating blade tips. The pickups generated the signals for activating the oscilloscope in the laser synchronization circuit to arm and fire the laser.

The stator vane actuating lever and unison ring were removed in the area of the viewing window, and the stators were locked in position. This allowed the holographic plates to be positioned close to the viewing window and as far aft of the blade passage as possible.

An actuator drive was installed on the test stage to reposition the holocamera platform by approximately 0.040 in. (1.02 mm) during the long double-exposure holography tests. To minimize vibration effects, the actuator was driven against rubber isolation pads mounted on the support structure. Position sensors were attached to the test stage to monitor relative positions of the holocamera and stage.

HOLOCAMERA DESIGN

The holocamera developed under this program is unique in that it is actually two separate holographic arrangements mounted in a single rigid tubular framework. One arrangement is used to record single- and double-exposure bright-field holograms, the other to record dark-field scattered-light holograms. Both arrangements share the same focusing lenses and reference beam optics. Transition from one recording arrangement to the other is accomplished rapidly and easily by exchanging a few key optical elements (beam splitters, prism plates, and reflecting prisms). These were mounted on a single sliding plate driven by a pneumatic actuator.

Optics Configurations

The two holographic configurations are shown schematically in figs. 4 and 5. Fig. 4 shows the arrangement of optics for recording the bright-field holograms and fig. 5 shows the dark-field arrangement. The large 14-in.-diameter (36-cm-diameter) intermediate focusing lenses have sufficient focal length to span the lower portion of the fan test stage and give a viewing angle of about 27 degrees to the holograms.

The holocamera is constructed on a tubular steel framework welded watertight, making it possible to fill the frame with either water or dry sand to increase the mass of the holocamera and thereby reduce the amplitude of vibration induced by the fan stage. The optical components are rigidly mounted to the frame.

An aluminum enclosure is provided on one end of the holocamera to support the sliding plate and one front surface mirror (for the bright-field configuration). It also anchored the shield between the diffuser and the focusing lens set. The reference beam prisms and the lens for spreading the reference beams are mounted below the enclosure on a steel plate welded to the tubular framework. Panels across the exposed top and bottom portions of the tubular frame minimize air turbulence through the reference beam path.

The illuminating laser beam is deflected into the holocamera by a right-angle reflecting prism beneath the framework. Depending on the position of the sliding plate, the beam illuminates either the bright-field holographic arrangement or the dark-field scattered-light holographic arrangement.

<u>Bright-field configuration</u>.--In the bright-field configuration (fig. 4), the reflected beam first encounters the flat surface of a plano-concave diverging lens (combined beam splitter and diverging lens). The portion of the beam that is reflected from the flat surface becomes the reference beam, while the portion passing through the lens becomes the scene beam.

The reference beam is diverted downward into a wedge prism and a reference reflector prism. The wedge refracts the light at an angle such that it is totally reflected by the reflector prism. This element directs light through

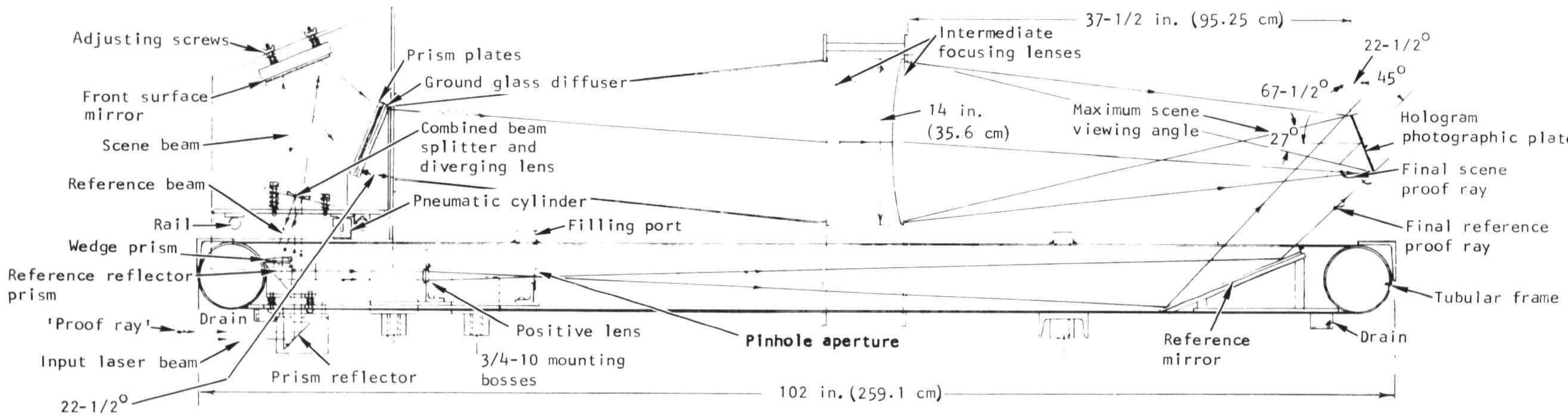

Figure 4.--Schematic of Holocamera Arrangement for Recording Bright-Field Holograms and Holographic Interferograms.

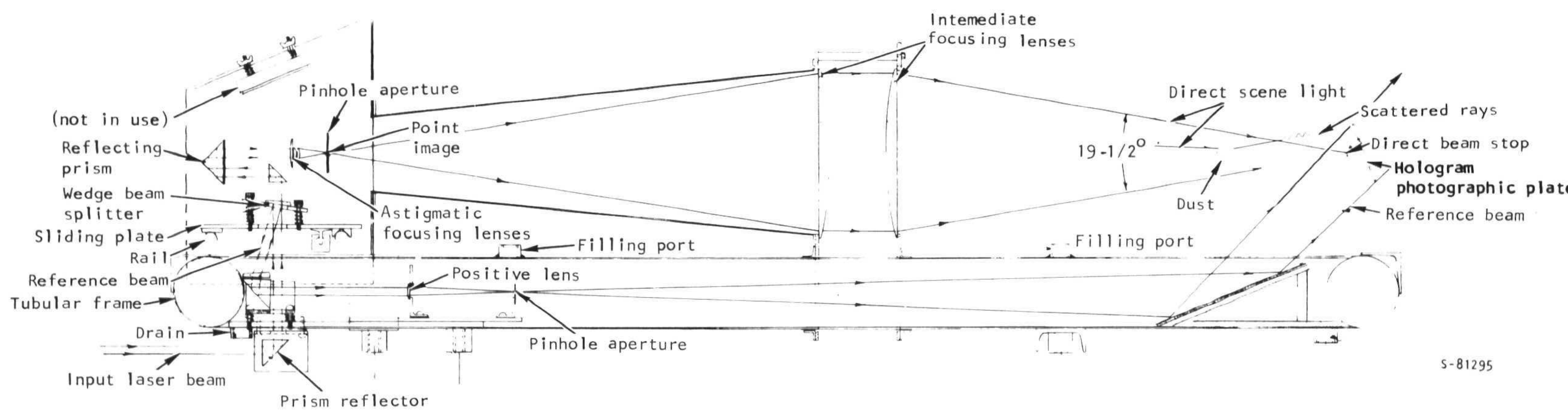

Figure 5.--Schematic of Holocamera Arrangement for Recording Dark-Field, Scattered-Light Holograms.

a positive converging lens and a pinhole aperture onto the reference mirror. The mirror directs light to the hologram photographic plate at an angle of 45 degrees. The pinhole aperture at the focal point of the positive lens eliminates stray light from the optics behind the focal point.

The scene beam in the bright-field arrangement is incident on a 6-in.-diameter (15-cm-diameter) front surface mirror mounted to the top of the enclosure. This mirror reflects the scene beam onto a prism plate, which directs the beam toward the focusing lens set. A glass plate, rough-ground on both surfaces, diffuses the light. Light scattered by this ground-glass diffuser is refocused by the intermediate focusing lenses onto the hologram photographic plate. The photographic plate and ground-glass diffuser are actually at 1:1 conjugate image points. The lenses serve to spatially match the scene beam to the reference beam at the hologram photographic plate. In other words, a ray or cross sectional element of the original input laser beam recombines with itself at the photographic plate, thus creating the bright-field hologram. This holocamera arrangement is basically a "path-matched focused ground-glass holocamera," similar to those first built to record holograms of liquid rocket fuel combustion (refs. 1 and 2).

Dark-field, scattered-light configuration.--In the dark-field, scattered-light holocamera configuration (fig. 5), the illuminating laser beam from the prism reflector mounted below the tubular framework, encounters a glass wedge beam splitter, which divides it into scene and reference beam components. The reference beam path is the same as that of the bright-field holocamera configuration. The scene beam, the principal amount of light transmitted through the wedge (92 percent), enters a second right-angle prism reflector, which directs it into a third, larger reflecting prism. This prism reflects the beam toward the astigmatic focusing lenses. The prism mount is adjustable for path matching. The astigmatic focusing lenses focus the second beam through a pinhole aperture, which blocks all light scattered by and from the surfaces of the optics preceding it, creating a point source of light in front of intermediate focusing lenses.

The intermediate focusing lenses refocus the light to a point in front of the photographic plate where a beam stop blocks the focused light from reaching the hologram. Particles are introduced at a point between the intermediate focusing lenses and the beam stop to scatter light past the beam stop toward the photographic plate. The holocamera is actually arranged for the most efficient scattering of light. The scattered light rays that reach the photographic plate recombine with the reference beam to create the scattered light hologram.

Q-Switched Ruby Laser Illuminator

A schematic of the Q-switched ruby laser used to illuminate the holocamera is shown in fig. 6. The system consists of an oscillator and an amplifier; the oscillator incorporates two nitrobenzene Kerr cells, which can generate two separate Q-switched pulses with separations of a few μsec.

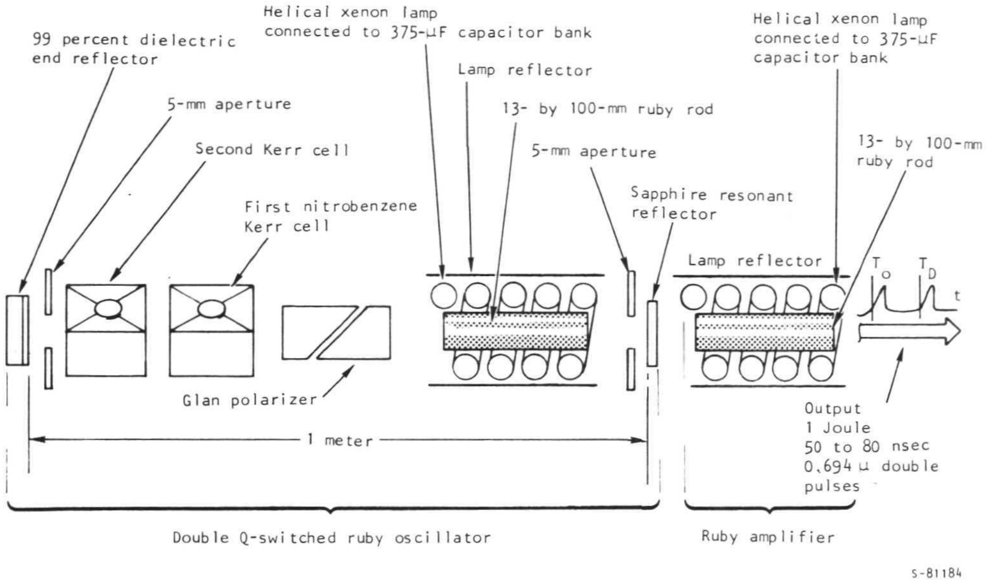

Figure 6.--Schematic of Ruby Laser Illuminator used to Record Holograms.

The double-pulse capability developed for this program differs from the more conventional practice of using a single Pockel cell with sophisticated electronics to double-pulse the single electro-optical element. The unique feature of the double-pulse circuit arrangement shown in fig. 6 is that the two electronically isolated circuits can be pulsed independently with essentially no limitation on minimum separation time. The arrangement can be used to generate two pulses with approximately 2 μsec separation to record the rapid double-exposure holograms.

Using only one Kerr cell, the laser shown in fig. 6 functions as a convectional Q-switched ruby laser, generating a single 50- to 80-nsec giant pulse (refs. 1 and 7).

The ruby rod, the surrounding helical xenon flash lamp, and the external silver lamp reflector are mounted in a single sealed housing. Coolant at a temperature of about 59°F (15°C) (just above the dew point) flows through the housing, cooling both the lamp and the ruby rod.

The flash lamp is fired by discharging a 375-microfarad (μF) capacitor through the lamp terminals. The bank is usually charged to 4300 V, representing an energy of 3500 Joules (J). Green and blue portions of the light emitted by the flash lamp are absorbed by the chromium ions inside the ruby rod. This excitation is held by the ruby rod for times on the order of several msec. The excitation represents the storage of energy in the rod. The excitation also gives the rod gain for light at the wavelength of the flourescent transition, (i.e., the R_1 transition, which has a wavelength of 0.6843 microns at 68°F (20°C) (ref. 1)

The combination of a pumped ruby rod (or optical amplifying region) with a pair of mirrors (i.e., the 99 percent dielectric mirror and the sapphire resonant reflector) is the optical analog of an electronic feedback amplifier. Such a combination oscillates as long as the gain exceeds the losses.

Either Kerr cell in fig. 6 can be used in concert with the polarizing prism (a calcite Glan polarizer) to stop oscillation. Biasing either Kerr cell to its quarter-wave bias prevents return of all light that leaks out of the end of the ruby rod. Feedback is stopped, and the combination can no longer oscillate. As a result, a larger fraction of the chromium ions in the rod can be excited. The greater the excitation of the atoms, the greater the storage of energy, and the greater the gain.

If the quarter-wave bias is instantaneously removed from the Kerr cell, the energy stored in the excited atoms is converted into light of the wavelength of the laser transition. The conversion takes place in approximately 20 complete cycles from one end mirror to the other and back again. The pulse duration is typically 0.05 to 0.08 μsec for a laser with mirrors separated by 1 m. A 1-cm-diameter, 10-cm-long rod can emit 1 J of light. The peak power of such an emission is on the order of 20 milliwatts (mW).

If the Kerr cell is not opened, the excitation will decay away in 3 msec.

The ruby rod is thus an energy storage device that converts, on command, the optically stored energy into light. The stored energy can be converted into either a single light pulse or a number of individual light pulses.

The second Kerr cell in the laser cavity generates the second pulse. To double-pulse a ruby laser, one half of the energy stored in the laser rod is converted into light. This is done by partially opening one of the Kerr cells. The other Kerr cell is then opened and the remaining energy is converted into light. The proper operating voltages are determined by experimentation.

The second ruby rod functions purely as an amplifier. The rod is identical in size to the rod in the oscillator. Its flash lamp is connected to an identical 375-μF capacitor bank. The bank is charged typically to 4500 V representing an energy of 3800 J.

Initially, the oscillator lamp is fired. For single-pulse operation, the quarter-wave-biased Kerr cell is short-circuited by a hydrogen thyratron, approximately 800 μsec after the start of current through the first flash lamp. The 800-μsec time was found to be near optimum; however, a giant pulse can be generated ranging from 0.5 to 1.2 msec. The 800-μsec delay produced the highest amplitude, shortest duration laser pulse.

The amplifier normally was initiated 0.15 msec after the start of current through the first flash lamp. This small delay optimized the gain relative to the emission of the pulse from the oscillator.

The double-pulse operation of this double Kerr cell laser is shown schematically in fig. 7.

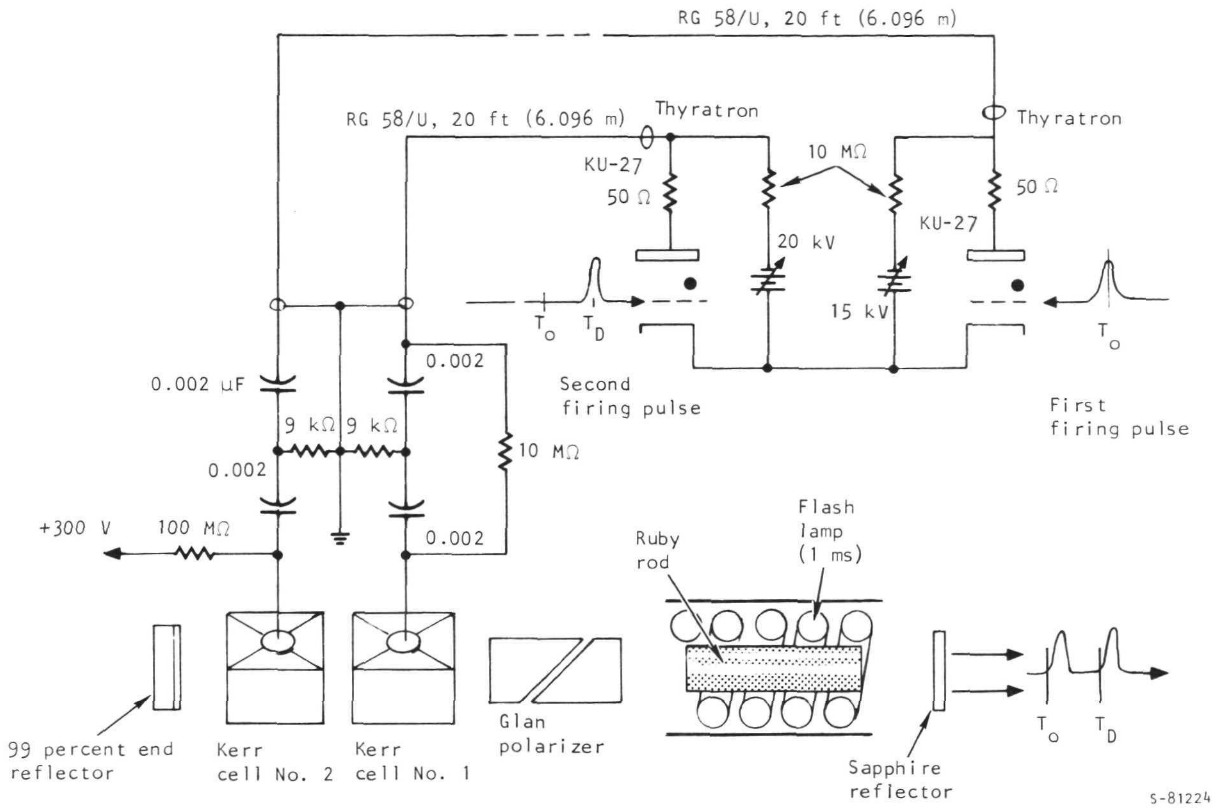

Figure 7.--Schematic of Double-Pulsed, Q-switched Ruby Laser.

Two large hydrogen thyratron apply and remove high voltage from the two Kerr cells. The first Kerr cell is connected to the plate of the first thyratron through a 10-megohm (MΩ) resistor and approximately 20 ft (6.1 m) RG/58 U (52-Ω characteristic impedance) coaxial cable. A second 10-MΩ resistor connects the plate of the thyratron with a variable high-power supply (0 to 30 kV). The high-voltage supply is adjusted until the Kerr cell is biased to its quarter-wave bias. The plate of the thyratron also is connected to ground through a 0.002-μF blocking capacitor and a 9000-Ω resistor (at Kerr cell end of cable). A second 0.002-μF capacitor is connected between the 9000-Ω resistor and the Kerr cell. A 50-Ω resistor terminates the cable at the Kerr cell.

Firing the first thyratron (by application of a 300-V pulse to its grid) discharges the first 0.002-μF capacitor through the 9000-Ω resistor. The flow of current produces negative voltage which dies away with the 18-μsec resistor-capacitor (RC) time constant. The second 0.002-μF capacitor couples this voltage step to the plates of the Kerr cell. The Kerr cell voltage thus instantaneously changes from quarter voltage (typically 20 000 V) to zero volts when the thyratron is fired. It returns to the 20 000-V quarter wave condition with a time constant of 18 μsec. A time span short enough so that the cell is closed before the gain of the rod (due to continued pumping by the lamp) starts the system oscillating again (after lasing.)

The second Kerr cell is identical to the first, with the exception that no resistor is connected from the plate of the Kerr cell to the plate of the thyratron. Firing the second Kerr cell discharges a second 9000-Ω, 0.002-μF RC circuit. The negative RC pulse is coupled to the plates of this Kerr cell. The pulse amplitude, determined by the voltage applied to the plate thyratron, is less than quarter-wave voltage and it can be applied to the plates of the other Kerr cell.

During double-pulse operation, the second Kerr cell is fired before the first. The thyratron voltage is adjusted until the two pulses are of equal amplitude. Results of an early test are shown in fig. 8 (these are oscillograms of the output of a vacuum biplaner photodiode). In this test, the two pulses were separated in time by approximately 80 μsec. The first Kerr cell was biased to within 23.5 kV of its normal quarter-wave bias. The right column shows the laser output power. Each oscillogram shows traces corresponding to the two pulses. The left column shows the integral of power or emitted energy. The two steps in the oscillogram verify that the laser emitted two pulses.

The fine structure seen in the oscillograms of laser output power shows that the laser was emitting a multiple of cavity modes. This type of emission is referred to as multimode emission, which results in a laser with low coherence.

As the program progressed, it became important to have a laser in which the two pulses were separated by as little as 2 to 5 μsec. This was accomplished by using the circuit shown in fig. 7. It was possible even though the first Kerr cell was still recovering at the time that the second Kerr cell was fired. Voltages had to be adjusted to compensate for the interaction.

Laser Pulse Synchronization

Synchronization of the laser to the blade position is complicated by the need to start pumping the ruby rod before the Q-switch pulse occurs. Approximately 3/4 msec is needed to charge the ruby with an electronic flash lamp. Q-switching can be accomplished from 1/2 msec to 1 msec after the start of pumping. As discussed previously, this is achieved by short-circuiting the quarter-wave voltage (23 kV) on the Kerr cell with a hydrogen thyratron. The laser pulse is prompt, occurring within 0.1 μsec of removal of the voltage from the Kerr cell.

During the early part of the program, the fan test stage was provided with two capacitance-type sensors, one located opposite the drive shaft, and the second opposite the rotating blades. Fluctuation in the capacitance of the circuit due to the proximity of a boss on the drive shaft or the individual blade edges generated charging and discharging voltages, which were amplified.

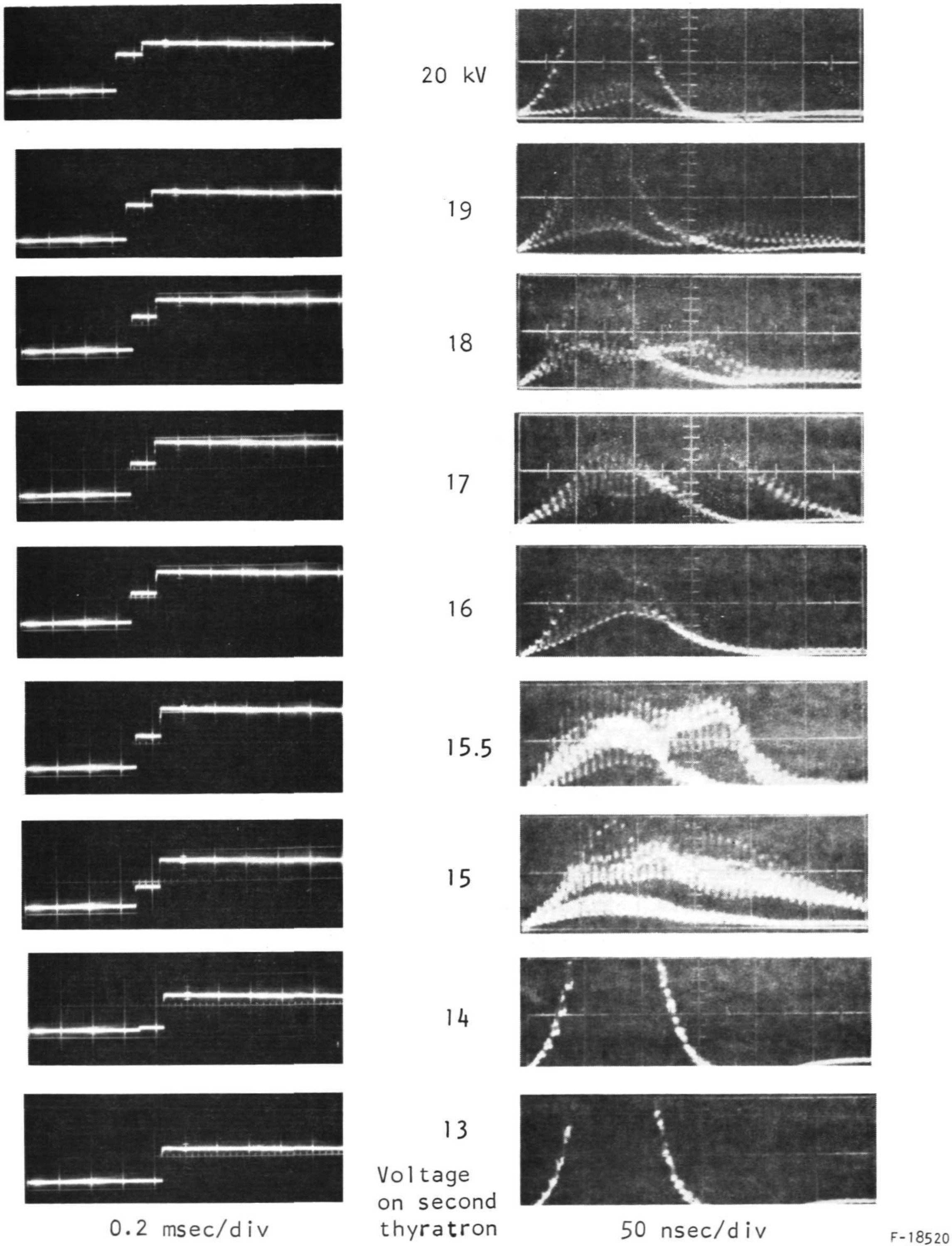

Figure 8.--Integrated and Instantaneous Emission From Ruby Laser.

One capacitive probe generated a pulse for each rotation of the shaft; the second probe generated a pulse for each blade passage. These signals are referred to as the "one-per-rev" and "40-per-rev" signals, respectively. Sample oscillograms are shown in fig. 9. Inspection shows that the one-per-rev signal is a 30-μsec pulse of 8-V amplitude. At a speed of 14 000 rpm (1466 rad/sec), the pulse separations are 4.3 msec and 108 μsec, respectively.

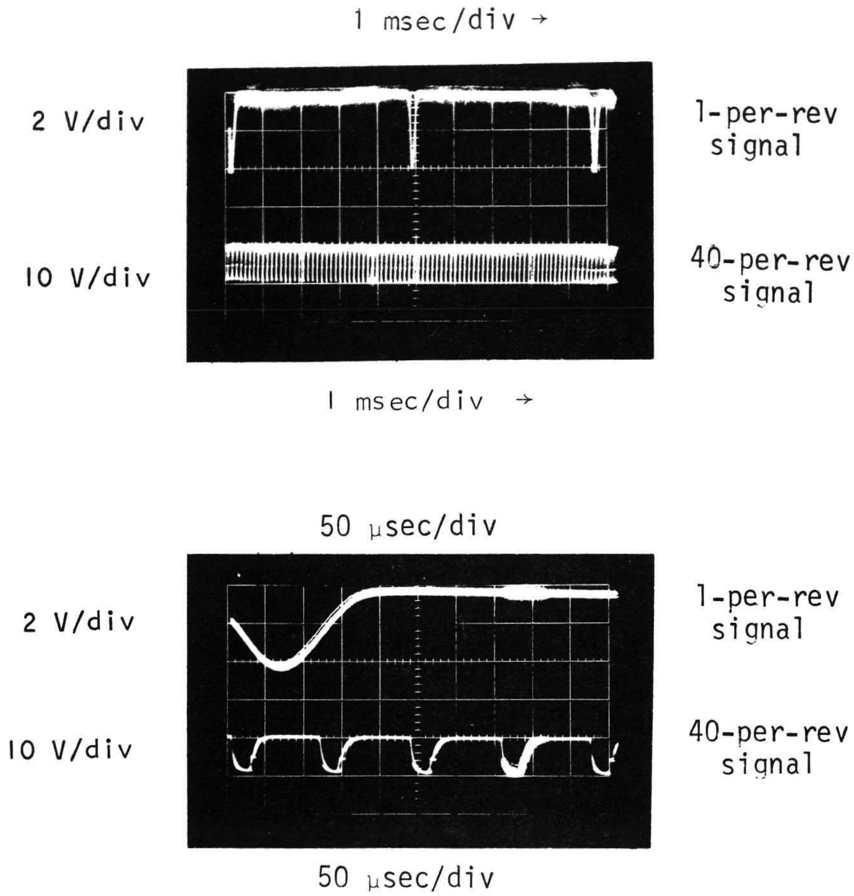

F-17748

Figure 9.--Sample Oscillograms Showing Signals used to Time Firing of Ruby Laser (100 percent Design Speed).

A pair of commercial dual-beam oscilloscopes (Textronix Types 555 and 565) and a commercial Kerr cell delay generator were used to delay pumping and firing of the laser relative to the one-per-rev signal. The oscilloscopes selected are particularly adaptable to this type of function. A schematic showing the interconnections of the oscilloscopes is shown in fig. 10. The one-per-rev signal is connected to the first vertical amplifier of the first oscilloscope. The first time base is set to trigger from this signal. When firing the laser, it is further set to the single sweep mode. The "+ gate" from this time base is connected to the input of the delay generator. This circuit produces a delayed pulse relative to the + gate or one-per-rev signal. Maximum delay is one msec in 50-µsec steps.

The second time base on the oscilloscope, Time Base B, is set to trigger after a predetermined delay set by the delay generator circuit of the oscilloscope. The function on the scope is entitled, "Trigger once for each "a" delay". This delay is called T_2. After a wait or delay of T_2, the time base will trigger on the next signal fed to the lower beam amplifier. The 40-per-rev signals are connected to this amplifier. In this way, any blade can be selected to initiate the + gate.

The + gate from the second time base is used to trigger the first time base of the second oscilloscope (the 565). The 40-per-rev signal is displayed on the vertical amplifier. The scope thus shows the blade passage signal which triggers it, as well as the next blade signal.

The 565 oscilloscope is similar to the 555 in that it has a second time base that can be delayed relative to the first, determined by a precision potentiometer. This oscilloscope is set to start the second time base after the delay set on the potentiometer (unlike the 555, which was set to trigger after the specified delay). The delay is called T_3.

The + gate from the second time base triggers the hydrogen thyratron in the laser. The second oscilloscope thus enables precision firing of the laser relative to the selected 40-per-rev pulse, and properly orients the position of the blade in the viewing window.

In addition, both scopes display a signal proportional to the energy emitted by the laser. This signal is generated by a photo diode inside the laser. A step voltage indicates proper laser emission, namely, a single pulse of 50 nsec duration. The output of the delay generator also is displayed on the upper sweep of the first oscilloscope.

Figure 11 schematically shows the relative positions of the one-per-rev, 40-per-rev, delay generator pulse, and oscilloscope + gate signals.

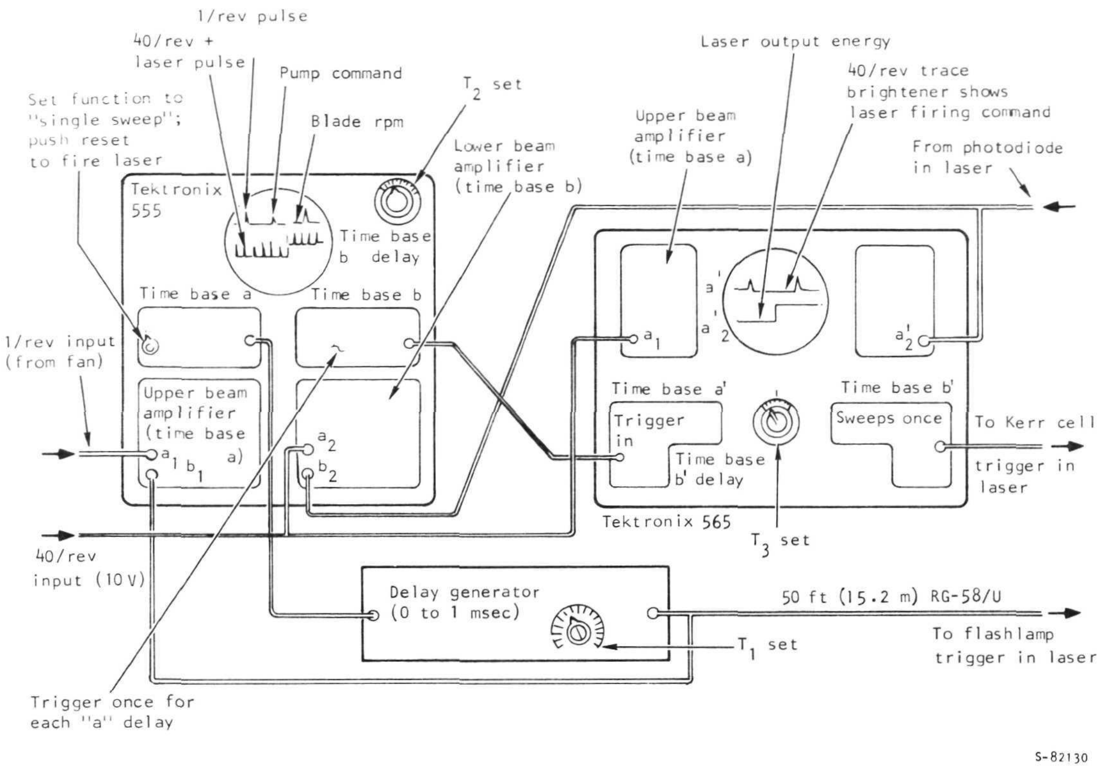

Figure 10.--Double Oscilloscope Scheme for Precisely Firing Ruby Laser Between Blade Rows of Fan.

As the program progressed, the capacitance sensors originally installed on the fan test stage were found to be intermittent, causing the laser to misfire. The probes were replaced with conventional electromagnetic pickups, which generated voltages proportional to the rate of change of magnetic field through a coil. These signals could not drive the speed-measuring electronics because of the complex voltage wave generated. The signals were, however, adequate for activating the oscilloscopes as shown in fig. 9. Photographs of the signals generated by these sensors are shown in fig. 12. The upper trace depicts the one-per-rev signal. The leading pulse shown in the upper trace was generated from a magnetic pickup on the hub. The following pulses on the same trace were generated from the passage of balancing holes drilled in the hub. The lower trace depicts the 40-per-rev signals. The two signals were interconnected into the circuit in the same manner as the signals from the original probes. The sensitivity and triggering functions of the scopes were changed to accommodate the new signals.

The original timing circuit was modified to include an additional delay unit to fire the second Kerr cell in the laser. A second Tektronix 555 oscilloscope was coupled to the original 555 and 565 oscilloscopes as shown in fig. 13. The one-per-rev and 40-per-rev signals are inputs for the left and right vertical amplifiers of the first 555 oscilloscope. Both are swept by time base a, triggered from the one-per-rev signal. The 40-per-rev

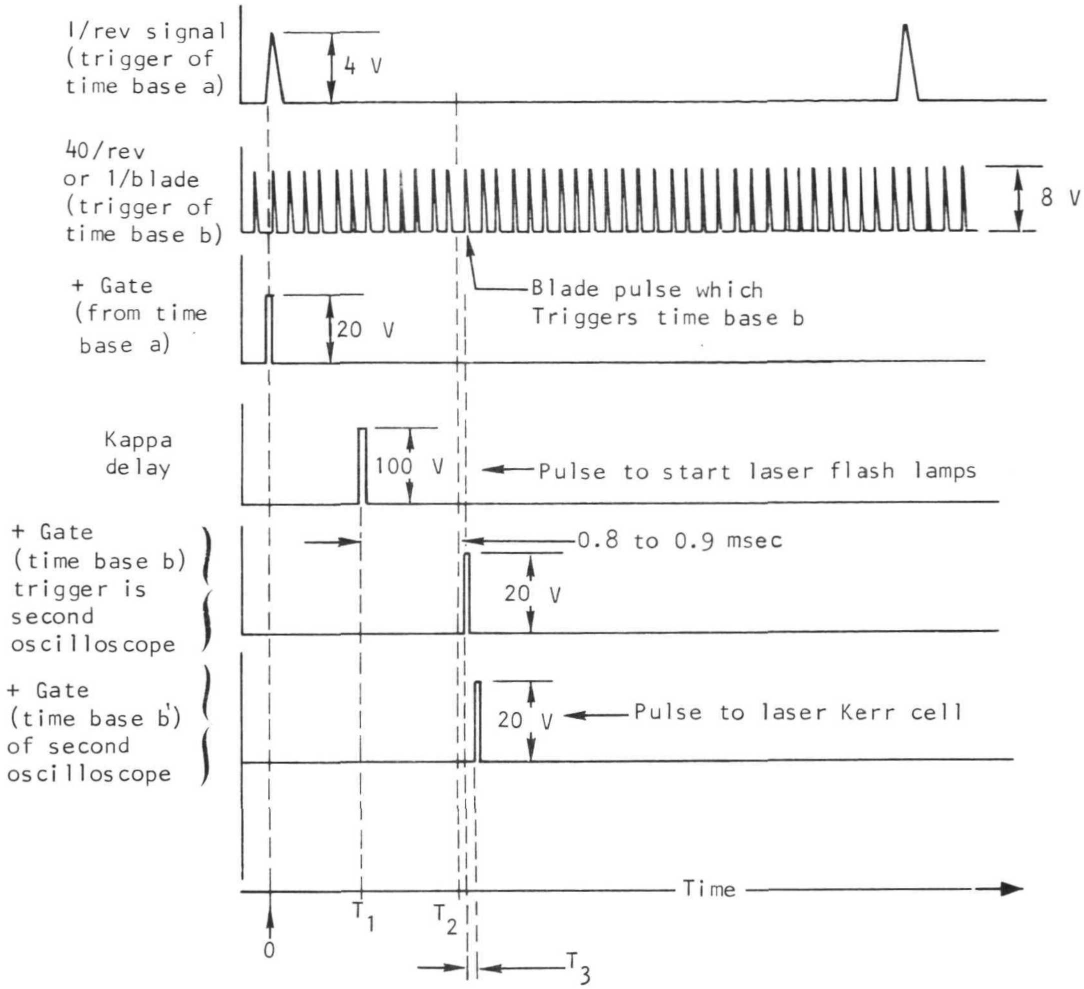

Figure 11.--Schematic of Relationship of Electrical Signals used to Synchronize Firing of Ruby Laser between Blade Rows.

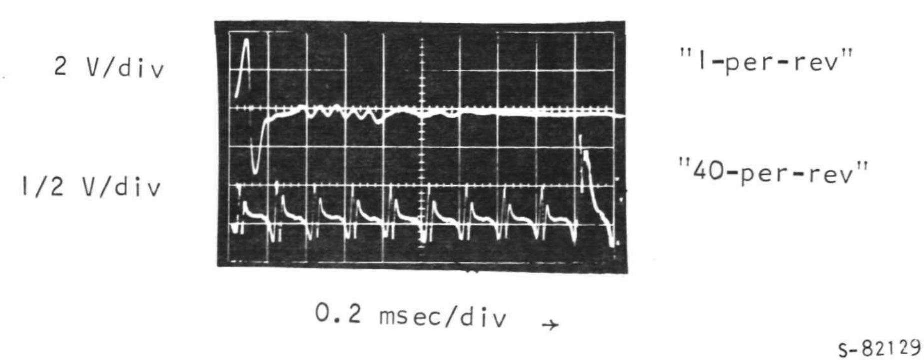

Figure 12.--Signals from Magnetic Pickup.

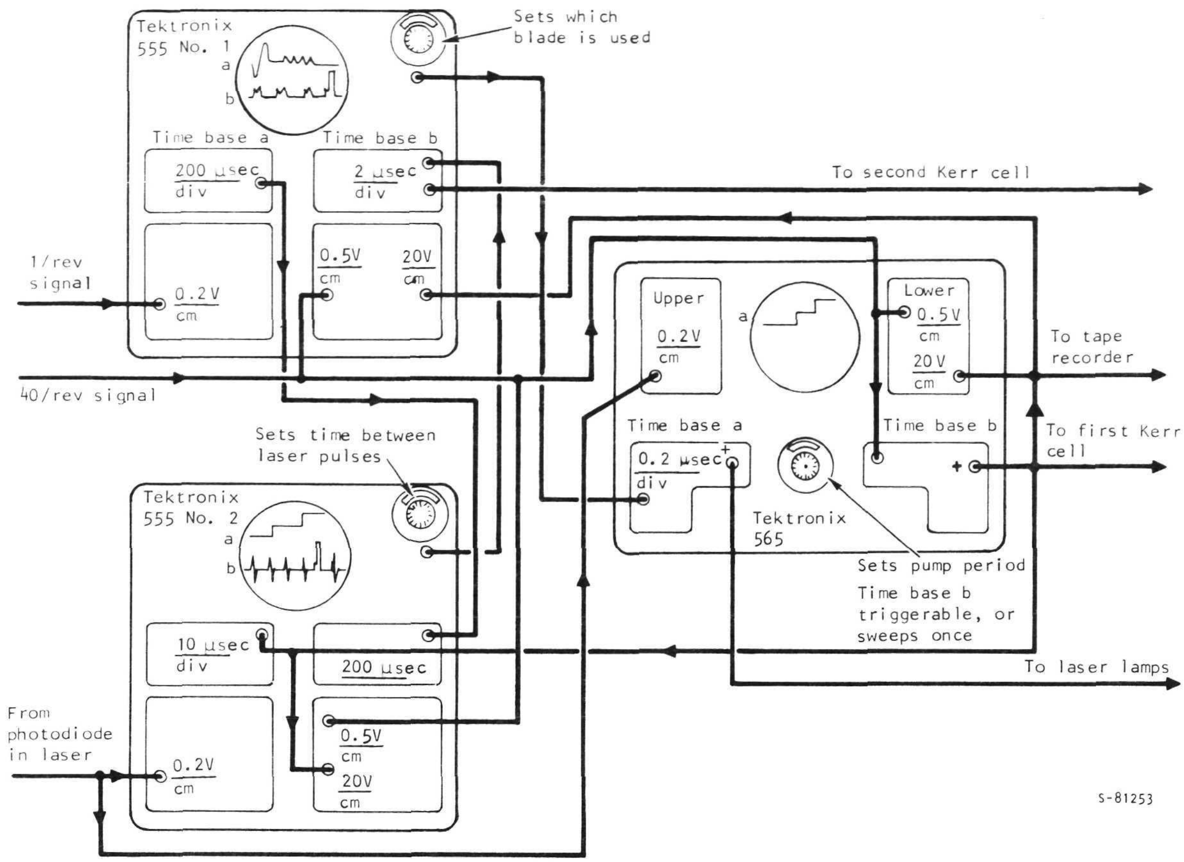

Figure 13.--Final Triple Oscilloscope Scheme Used to Precisely Double-Pulse Ruby Laser Between Blade Rows.

signal also is connected to the lower beam of the 565 oscilloscope and to the input trigger of the second time base of this oscilloscope (time base b). The "delay-trigger-output" of the first 555 provides a variable delay pulse relative to the starting of the first oscilloscope. This function eventually selects which blade the laser illuminates. The delayed trigger output is connected to the 565, triggering the first time base a of this oscilloscope. The + gate of this oscilloscope is connected via a coaxial cable to the laser supply to fire the flash lamps. This delay trigger output sets the pump period and the exact blade the laser illuminates. The 565 logic is set such that the second time base starts after a predetermined setting of the delayed dial function, called "sweeps once," or is triggerable after the same specific delay period. This latter arrangement lets the 40-per-rev signal trigger the second time base. The triggerable mode is used when accurate blade position is required. The + gates from the second time base are used to fire the first Kerr cell in the laser power supply, as well as to provide a timing identification mark on the data recording equipment and to trigger the third oscilloscope (the second 555). In addition, this signal is displayed on the lower beam of the 565, the lower beam of the 555 (via a dual trace amplifier), and the lower beam of the second 555. As a result, the two scope traces show the intended firing of the laser relative to the 40-per-rev signals. The "delayed-trigger output" of the second Kerr cell provides the signal to trigger the second Kerr cell in the laser power supply. The unused time base in the first 555 oscilloscope is employed as a power amplifier to send the pulse over a long piece of coaxial cable to reliably fire the thyratron in the laser power supply.

The photodiode inside the laser is connected to the vertical amplifier of the second 555. This shows the pulsing of the laser.

A more simplified representation of this firing arrangement is shown in fig. 14. The tabulation in this figure shows the different scope displays. A sample is shown in fig. 14. The thyratron in the laser power supply feeds a noise signal into the coaxial cable so its firing also is seen on the sweep. The thyratron spike can be seen on the lower trace, added to the pulse gate command.

Other System Components

Windows.--Standard Plexiglas was selected as the window material because of its optical homogeneity, transparency to laser light, suitable tensile strength, amenability to fabrication into complex shapes and compound curvatures, and moderate cost.

The windows were shaped by thermally forming standard Plexiglas sheet. Thermal forming minimizes the refractive distortion of transmitted light because the inner and outer surfaces are basically parallel after formation. The larger window, referred to as the scene window, was formed as a 53-deg cylinder approximately 15.5 in. (39.4 cm) in radius, 9.75 in. (24.8 cm) wide, and 0.5 in. (1.27 cm) thick. The smaller window, or viewing window, is 3 in. (7.6 cm) high, 5 in. (12.7 cm) wide, and 0.75 in. (1.96 cm) thick. It fits into the fan outer shroud adjacent to the rotating blade tips. Fabrication of the viewing window was complicated by the fact that its inner surface forms a part of the aerodynamic flow path and thus requires a compound curvature. A photograph of a finished window and the mold used to form it is shown in fig. 15. An unmachined flange is also shown on the concave mold surface.

As the program progressed, the reconstructed holograms indicated that the windows were not sufficiently smooth, particularly the smaller viewing window, which has the compound curve surface. Double-exposure holograms taken with the rotor at rest and the holocamera repositioned between the two exposures showed "fringe islands" of several fringes approximately 1 cm wide across the area of the window. In an effort to minimize the window distortion effects, both surfaces of the window were polished. A moderate improvement in window quality was achieved.

In an attempt to better understand the source of these fringes, thinner windows, 0.25 in. (6.35 mm) thick, were fabricated and tested. It was found that the larger scene window distorted under pressure; the smaller viewing window, however, showed a substantial reduction in fringes.

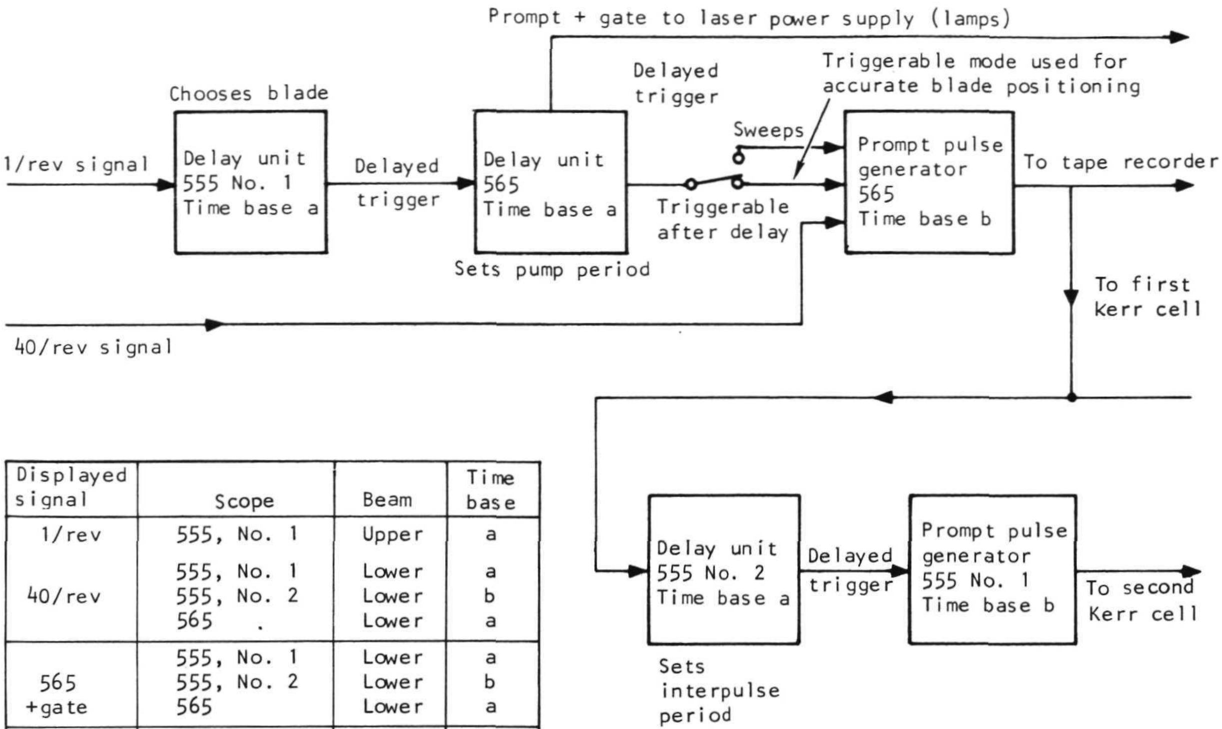

Displayed signal	Scope	Beam	Time base
1/rev	555, No. 1	Upper	a
40/rev	555, No. 1 555, No. 2 565	Lower Lower Lower	a b a
565 +gate	555, No. 1 555, No. 2 565	Lower Lower Lower	a b a
Laser output	555, No. 2 565	Upper Upper	a a

S-81231

2 μsec/div

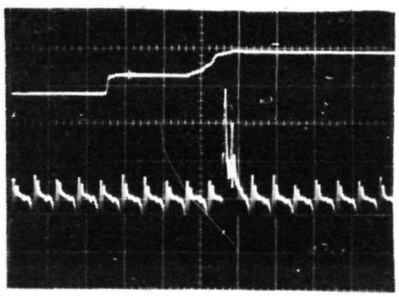

200 μsec/div

F-18542

Figure 14.--Simplified Block Diagram of Three-Oscilloscope Scheme for Double-Pulsing Ruby Laser and Sample Oscillogram.

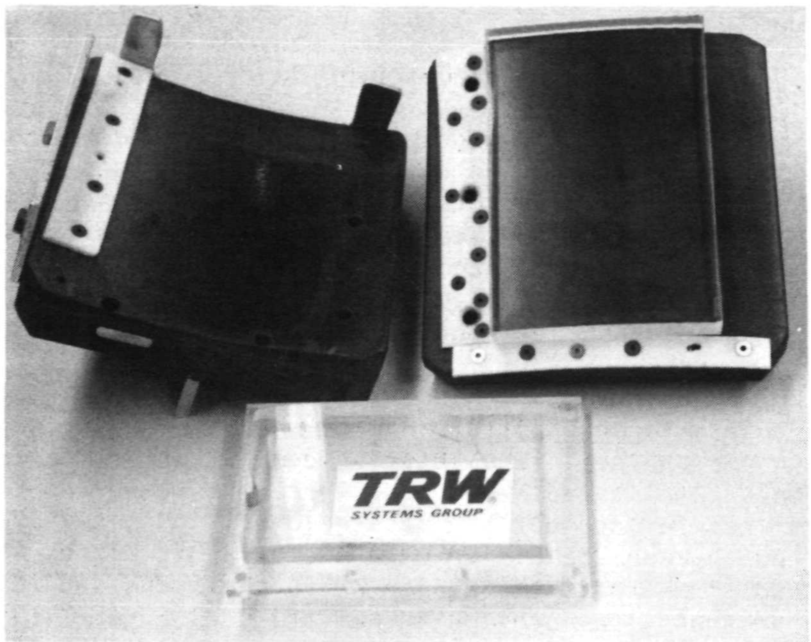

F-19085

Figure 15.--Plexiglas Viewing Window and Mold.

Automatic plate changer.--An automatic plate changer capable of storing up to 24 photographic plates was developed. The plate changer is essentially an ejector type of mechanism that will automatically feed and position the plates, holding them rigidly in position by suction during exposure; then eject and store the plates in a container. The plate changer was remotely operated by a flexible cable from the control panel.

HOLOGRAPHY TECHNIQUE

General Description

Holograms are a record of the microscopic interference between two coherent beams of light. One beam, called the reference beam, appears to come from a distant point source of light. The other beam, called the scene beam, is transmitted through the flow field. The scene beam is quite complex, particularly in the bright-field arrangement, since it is generated by the passage of laser light through a piece of ground glass. The scene beam is less complex in the dark-field arrangement because its source is light scattered from flow-entrained particles.

A microscopic interference pattern exists wherever the scene and reference beams pass through one another. The interference pattern is three dimensional and can be extremely complicated. When and where the scene and reference beams are coherent, the interference pattern is stationary in space. It can be recorded by a special photographic emulsion on a photographic plate. The photographic plate can be placed anywhere in the region where the scene and reference beams pass through one another; its location is not critical except in cases where the laser coherence is limited (as it was in this program). For such cases, the plate is located at the "path match position".

Whenever the plate containing the interference pattern (chemically fixed in the photographic emulsion) is illuminated by a beam that duplicates the original reference beam, the plate (hereafter referred to as a hologram) diffracts a beam that is identical to or a close facsmile of the original scene beam. Three-dimensional images are thus recreated from a hologram.

Double-exposing the photographic recording plate offers the simplest method of holographic interferometric comparison. The initial exposure records a stationary microscopic interference pattern on the plate. Changes in the optical paths throughout the scene that take place between the two exposures result in a slightly different pattern for the second exposure. Such a hologram displays two wave fronts whenever it is reconstructed or illuminated by a beam that approximately duplicates the reference beam. Changes in optical path length that occur between the two exposures and are multiples of a wavelength of laser light lead to constructive interference between the two reconstructed wave fronts. These regions of the image are seen as bright bands or fringes. Changes in optical path length that occur between the two exposures and are multiples of one-half wavelength lead to destructive interference or cancellation between the two wave fronts reconstructed from the holograms. These portions of the reconstructed image are seen as dark fringes that run through the scene. Neighboring fringes correspond to changes of optical path equal to one wavelength.

Double-exposed holograms are sensitive to changes in optical path as small as 1/20 of the wavelength of the laser beam. Changes in path that are a small fraction of a wavelength produce quasi-fringes or shadows in the reconstructed image.

The bright-field pulsed laser holographic apparatus (fig. 4) developed for this program recorded what are commonly known as transmission holograms. Optical path changes are produced by changes in the refractive index, not by a physical change in surface position. In such a situation, the optical path is defined as the integral of the refractive index over the physical path; namely,

$$\text{Optical path} = \int n \, dz \tag{1}$$

where n is the refractive index locally, and dz is the differential of physical path. For gases, the change in refractive index is directly proportional to the change in mass density (i.e., the change in the number of atoms per unit volume). Because the index of refraction of free or empty space is unity, the index can be related to the density as follows:

$$n - 1 = K\rho \tag{2}$$

where ρ is the mass density in lb/ft^3 (g/cm^3) and K is the constant of proportionality (the Gladstone-Dale constant). Its value can be computed from values of the refractive index and density given in published tables. For example, the refractive index of dry air at 59°F (15°C) and 29.92 in. Hg abs (76 cm Hg) pressure, and at 0.6943 microns (the wavelength of the ruby laser) is 1.0002753. Air at this temperature and pressure has a density of 0.0765 lb/ft^3 (0.001226 g/cm^3). At the wavelength of the ruby laser, the Gladstone-Dale constant for dry air, therefore, has a value of 0.225 cm^3/g.

Double-exposure transmission holograms measure the change in optical path that occurs between the two exposures of the holograms. Division of this change (eq. (1)) by the wavelength of the laser beam expresses the change in terms of wavelength, a value or representation that is more helpful in interpretation; namely,

$$S = \frac{\text{change in optical path}}{\lambda} = \frac{1}{\lambda}\int (n_f - n_i) \, dz \tag{3}$$

where n_f is the final index of refraction and n_i is the initial index of refraction. Eq. (3) can be written in terms of density change via eq. (2)

$$s = \frac{K}{\lambda}\int (\rho_f - \rho_i) \, dz \tag{4}$$

Change in density can be determined from an interferogram by solving eg. (4).

Because the holographic interferograms were recorded with a ruby laser, a relevant number is the number of fringes produced in air over a centimeter of path from a change in pressure of one atmosphere. This quantity is simply the change in the index of refraction divided by the wavelength of the ruby laser, which is 3.97 waves/cm/atm, or approximately 4 waves/cm/atm. For example, a 1-fringe shift over a span of 2 cm is an average change of 1/2 fringe per cm. Based on the value of 4 waves/cm/atm, such a change represents a 1/8 change in density (between the two exposures). The sensitivity of double-exposure holograms to changes as small as 1/20 of a wavelength over a path 2-cm long represents a miximum change of 1/40 fringe per cm and means that 1/160 atm is the minimum practical detectable change in density (4.7 mm Hg).

In summary, holographic interferograms are sensitive to optical path changes on the order of small fractions of the laser wavelength. A double-exposed hologram allows visualization of normally indiscernible aerodynamic changes in terms of clearly observable interference fringes.

Single-Exposure Holograms

A single exposure hologram may be defined as a hologram in which the microscopic interference pattern (i.e., the interference between the scene and reference beams, recorded by the photographic plate) is stationary throughout the exposure of the plate. Such a hologram reconstructs an identical three-dimensional image of the scene. It can be shown experimentally that an individual cannot distinguish between a holographic reconstruction of a scene and the scene itself under the same conditions of laser illumination (ref. 9).

The microscopic interference pattern at the photographic plate (at the time of recording) is stationary in space if all parts and paths through the holocamera are stationary to less than 1/20 of the wavelength of laser light. In terms of exposure time, this condition establishes a velocity below which objects will be recorded satisfactorily, and above which they will be recorded with diminishing intensity (if at all). In this program, the holograms were recorded with a Q-switched ruby laser of typically 50-nsec pulse duration. Dividing this duration into the 1/20-wavelength stability condition gives a limiting velocity of 70 cm/sec. Elements or parts of the scene that move at speeds of greater than 70 cm/sec will not be recorded by a hologram exposed with a 50-nsec laser.

Two types of holograms were recorded: (1) bright-field holograms and (2) dark-field scattered-light holograms. In the bright-field holographic arrangement (fig. 5), the rotating blades were not a part of the holographic optical arrangement. The blades only passed through the scene volume of the holocamera. The blades were seen only in silhouette against the bright background produced by the ground-glass diffuser. Single-exposure holograms taken with the blades rotating were essentially identical in appearance to holograms taken with the blades at rest, except for some minor differences. With the blades stationary, light that was reflected from the blade surfaces could be seen in the reconstructions. When the blades were rotating, this reflected light was not reproduced in the reconstruction, since the optical path for light scattered from the blades surfaces during exposure of the hologram was in excess of the 1/20-wavelength limit. Except for the lack of highlights with the blades rotating, the two holograms appeared identical.

Reconstruction of single-exposure holograms recorded with the stage operating at design speed showed that components of the holographic apparatus were not vibrating with amplitudes in excess of 1/20 of the wavelength of the laser light. Satisfactory single-exposure bright-field holograms substantiated that induced vibration levels of the holocamera were significantly lower than originally anticipated, and that holocamera vibration would not impose any serious problems.

The recording further showed that the aerodynamic phenomenon was weak, and that throughout the flow field, there were no regions where the optical path changed more than 1/20 of a wavelength during the 50-nsec duration.

The dark-field scattered-light holograms were quite different from the bright-field holograms. In the scattered-light holograms, particles were recorded by their scattering of laser light. This made the particles a part of the holographic apparatus and subject to the 1/20-wavelength path restriction. At the stage design speed, particles entrained in the flow field moved too rapidly to be recorded with a ruby laser with a 50-nsec pulse duration. Tests were therefore limited to an operating speed of approximately 10 percent design speed in lieu of shortening the laser pulse duration.

Examples of the hologram reconstructions taken with the blades at rest are shown in fig. 16. The figure on the left was taken with the holocamera in the bright-field or "focused-ground-glass" configuration and shows highlights due to the scattering of light from blade surfaces. As indicated previously, these highlights were not present in holograms recorded when the blades were rotating. The figure on the right was made with the holocamera in the scattered-light arrangement. For this photograph, the copy camera was focused on the blade nearest the viewing window. The background in the right photograph was due to dirt on both the scene window and the surfaces of the intermediate focusing lenses. The "impact" of the focused laser beam on the viewing window is seen in the foreground of the photograph of the scattered-light hologram.

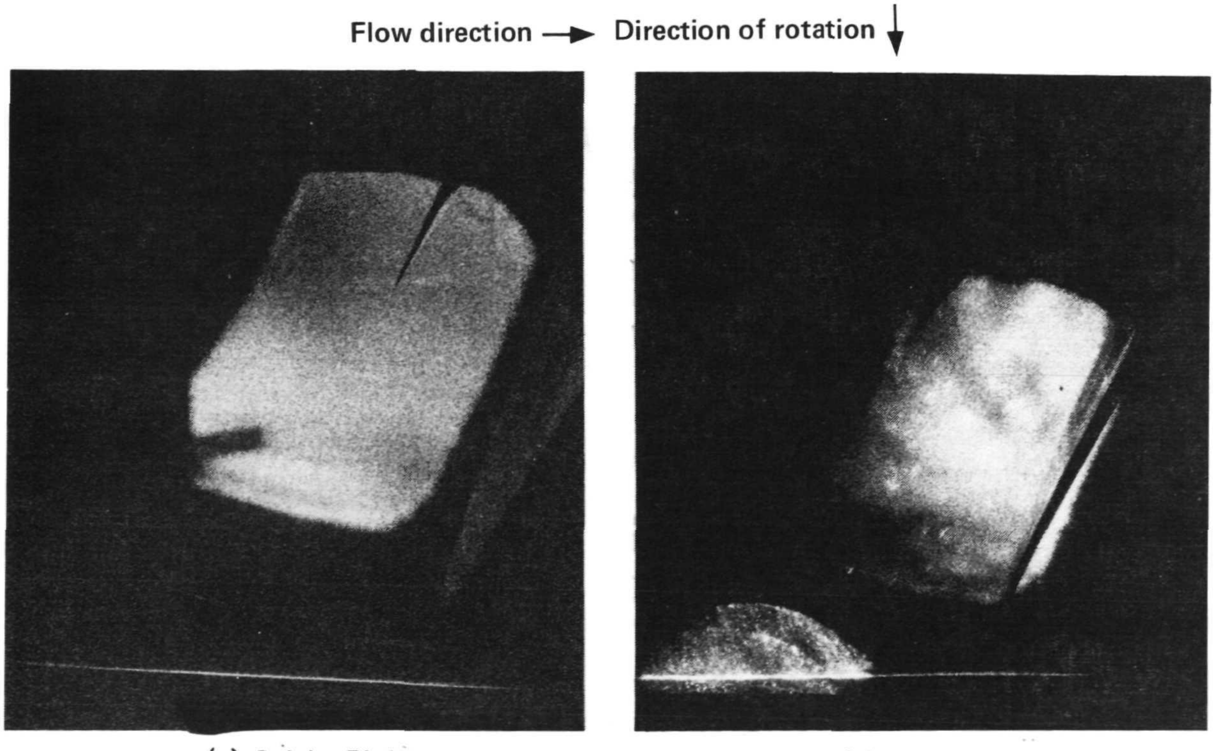

(a) Bright Field.

(b) Dark Field.

F-17738

Figure 16.--Single-Exposure Holograms of Rotor Blade Passage at Rest (Zero Speed).

Two exposures of the scattered-light holograms were made to show the relative positions of particles at two different points in time; however, no interferometric or phase information was obtained. Special single-exposure bright-field holograms also were attempted. The laser pulse duration was increased from the nominal 50-nsec duration to 1 to 2 μsec. This was achieved by increasing the optical cavity length to 19.7 ft (6 m). Increasing the laser pulse duration made the hologram even more sensitive to optical path length changes produced by the flow field. The results were moderately successful, but not as successful as for the holograms in which the laser emitted two distinct pulses in rapid succession. This type of hologram is discussed in the following paragraphs.

Double-Exposure Holograms

The double exposing of a hologram provides a method for visualizing the shock-induced density changes in the air flowing through the blade passage. The holocamera is in the bright-field arrangement for this type of recording. Density changes are visualized in the fringe pattern seen in the hologram. These are caused by optical path changes that occur between the two exposures of a hologram. In double-exposure holography, the first exposure provides a reference to which the second exposure is compared. The reconstruction of the hologram recreates the two wave fronts at the same time; these then interfere with one another, showing the changes in optical path in terms of the optical interference pattern. The steps in recording a transmission holographic interferogram are diagrammed in fig. 17. In this figure, the scene beam is shown as

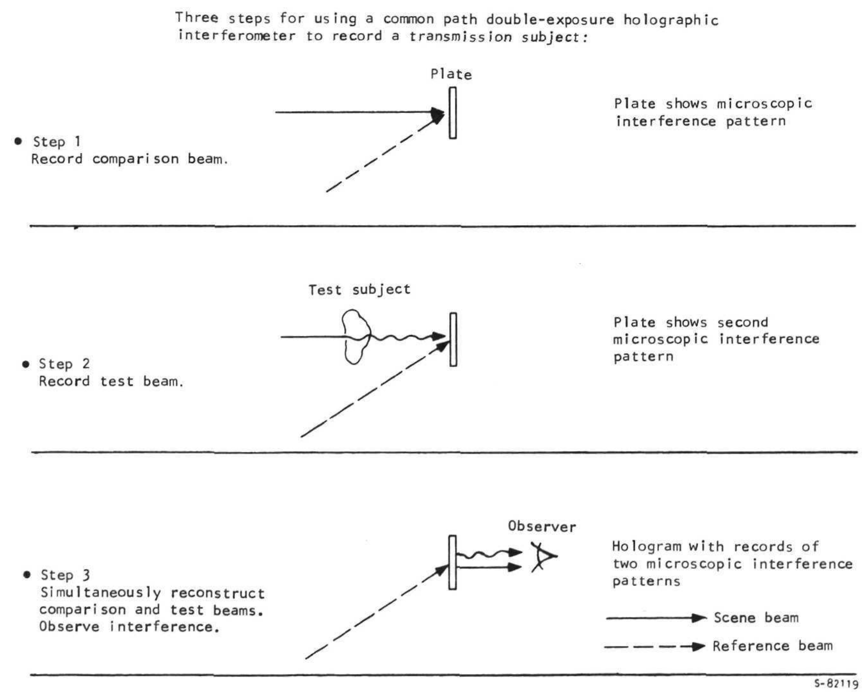

Figure 17.--Diagram of the Procedure for Recording and Reconstructing a Double-Exposure Holographic Interferogram.

a solid line, and one ray of the reference beam is shown as a dotted line. As discussed earlier, the photographic plate records the microscopic interference pattern due to the passage of the scene beam through the reference beam. After the first exposure, a change is introduced into the scene path. In the example, it is shown as a transparent object that shifts the phase of the scene beam relative to its original value. During the second exposure, a second microscopic interference pattern is recorded by the plate. The plate is developed, then illuminated with a beam that duplicates the original reference beam. The two microscopic interference patterns, developed in the plate, create (by diffraction) the original wavefronts, shown simultaneously. Because the wavefronts interfere with one another, the phase change that occurred between the two exposures is seen in terms of gross optical interference fringes.

In recording aerodynamic phenomena, the first exposure generally is made under quiescent conditions, the second exposure is made in the presence of the event, and the holographic interferogram then shows the difference. In theory, the absolute change in aerodynamic density can be calculated from such a hologram by diligent application and interpretation of eq. (4).

An example of a double-exposure hologram is shown in fig. 18. This example represents one of the early recordings obtained during initial installation and checkout of the holocamera assembly. The first exposure was recorded with the rig at rest, and the second exposure was made with the rig rotating at 60 percent design speed. The hologram reconstructs the two images simultaneously and these interfere to give the finite fringe pattern seen in the figure. The photographs differ only by the viewing angle. The ghost image of the blades when the rig was at rest is seen in the two right-hand figures. The fringes seen are due to changes in optical path length, resulting from the combination of aerodynamics and mechanical movement of the rig relative to the holocamera. Flow direction as viewed is from left to right. A circuit around the blade shows a discontinuity in the number of fringes. Knowing the path length, this difference gives the density difference directly. Thus, near the top of the right-hand figure, a three-fringe difference in the number of fringes from the pressure to the suction surface of the blade can be seen. Because the view is skewed along the blade, the path length is estimated to be 1.97 in. (5 cm). Thus, at this point, a 0.6 λ/cm fringe change is measured across the blade. Based on the 4 λ/cm/atm constant derived earlier, a density change of $\sim$0.15 atm is estimated from the suction to the pressure side of the blade at the point in consideration.

The S-shaped nature of the fringes is due primarily to mechanical movement of the test rig relative to the holocamera. Hooking of fringes at the edge of the window is due to warpage of the window.

Rapid Double-Exposure Holograms

Double-exposure holograms are not restricted to the separation in time of the two holographic exposures. The hologram only visualizes, in terms of optical interference phenomena, the change in optical path that occurs between the two exposures. Shock waves in any supersonic section are characterized

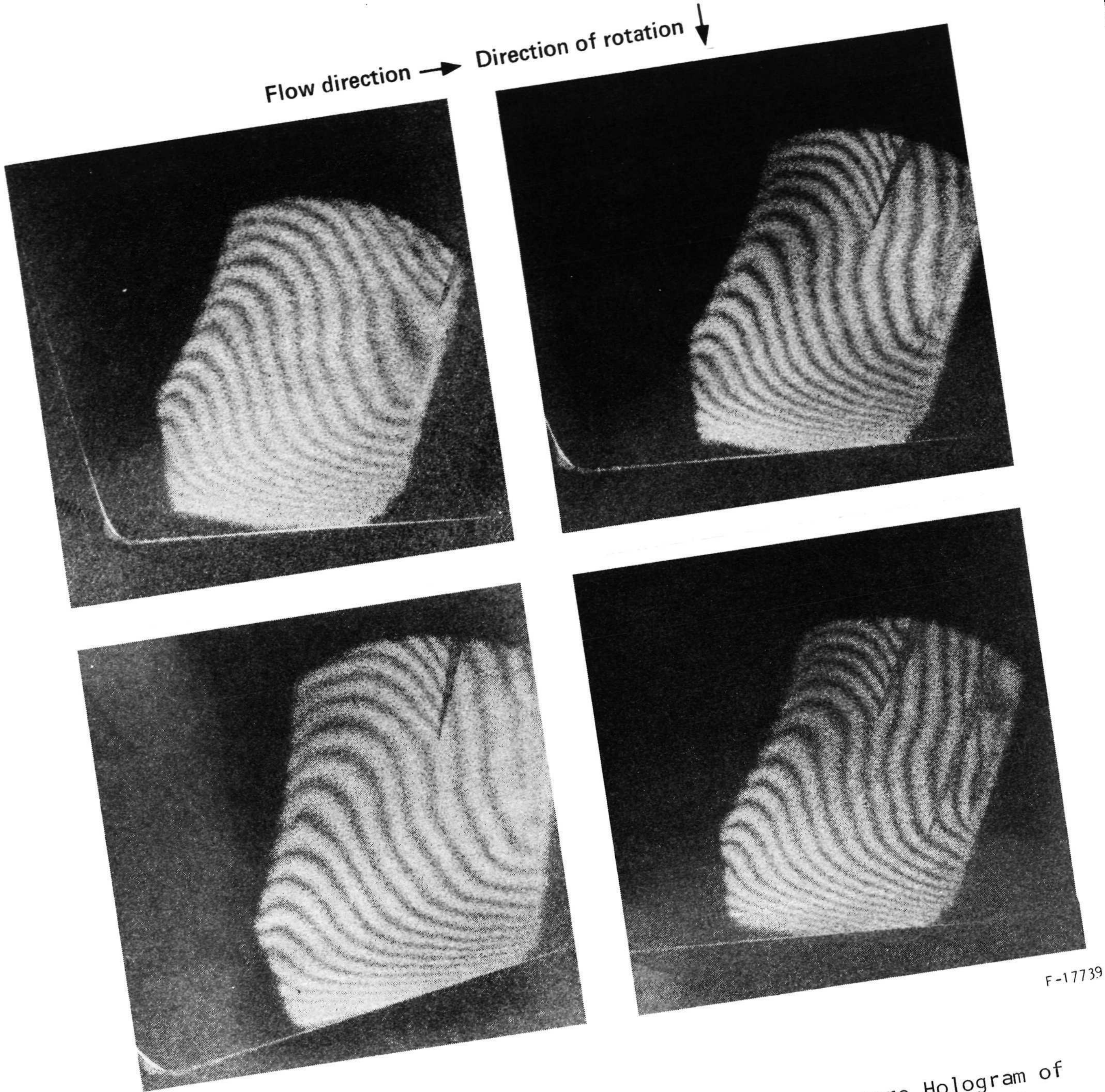

Figure 18.--Various Viewing Angles of a Double-Exposure Hologram of Rotor Blade Passage - Initial Exposure Taken at Rest, Second Exposure at 60 percent Design Speed.

by a sharp density gradient. The change in density in the flow field constitutes a change in light path and will change the interference pattern at the hologram. In a rapid double-pulsing of the laser, the shocks move slightly between pulses, which greatly enhances the image recorded on the hologram. This technique offers a unique method for visualizing and identifying shock fronts three-dimensionally.

The proper pulse separation was determined experimentally. Fig. 19 shows three examples. Example (a) is an abnormally long single-exposure hologram for which the pulse duration was approximately 1 μsec. Examples (b) and (c) are double-exposure holograms with separation times of 5 μsec and 30 μsec, respectively. For example (c) blade movement during this time interval was nearly 25 percent of the blade passage width. The double-exposure holograms recorded with 2- and 5-μsec time separation (example (b) of fig. 19) appeared to provide the best rendering of the shock structure. Therefore, most of the double-exposure holograms taken during the program were recorded with a 2- to 5-μsec time separation. Double pulsing of the laser within these pulse intervals required special development of the laser illuminator. Holograms of the type shown in (b) and (c) of fig. 19 are referred to as "rapid double-exposure holograms" to distinguish them from double-exposure holograms recorded at different operating speeds or flow conditions. (The latter were referred to throughout the program as "long double-exposure holographic interferograms.")

Double-Exposure Scattered-Light Holograms

The new experimental aspect of the program was the determination of flow velocity from double-exposure scattered-light holograms of particles entrained in the flow stream. In scattered-light holography, light is scattered off the moving particles. As a result, the particles become part of the holographic apparatus. The particles are then subject to holographic motion limitations; to be recorded, the optical path of the scattered rays should not change more than 1/10 of a wavelength of laser light during the exposure of the hologram. A particle that moves a little more than 1/10 of a wavelength reconstructs only dimly, and one that moves many wavelengths during the exposure time does not reconstruct at all (ref 10).

The flow velocity at the design speed for this application is high for a conventional 50-nsec Q-switched ruby laser. In scattered-light holography, motion of the microscopic interference pattern is a function of the relative direction between the illuminating beam, the direction of scattered light, and the motion of the scattering particle. The forward scattering condition is least sensitive to particle motion. For this reason, the holocamera was designed to use forward-scattered light. Motion of particles entrained in the flow field is essentially perpendicular to the direction of the converging scene beam. A simplified view in fig. 20 shows the direct beam focused on a beam stop in front of the hologram and fig. 21 shows an enlarged simplified portion of the laser particle scattering region. Only light scattered by the particles reaches the hologram. A ray is shown being scattered at an angle relative to a ray of the direct illuminating light.

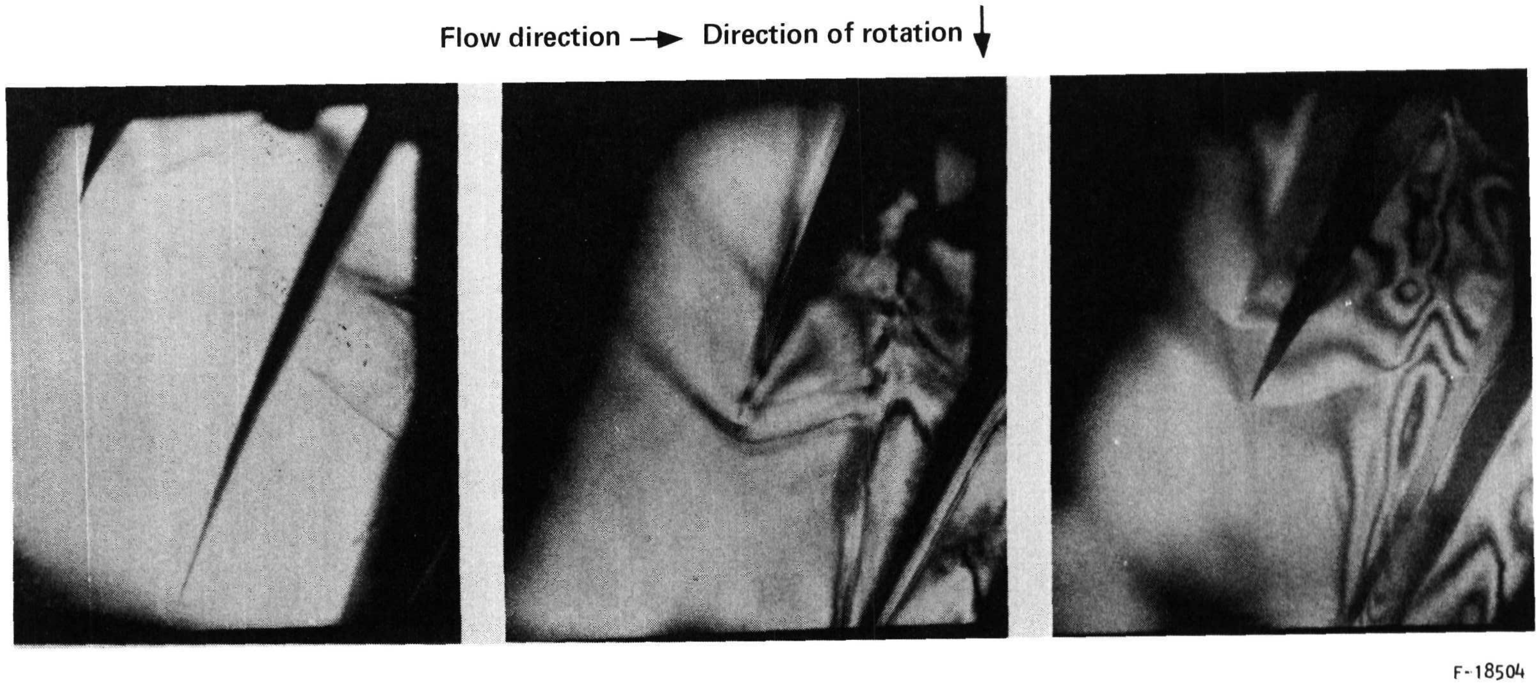

(a) Single-Exposure (Hologram 90).

(b) Rapid, Double-Pulse, 5 μsec Pulse Separation (Hologram 106).

(c) Rapid, Double-Pulse, 30 μsec Pulse Separation (Hologram 107).

Figure 19.--Reconstruction of Single-Pulse and Rapid Double-Pulse Holograms with ~1 to 30 μsec Pulse Separation.

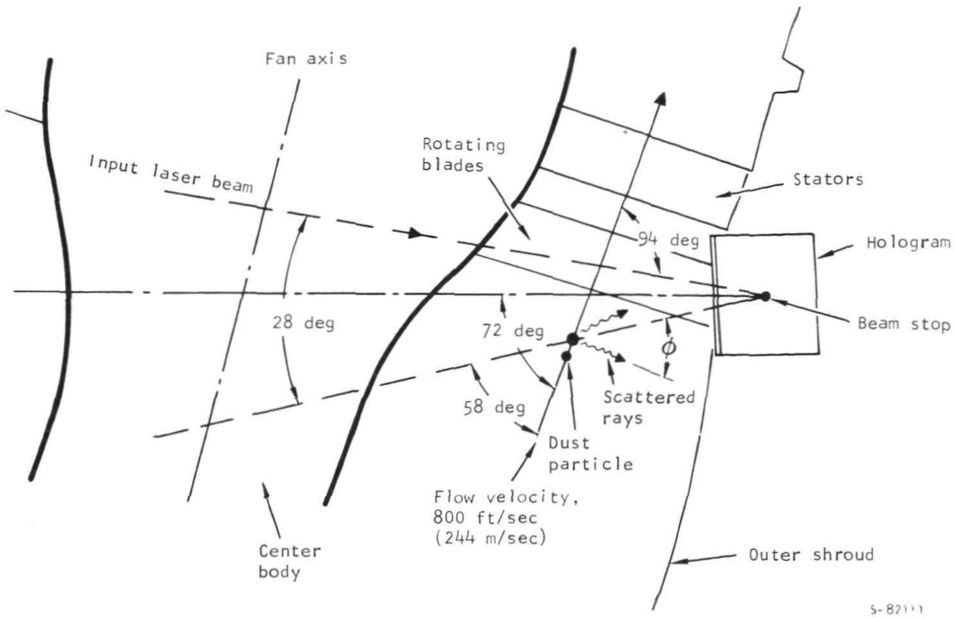

Figure 20.--Schematic of Skewed Holographic Arrangement for Scattered-Light Analysis (Flow Varies in Angle Relative to Laser Beam Direction from 58 to 94 deg).

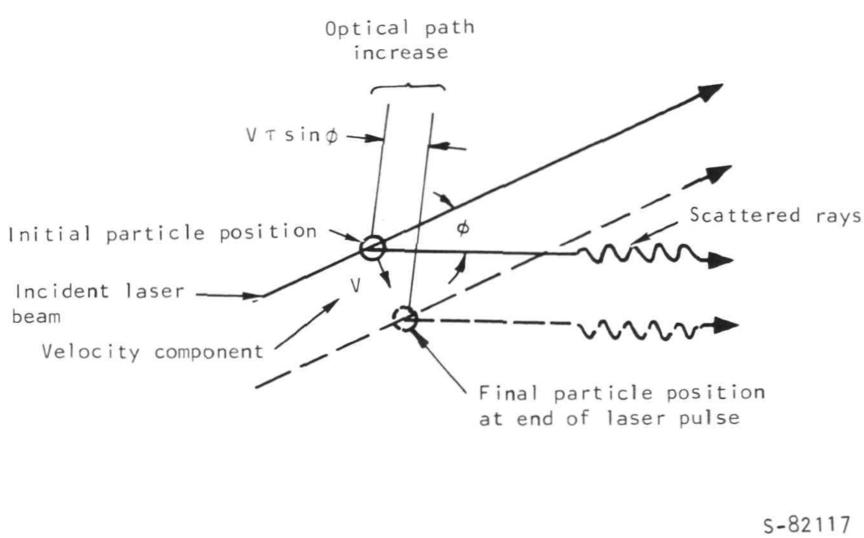

Figure 21.--Enlarged Portion of Particle Interaction Showing Optical Path Increase due to Particle Motion.

The direct radiation converges onto the beam stop with an angle of convergence of 28 deg. This was determined by the diameter of the intermediate focusing lenses. In the actual setup, the axes of the converging scene beam and the flow field are skewed at an angle of 72 deg, which is the alignment of the holocamera to the axis of the fan rotor.

The two particle positions shown in fig. 21 correspond to the positions of a scattering particle at the beginning and end of a single laser pulse. The incident laser beam direction is shown along with the direction of scattered light. The scattered light, as in fig. 20, is shown as being scattered at an angle of ϕ. Only the component of velocity perpendicular to the direction of the incident or unscattered light is effective in changing the optical path for the arrangement shown in fig. 20. The component of velocity parallel to the incident beam does not change the optical path and thus can be ignored. Considering only the perpendicular component V, it can then be shown that the change in optical path Δ over a pulse duration τ for rays scattered at an angle ϕ with respect to the incident light is

$$\Delta = V \tau \sin \phi \qquad (5)$$

For the scene-reference beam interference pattern to be stationary at the hologram,

$$\Delta \lesssim \lambda/10$$

where λ is the wavelength of the laser light. Substitution into eq. (5) derives the range of angles over which the hologram brightly reconstructs:

$$\phi \lesssim \sin^{-1} \frac{\lambda}{V \tau 10} \qquad (6)$$

Eq. (6) establishes limits on either or both flow velocity and scattering angle for a given laser wavelength and pulse duration. Solving eq. (6) for the scattering angle ϕ and given:

V = 800 ft/sec (244 m/sec)

λ = 0.6943 microns

τ = 50 nsec (pulse duration of a conventional Q-switched ruby laser)

yields the scattering angle

$$\phi \simeq 1/3 \text{ deg}$$

Light scattered at less than 1/3 deg will result in a stationary interference pattern at the hologram. The reconstruction of such a hologram will show each scattering point or particle as a bright object against a dark background for scattering angles less than 1/3 deg. For angles greater than 1/3 deg, the reconstructed image becomes dim, becoming invisible at angles in excess of a few degrees. In this condition, the inability to reconstruct an image of the scattering particles was the result of motion of the interference pattern at the hologram due to change in optical path during the exposure period. For the condition described, the particle appears as a bright scattering object over a very restricted angle above the incident or unscattered position (i.e., angular cone of 2/3 deg).

An obvious method of increasing the range of angles over which the particles brightly reconstruct is to decrease the laser pulse duration. Using eq. (5), the pulse duration required for all particles in the field to brightly reconstruct within the angular limitation of the viewing window ($\phi_{max} = \pm 18$ deg) can be computed. For an inlet flow velocity of 800 ft/sec (244 m/sec),

$$\tau \lesssim \frac{\lambda}{10V \sin 18} \lesssim 0.9 \text{ nsec}$$

Such pulses are abnormal to conventional Q-switched ruby laser performance. Short pulses have been achieved with electro-optical techniques. Pulses as short as 2 nsec have been produced with spark gaps fired by a laser pulse that short-circuits a Kerr cell while light is passing through it. Implementation of such techniques was beyond the scope of the program. Instead of reducing the laser pulse duration, the flow velocity field was decreased to accommodate the 50-nsec laser pulse duration. Feasibility tests were run with the rig rotating at only 1000 rpm (≅8 percent design speed). The resulting holograms verified the technique of determining velocity from a double-exposure scattered-light hologram. At this speed, flow velocities were 33 ft/sec (10 m/sec).

HOLOGRAPHIC TESTS

Bench Test

Both the bright-field and dark-field holographic installations were breadboarded and bench tested prior to final construction of the holocamera. Bench testing was particularly important in the case of the scattered-light arrangement, where feasibility had to be established by actual test. The breadboard setup of the bright-field and scattered-light arrangement showing the fan rotor blade mockup, holocamera, and nebulizer for injecting the particles is presented in fig. 22.

The scattered-light arrangement was tested by recording holograms of particulate matter that was either blown or convected into the scene volume (i.e., into the area between the focusing lens set and beam stop). The nebulizer (plastic bottle forward of the rotor blade) used to blow 40- to 50-micron particles into the scene also is shown in fig. 22. The nebulizer was filled with either phenolic particles or glass microballoons. Both samples consisted of particles principally in the 30- to 50-micron size range. Photomicrographs of the particles are shown in fig. 23.

To test the sensitivity of the scheme for particles of even smaller size, incense smoke was used as the scattering source. (Incense had been used in other applications of scattered-light holography and produced particles in the 1- to 3-micron size range.)

Photographs of reconstructed holograms for the three different particles are shown in fig. 24. The incense is shown in view (a) and appears cloud-like in character. The glass microballoons shown in view (b) are clearly more granular in appearance and can be seen as bright points of light. The phenolic particles, view (c), which range in size from 30- to 50-microns, tend to form in clusters, resulting in agglomerates several hundred microns in diameter. The phenolic particles also are granular in appearance. These tests established the feasibility of holographically recording particles of this size range.

All scattered-light holograms were recorded with a conventional Q-switched ruby laser illuminator, a laser without any coherence-improving elements (such as a chlorophyll dye cell) within the laser cavity. As a result, many of the holograms showed the effects of the limited coherence of the Kerr cell Q-switched ruby oscillator. Holograms for quantitative analysis should be recorded with a more coherent oscillator.

Shakedown Test

The holocamera, laser, and optics were aligned to achieve the precise path matching of the reference and scene beams required to produce high-quality, brightly reconstructing holograms. Path matching appears to be a relatively simple adjustment, to match the physical distance of the reference beam to that of the scene beam path with mirrors. This adjustment is complicated,

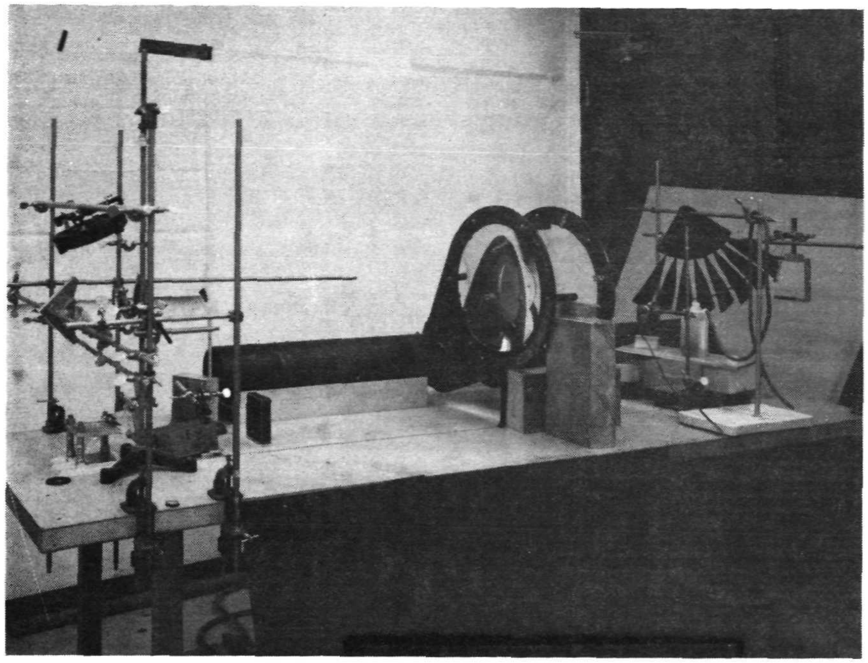

(a) Mockup of Breadboard Setup

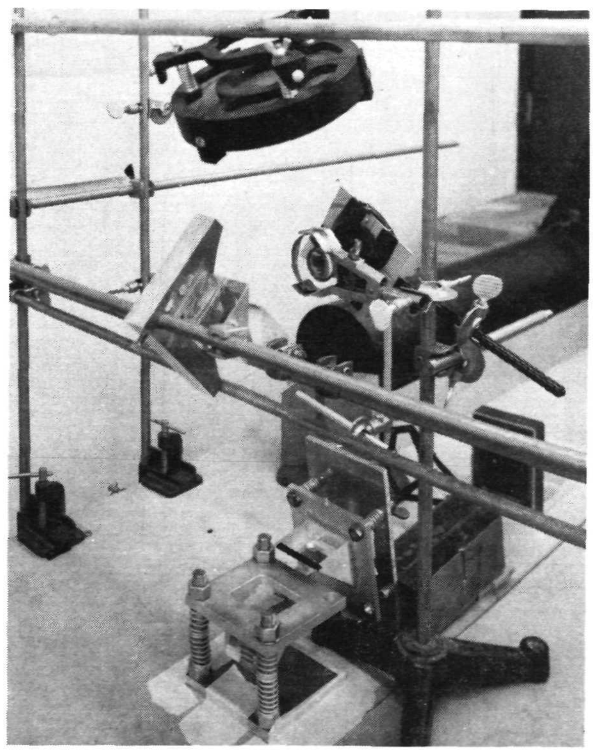

(b) Optical Elements. F-18498

Figure 22.--Breadboard Setup of Scattered-Light Holographic Arrangement showing Transonic Fan Blade Mockup, Hologram, Nebulizer for Injecting Particles, and Beam Forming Elements.

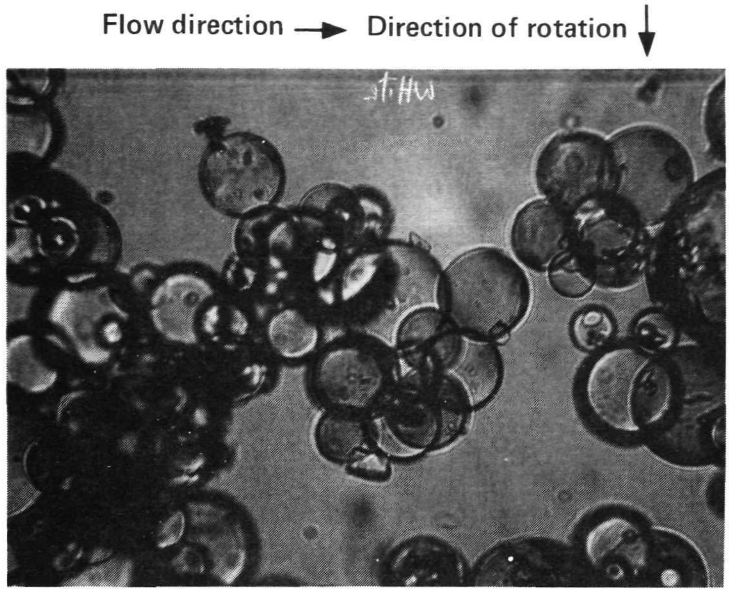

(a) Glass Particles.

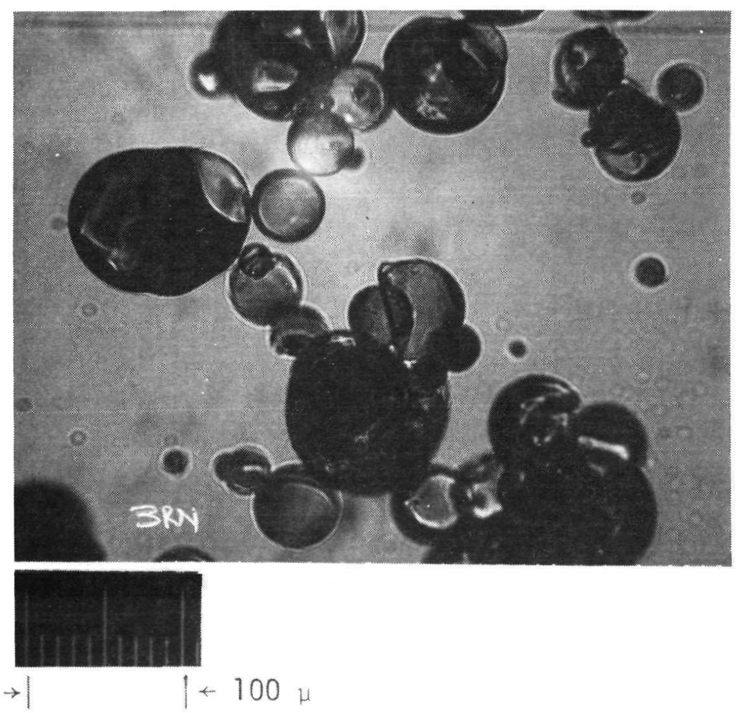

(b) Phenolic Particles.

F-18518

Figure 23.--High-Magnification Photomicrographs of Sample Microballoons.

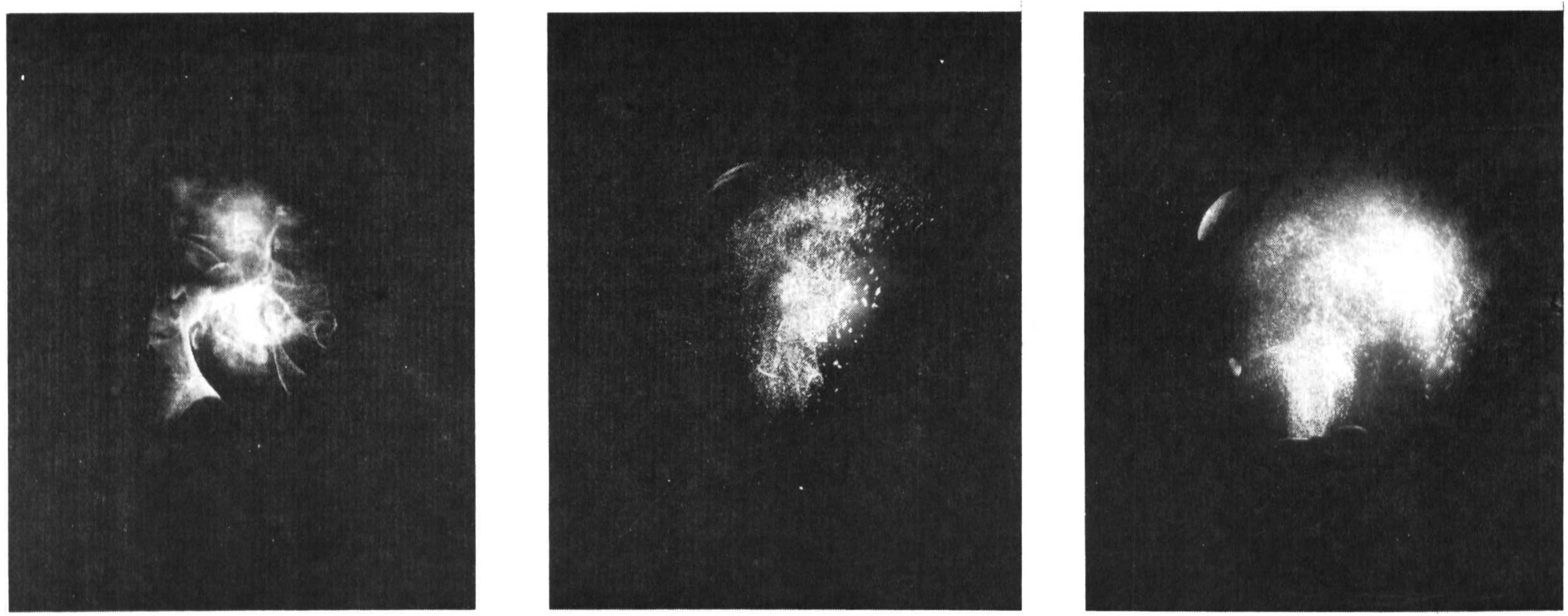

F-18541

(a) Incense Smoke (1 to 3 microns).

(b) Microballoons (30 microns).

(c) Microballoons (30 to 50 microns).

Figure 24.--Reconstruction of Dark-Field, Scattered-Light Holograms of Various-Sized Particles from 1 to 50 Microns.

however, by the windows, which increase the optical path length by an amount equal to the physical path, τ, multiplied by the difference between the refractive index of the window and that of vacuum where:

$$\Delta Path = (n - 1)\tau$$

In essence, path match is best determined by recording holograms with a laser operating incoherently. Coherence is reduced by removing the resonant reflector on the laser cavity and replacing it with a single dielectric output mirror. This permits the laser to oscillate over a wide band of frequencies. The coherence actually reduces to approximately 0.10 in. (0.25 cm). A hologram recorded with such a laser reconstructs only to a band in which the reference and scene beam paths differ by this amount; however, once the proper alignment of the holocamera, laser, and optics was achieved, further adjustments to the holocamera installation were not necessary.

Both single- and double-exposure holograms were successfully recorded during the shakedown test. Single-exposure holograms were made with both the bright-field focused ground glass and the dark-field scattered-light holographic arrangements. A double-exposure hologram of the rotor blade passage with the stage initially at rest and operating at a speed of 60 percent of design speed was shown earlier (see fig. 18). At this time, no attempt was made to synchronize laser firing with the exact blade position.

Double-exposure holograms were of two types, long-interval double exposures where both speed and operating conditions were changed, with exposures separated by time intervals as much as 5 to 7 min, and rapid double exposures where the blade moved some finite distance (limited to less than one blade passage) with a pulse separation of 2 to 5 μsec. The quality of holograms recorded was very encouraging and clearly showed the three-dimensional shock structure within the rotating blade passage. The most interesting holograms recorded during this test period were achieved when the laser emitted either an abnormally long pulse (estimated at 0.10 to 0.4 μsec) or rapid pulses separated by approximately 2 to 5 μsec. These holograms accurately portrayed aerodynamic phenomena (shock waves characterized by abrupt density changes) within the blade rows. (An example is fig. 19(a), shown earlier.)

Based on the results of these tests, improvements in the test technique and modifications to the laser, holocamera, and test stage were implemented.

Final Test

More than 600 single- and double-exposure holograms were taken during the initial checkout, shakedown, and final test phases of the holography program. Of these, approximately 350 were recorded during the final test period after modifications to the laser, holocamera, and test stage had been implemented. The holograms covered the complete operating speed range from 60 to 110 percent design speed and from choked flow to near stall conditions.

The holograms recorded during the final tests were greatly improved over the earlier recordings, particularly from the standpoint of image quality, larger effective viewing image area (achieved by recording a series of holograms at incremental blade positions), and a substantial reduction in interference fringes due to combinations of window deficiences and vehicle vibration. A tabular summary of the data points and corresponding holograms that were selected for reconstruction and analysis is presented in table 1. The operating conditions at which the series of holograms were taken are superimposed on the overall stage performance map shown in fig. 25.

Four basic types of holograms were recorded: (1) long-pulse, single-exposure, (2) rapid double-exposure, (3) long double-exposure, and (4) scattered-light.

Long-pulse, single-exposure holograms were attempted by modifying the laser to emit 2-μsec pulses. The long pulse duration was achieved by repositioning the mirrors (99 percent mirror) approximately 20 ft (6.1 m) apart to lengthen the resonator. The 2-μsec pulses were consistently achieved; however, the results of these holograms were disappointing. The long pulses accentuated the fringes associated with the major shock waves, but these holograms lacked detail, making them difficult to interpret during reconstruction.

Rapid double-exposure holograms were made with a laser emitting two pulses within a very short time span. A 2- to 5-μsec pulse separation was found to produce the best results. By double pulsing, the shock fringes moved slightly between pulses. This greatly enhanced the patterns recorded in the hologram, thus making the shock fronts easily identifiable. Most of the holograms were made using this technique. These holograms were made at speeds of 80, 90, 95, 100, and 110 percent design speed. Thirty six holograms were selected for 8 different operating speed and flow conditions. Six additional holographs were made where the speed was varied from 80 to 100 percent design speed along a constant operating line.

Long double-exposure holograms were made with the first exposure at 60 percent design speed and the second exposure at 90, 95, or 100 percent design speed. These holograms were made with the thinner, 0.25-in.-thick (0.64-cm) windows. The first double-exposure holograms indicated the larger window deflected under pressure. The final holograms were, therefore, made with the original scene window and the thinner viewing window. Six holograms were selected for a range of operating speed and flow conditions.

A limited number of dark-field scattered-light double-exposure holograms were made. Effort was concentrated on recording scattered-light holograms that would demonstrate feasibility of the technique for determining flow velocity. Most holograms were recorded with the stage operating at a 1000 rpm (~8 percent design speed). Microballons ranging in size from 30 to 50 microns were injected into the flow stream. Successful holograms were made showing clouds of particles in the blade passage. Pulse separation was typically 40 to 50 μsec, giving a displacement of particles sufficiently large to identify individual particles. One representive scattered-light hologram was selected as a typical example.

TABLE 1

FLOW VISUALIZATION TEST
DATA SUMMARY

Data Point	Reading *	$\frac{N/\sqrt{\theta}}{(N/\sqrt{\theta})_{des}}$	$\frac{W\sqrt{\theta}/\delta}{(W\sqrt{\theta}/\delta)_{des}}$	Rotor P_{T9}/P_{T5}	Rotor η_{ad}	Stage P_{T12}/P_{T5}	Stage η_{ad}	Hologram
				Rapid Double Pulse				
1	103	0.90	0.980	1.352	0.885	1.321	0.808	311 312 313
2	106**	0.90	0.942	1.545	0.865	1.524	0.834	318 319 320
3	104	0.95	1.019	1.396	0.879	1.348	0.784	286 287 289 323 324 325 326
4	118**	0.95	0.995	1.640	0.900	1.604	0.855	278 279 280 332 333 334
5	107	1.0	1.040	1.429	0.851	1.369	0.743	164 290 292 293 335 337 338
6	128**	1.0	1.041	1.545	0.867	1.505	0.812	294 339 340 341 342 343
7	126	1.0	1.031	1.724	0.897	1.669	0.837	344 345 346
8	113**	1.10	1.082	1.653	0.833	1.597	0.770	167
9	-	1.0 0.96 0.92 0.90 0.86 0.80						347 349 351 352 356 358
				Double-Exposure Hologram				
10	103	0.90	0.980	1.352	0.885	1.320	0.811	453
11	104	0.95	1.019	1.396	0.879	1.348	0.784	456
12	107	1.0	1.040	1.429	0.851	1.369	0.743	462
13	128	1.0	1.041	1.545	0.867	1.505	0.812	470
14	126	1.0	1.031	1.724	0.897	1.669	0.837	460
				Scattered-Light Hologram				
15	-	0.079						512

S-82151

* Corresponds to reading numbers for performance data for uniform inlet flow test of ref. (6).
** Blade element performance data presented in Appendix A.

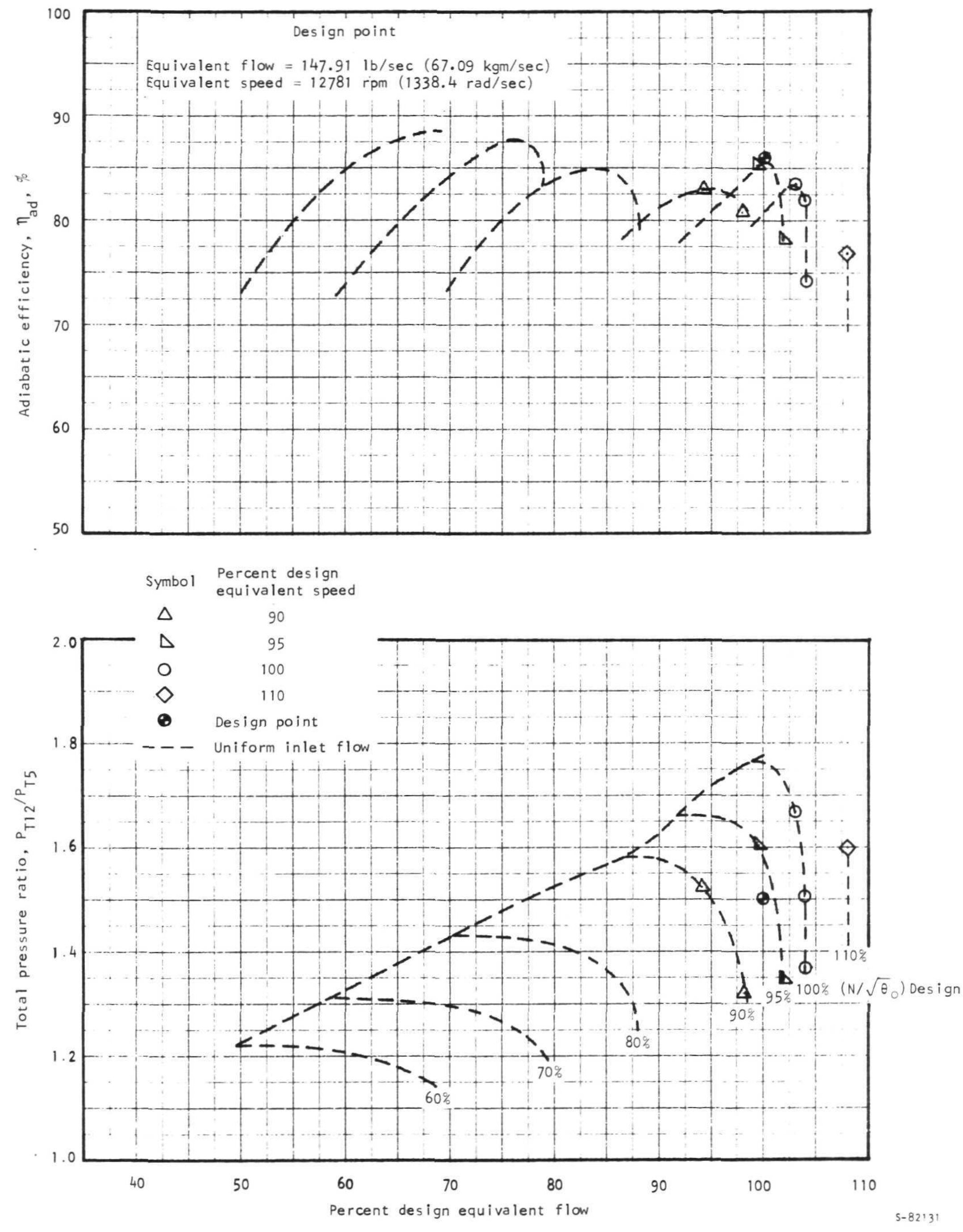

Figure 25.--Flow Visualization Data Points Superimposed on Overall Stage Performance Map.

Window clouding from oil centrifuged from the front bearing seal was a major problem during the test. The windows were cleaned repeatedly during the test to maintain a clear field of vision and to minimize light scattering from particles adhering to the window.

ANALYTICAL PROCEDURES FOR RECONSTRUCTING AND INTERPRETING HOLOGRAMS

Ideally, holograms that are recorded with a ruby laser should be reconstructed with a ruby laser to produce the most accurate reconstruction. Such an approach is not practical, however, because ruby lasers are pulsed devices that are inefficient when operated continuously or at high repetition rates. Therefore, ruby laser holograms are reconstructed with continuous-wave helium-neon lasers. The difference in wavelength between the helium-neon and ruby lasers of approximately 10 percent introduces slight astigmatism, but this can be seen only at microscopic levels. Helium-neon lasers provide an efficient source of light for reconstruction and photography of any ruby laser hologram.

A 15-mW helium-neon laser (Spectra-Physics Model 124) was installed in the test cell adjacent to the fan control room. The laser beam was diverged to duplicate the divergence of the original reference beam in the holocamera. The beam was reflected from a mirror at an angle of 45 deg relative to the horizontal, duplicating the original angle of the reference beam in the holocamera. The holograms were placed in a holder and positioned for maximum brightness in reconstruction. In viewing the holograms, the blades are observed through the viewing window. In long double-exposure holograms, one can observe three-dimensional images showing fringe patterns. In rapid double-exposure holograms (see fig. 19), fringes were confined to shock fronts. The scattered-light holograms (see fig. 16) showed the scattering of light from dust on the two windows, from the blades and from entrained particles.

The methods used to photograph and interpret the images seen in the holograms are discussed in the paragraphs that follow.

Hologram Reconstruction Method

The ideal method of interpreting a hologram is to examine it directly using the proper optical aids such as telescopes, microscopes, and cathetometers. For reporting purposes, however, the results must be presented photographically.

Photographing a holographic image is accomplished with a conventional copy camera. Use of a 4 by 5 in. (10.2 by 12.7 cm) bellows camera with a focusing screen is the best way to compose the picture. The camera is placed in front of the reconstructed hologram and focused on the region or point of interest. Photographs can be recorded on Polaroid Type 52 film. Polaroid Type 55 positive-negative film is ideal for making negatives from which enlargements can be made. The "f-stop" or aperture ratio on the camera is used to control the depth of field of the image.

Holograms also can cast a real image. Real images are projected when it is necessary to see or photograph fine detail with a microscope or short focal length lenses. In this method of reconstruction, the reference beam is projected through the hologram in the reverse direction from which it was originally projected. The hologram (which has no sense of the original direction of the reference beam) projects a real image into space. The rays that form the image flow in the opposite direction, making the image pseudoscopic. These real images can be focused on screens, and also can be recorded directly on photographic film without the aid of any camera lens. They also can be examined with short working distance microscopes. Aperture ratio (f-stop) and viewing angle can be controlled by masking the hologram.

A variation of the real image approach to reconstructing a hologram is to pass the raw beam from a helium-neon laser through the hologram in the reverse direction of the reference beam, and at the same convergence as the original reference beam divergence. The result is a real-image "pinhole" camera reconstruction of a hologram. Such a reconstruction has almost infinite depth-of-focus. The image is projected directly on film.

Hologram reconstructions were photographed using direct photography of the virtual image, projected real images (particularly of scattered-light holograms), and direct reference beam projections. Reconstructed holograms of rapid double-pulse, long double-exposure, and scattered-light holograms are presented in figs. 26 throrough 32. Figs. 26 through 29 show a series of photographs taken from reconstructed rapid double-pulse holograms recorded at 90, 95, 100, and 110 percent design speeds, respectively. A photograph of a reconstructed double-exposure hologram is shown in fig. 30. A scattered-light reconstruction is shown in fig. 31. The holograms from which these photographs were taken are identified by number in the figures.

Stereo Photography Method

Stereo photography is an accepted method for presenting three-dimensional data photographically. Stereo-photographs are made by combining photographs of two views of the same scene made from two different angular positions. The angular separation is usually 7 deg (based on the eye pupil separation and the distance of accommodation for most people). The stereo pair is mounted and then viewed with a binocular viewer to fuse the two images. Ancient stereoscope viewers are one example.

The stereo photographs shown were made by rotating the copy camera about a focal point through an angle of approximately 7 deg. The two photographs were then mounted on a board, which can be placed in a stereoscope or seen with a viewer. Viewing these images gives an appreciation of the three-dimensional character of the scene. The value of a pair of stereo pictures lies between a single picture and a montage of pictures which cannot be stereo-optically fused. Stereo pictures are not as good as holograms because both parallax and depth of focus are lost. A typical example of a hologram stereo-optically photographed is shown in fig. 32. This was taken from a reconstructed rapid double-exposure hologram (hologram 167) recorded at 110 percent design speed.

Flow direction → Direction of rotation ↓

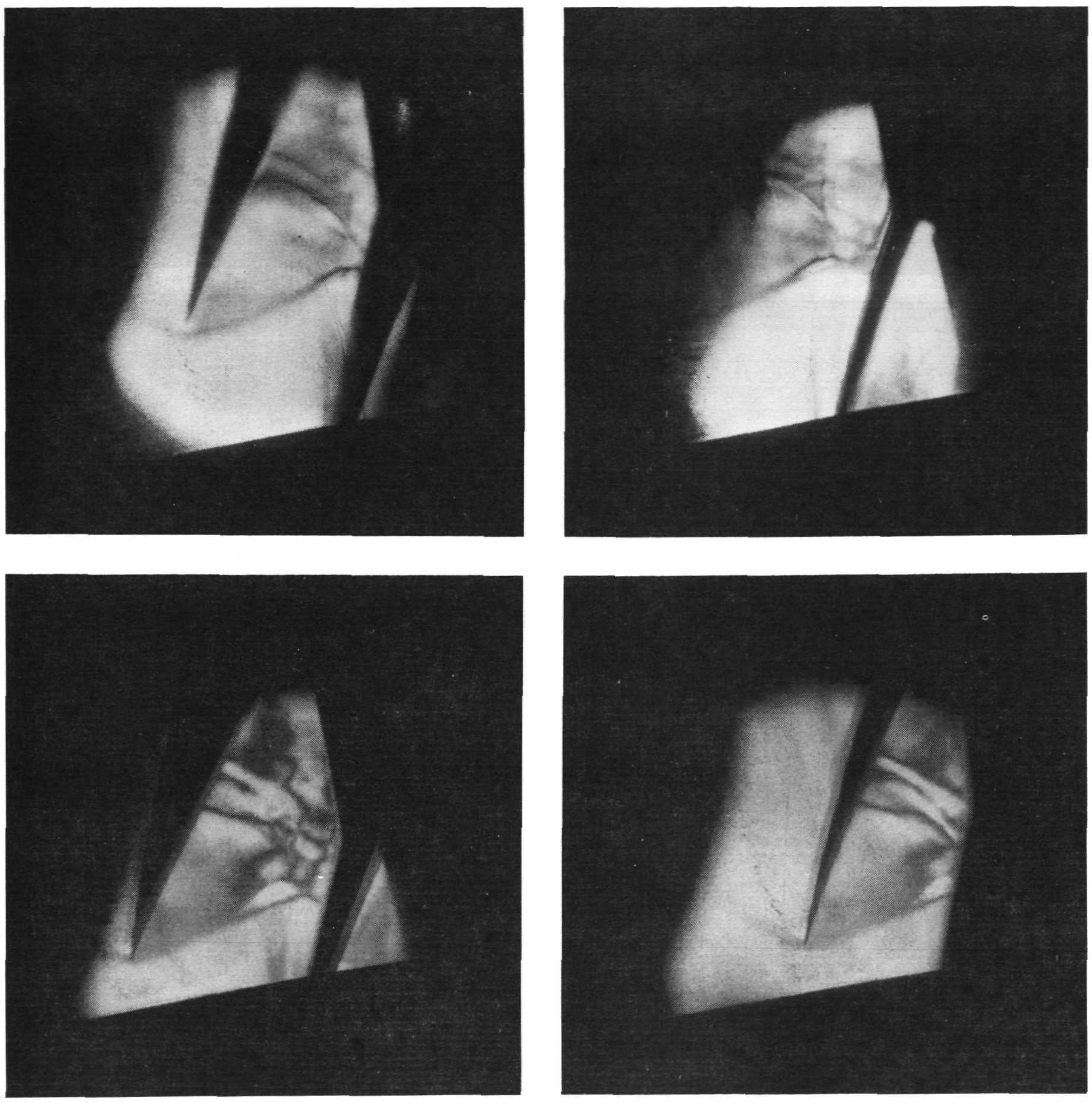

F-18521

Figure 26.--Photographs of Reconstructed Rapid Double-Exposure Hologram 311 at 90 percent Design Speed - 5 μsec Pulse Separation.

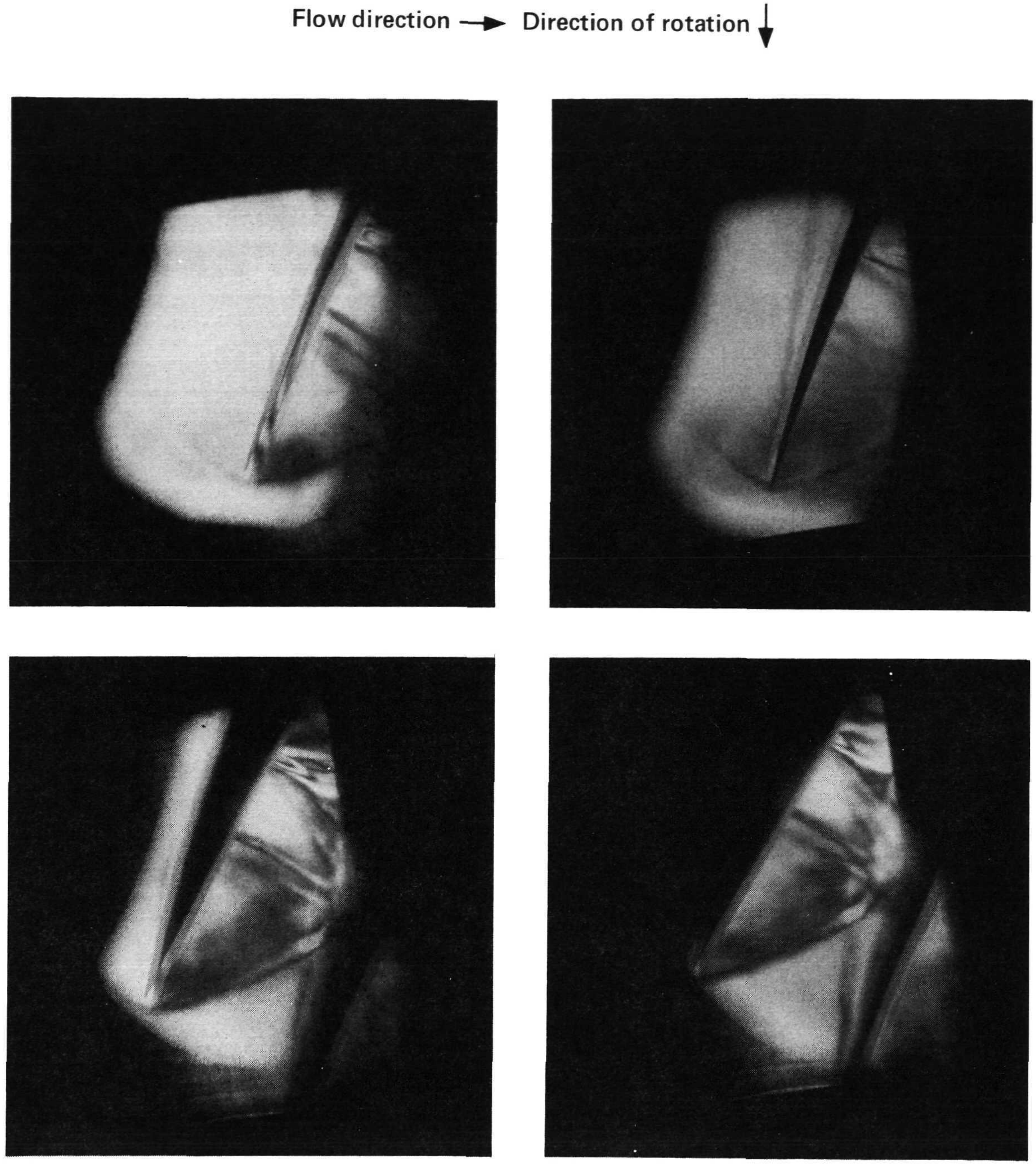

F-18513

Figure 27.--Photographs of Reconstructed Rapid Double-Exposure Hologram 324 at 95 percent Design Speed - 5 μsec Pulse Separation.

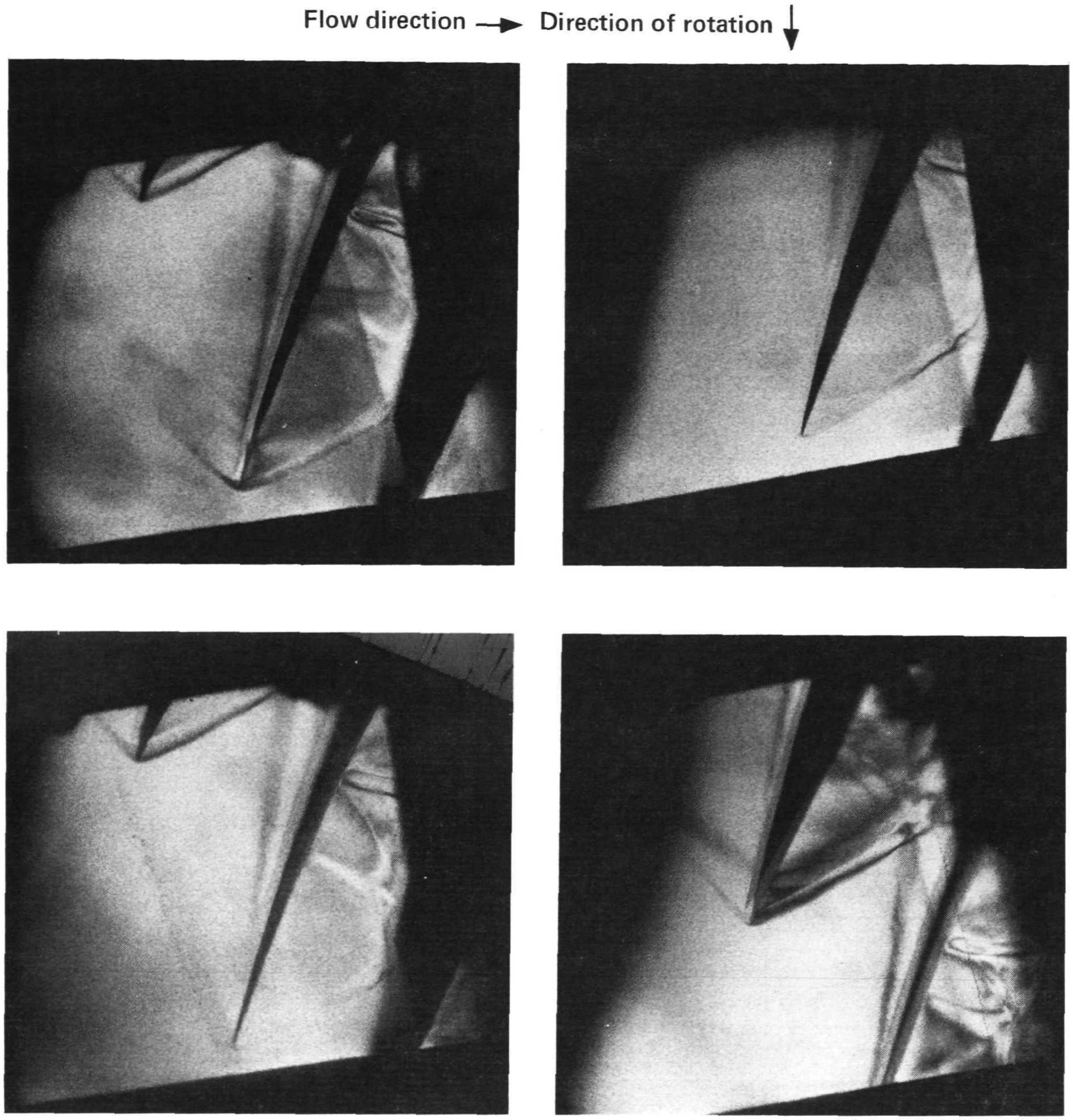

F-18522

Figure 28.--Photographs of Reconstructed Rapid Double-Exposure Holograms 339 and 343 at 100 percent Design Speed - 5 μsec Pulse Separation.

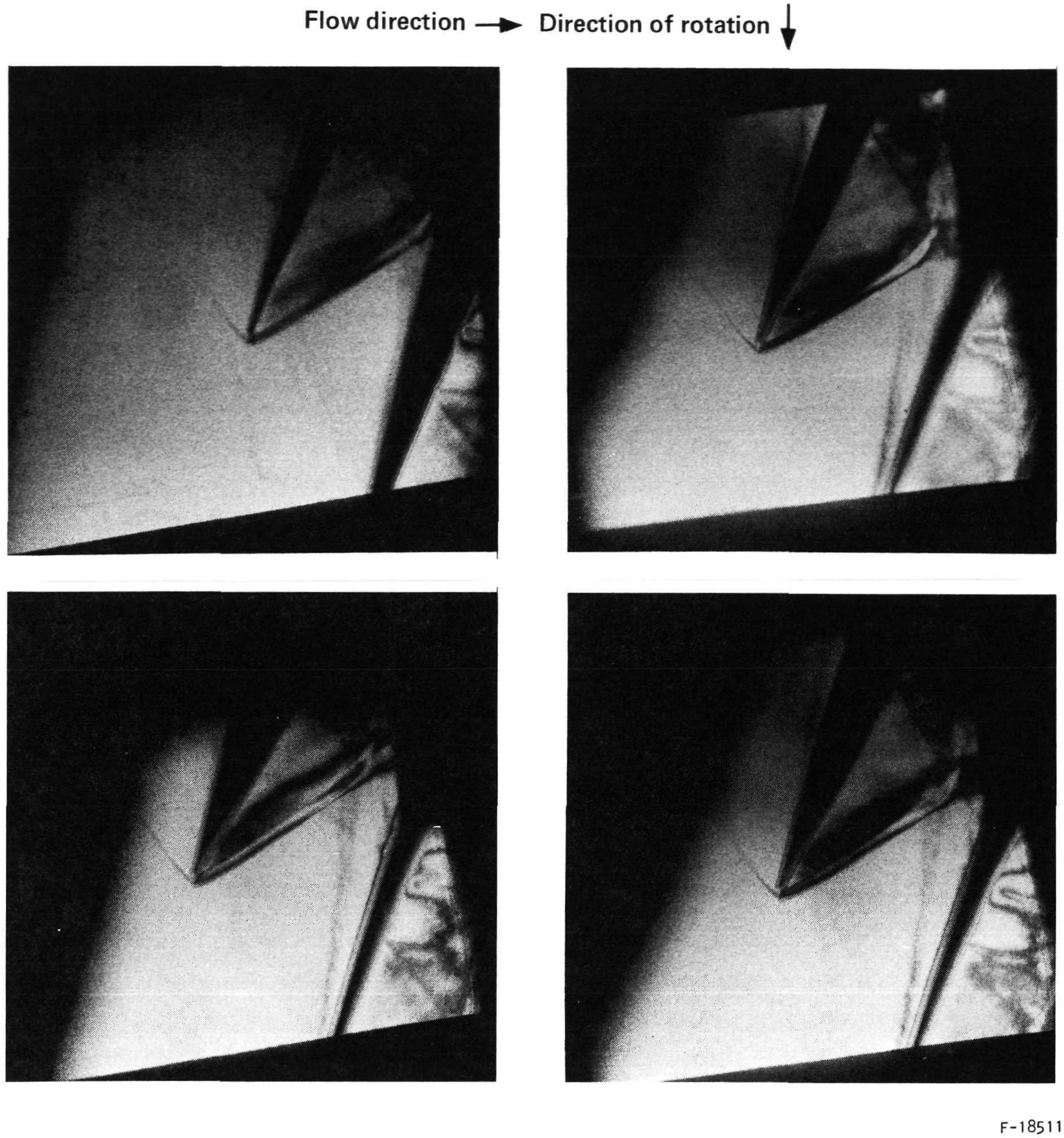

Figure 29.--Photographs of Reconstructed Rapid Double-Exposure Hologram 167 at 110 percent Design Speed - 5 μsec Pulse Separation.

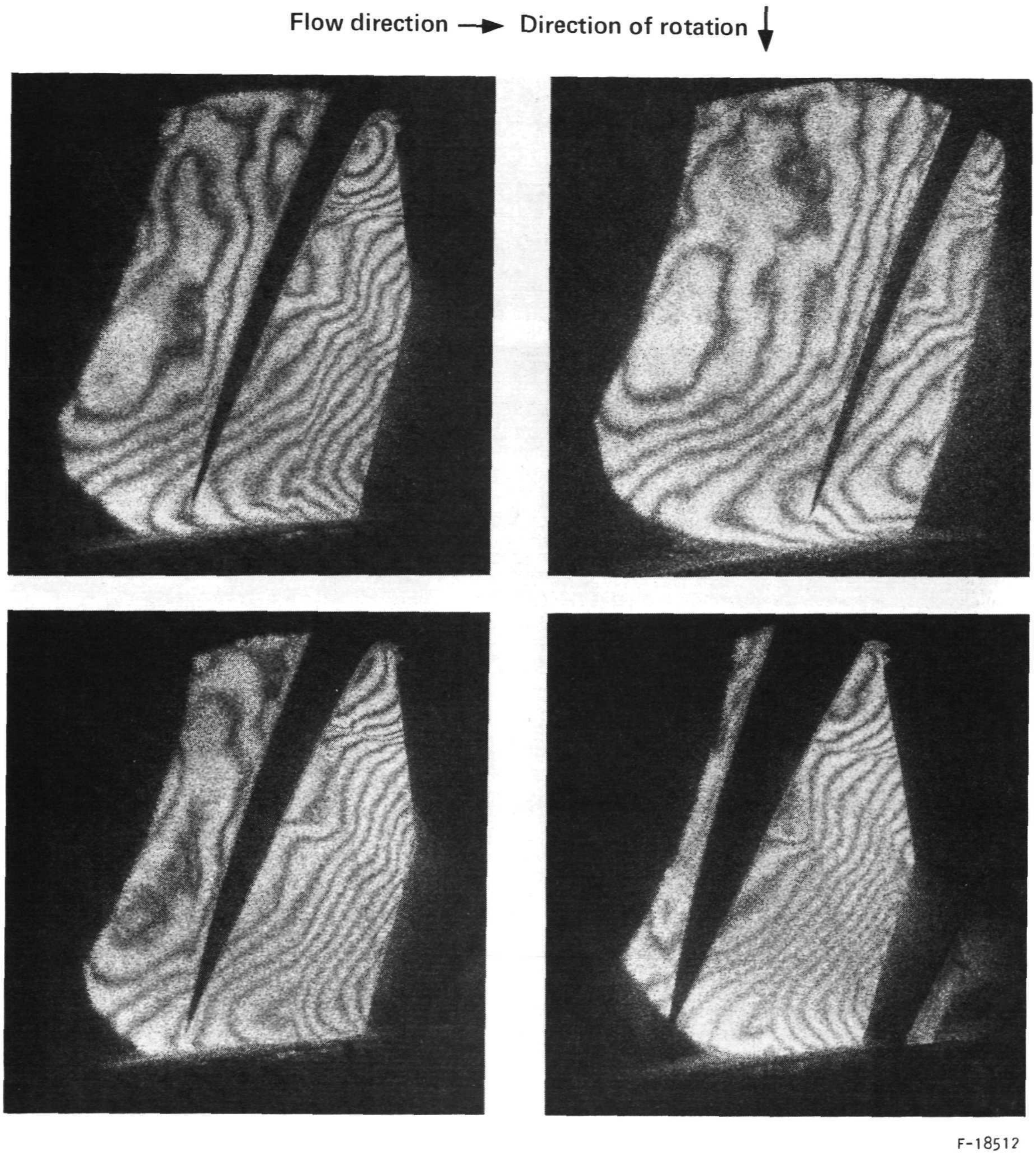

Figure 30.--Photographs of Reconstructed Double-Exposure Hologram 469 at 60 and 100 percent Design Speed.

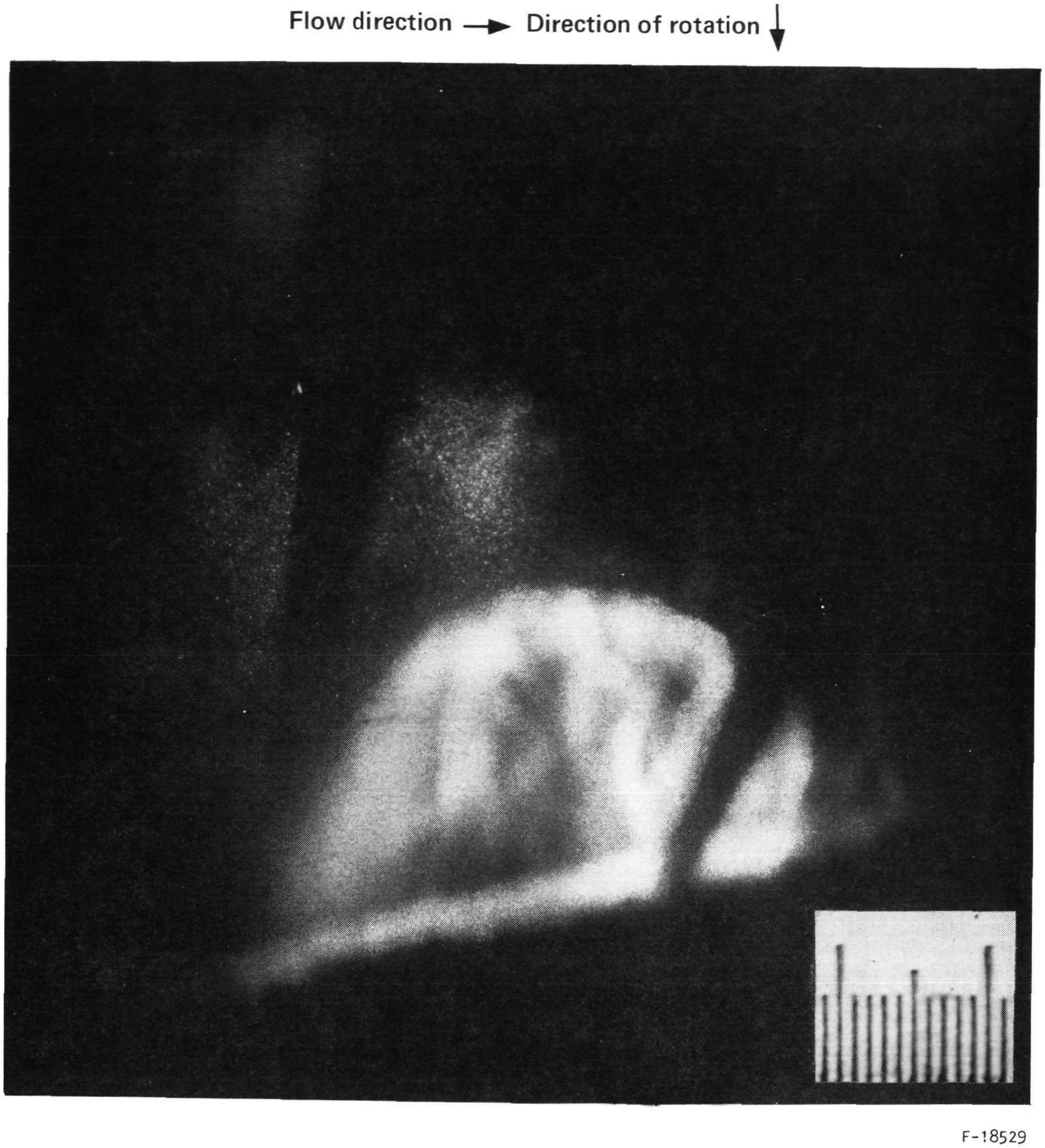

Figure 31.--Reconstruction of Double-Exposure, Scattered-Light Hologram 530 at 1000 rpm (104.7 rad/sec) - 40-μsec Pulse Separation.

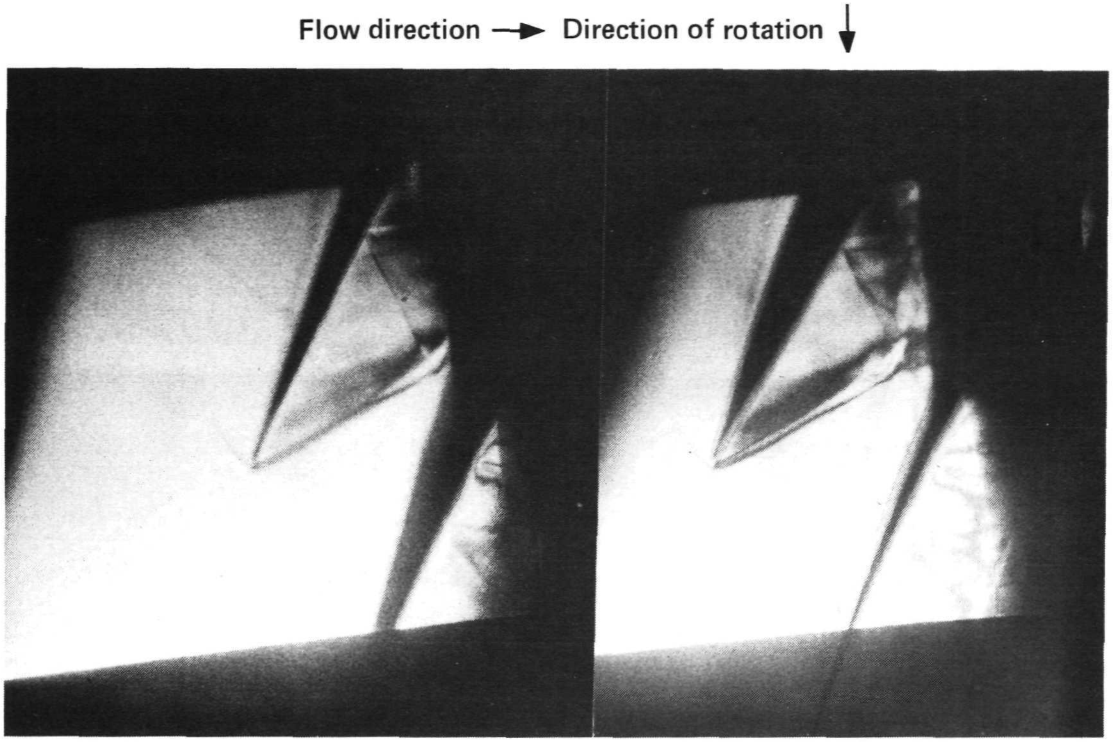

F-18505

Figure 32.--Reconstruction of Rapid Double-Exposure Hologram 167 Arranged as Stereo Pair for 110 percent Design Speed - 5 μsec Pulse Separation.

Interpretive Models of Reconstructed Holograms

Unless a viewer is perceiving a common object, a holographic image can be as perplexing as an X-ray of the human body. The granular appearance of the three-dimensional image, the difficulty of some viewers to see in the red portion of the spectrum, and the complex viewing angle all add to the confusion.

To better understand and present the data seen in the holograms, a unique method was developed for interpreting and transferring the shock patterns observed in the reconstructed holograms to an actual blade model. The method consists of superimposing the three-dimensional shadow image of the blades seen in the hologram reconstruction on a set of actual blades. This, in essence, creates a three-dimensional superimposition; once the blade images are superimposed on the blade set, the shock patterns are located in space by parallax. The shock lines are then transferred to the blade set by stretching a filament of glue between the point of intersection of the visualized waves and the surface of the actual blades. The glue filaments are then replaced by wire. The technique used to transfer the shock waves to an actual blade is illustrated in fig. 33.

As shown in the figure, the blades were mounted in a fixture to permit the actual blades to rotate about an axis coincident with the axis of rotation of the holographic blade image, using a universal vise attached to a tripod. The tripod and vise were then adjusted until the blades could be rotated about their axis of rotation in agreement with the oulines seen in the hologram reconstruction.

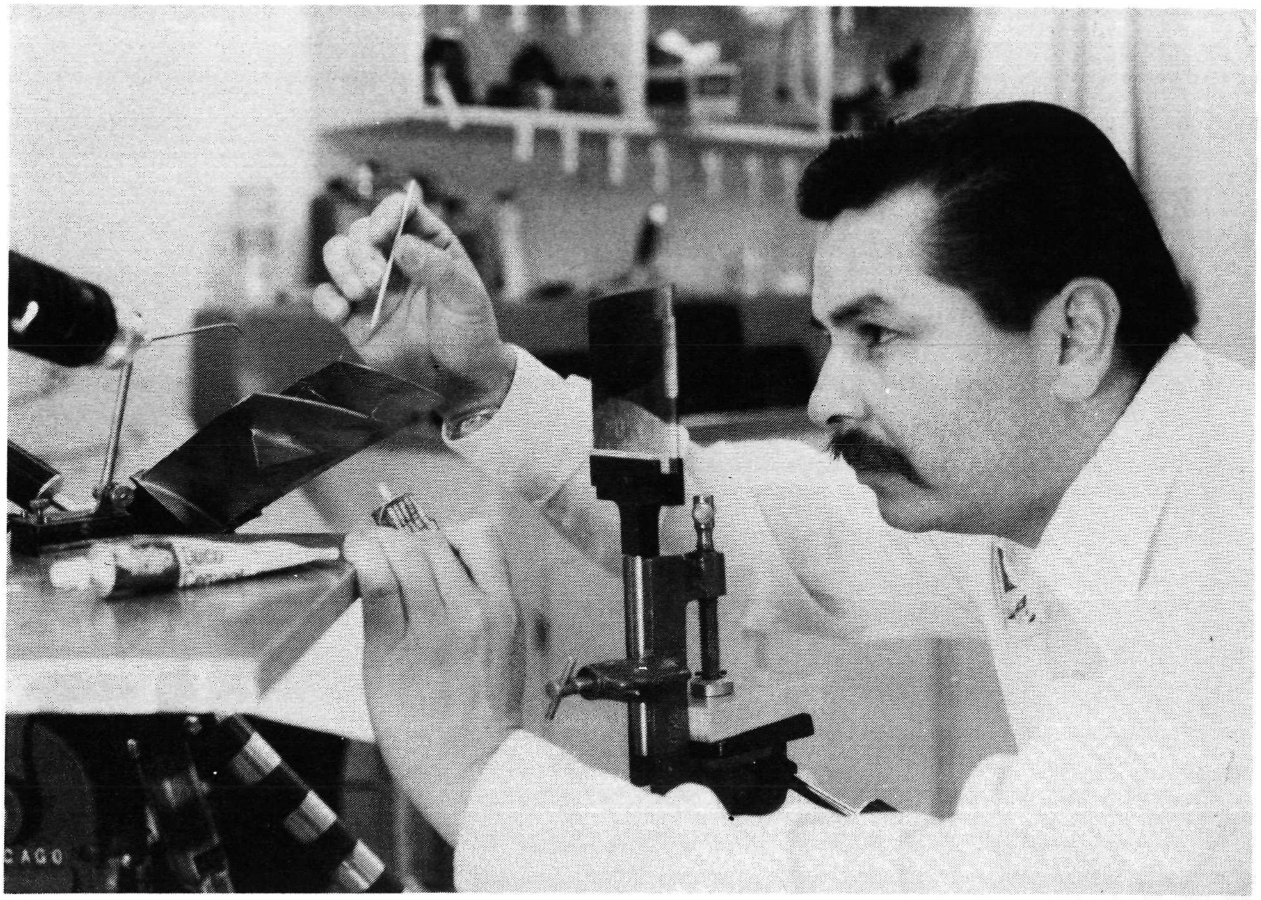

F-18508

Figure 33.--Transferring Three-Dimensional Shock Waves Seen in Hologram Reconstruction to a Set of Blades.

With this mounting arrangement, the pair of added blades could be moved from one reconstructed passage to another. This flexibility greatly improved the interpretation of the shock phenomena seen in the hologram reconstructions. For example, the phenomena at one passage (and one specific viewing direction) could be compared with phenomena in the adjacent blade passages at a different viewing angle. The lines or surfaces located in one blade passage could thus be correlated with lines in the neighboring blade passage, even though they appeared to be different in the two passages. The blade fixture also permitted comparison of holograms recorded under the same aerodynamic conditions, but at different blade positions.

Fig. 34 shows two views of the blade mounting fixture and setup. Also seen in the two views is a hologram. One view shows the reconstructing laser in the background; the other is a rear view of the blade positioner.

The blade positioning apparatus also provided an excellent means for presenting the information seen in the hologram. A series of photographs of both the reconstructed hologram and the blade set was recorded with a camera. The two images were overlaid on each other. Each photograph in the series differed from the others by the viewing angle. Neighboring pairs of pictures formed stereo pairs that could be viewed stereo-optically with the aid of a viewer.

An example of such a photograph is shown in fig. 35 (hologram 339). This was taken from a reconstructed rapid double-exposure hologram recorded at design speed and design pressure ratio. The figure contains three sets of photographs taken at different viewing angles. Neighboring photographs correspond to a change in viewing angle of 6-1/2 deg. The upper row of each figure shows the photograph of the hologram reconstruction superimposed on the photograph of the added pair of blades. The lower row in each figure presents only the hologram reconstruction; these are included because the superimposed pictures mask some of the fine detail of the fringes. Neighboring pairs of pictures are mounted stereo-optically.

In the hologram reconstructions, the blade surfaces are only defined by their shadow images. This, coupled with the limited angular field of view, makes it difficult to determine the spatial location of the fringes when viewing the stereo pair of the hologram with a stereoviewer. The added blades, however, were not restricted in angle, and the pictures of these blades show surface detail. As a result, when viewed stereo-optically, the blades appear to be quite three-dimensional. Consequently, the viewer can begin to visualize the three-dimensional character of the interference fringes. The stereo-pictures, however, have no focusing depth as in the case of the hologram. To achieve a moderately large depth-of-focus, the pictures were taken at a large f-number (usually f/11 or f/16).

Actual models of shock patterns visualized from the reconstructed holograms were constructed with glue filaments and wires. The individual holograms and blade passages were correlated with a series of holograms taken at the same operating conditions with the aid of the blade positioning apparatus. Fig. 36 presents an example of interblade passage shocks developed using wires to define the shock fronts. This model was developed from holograms 164, 290, 292, 293,

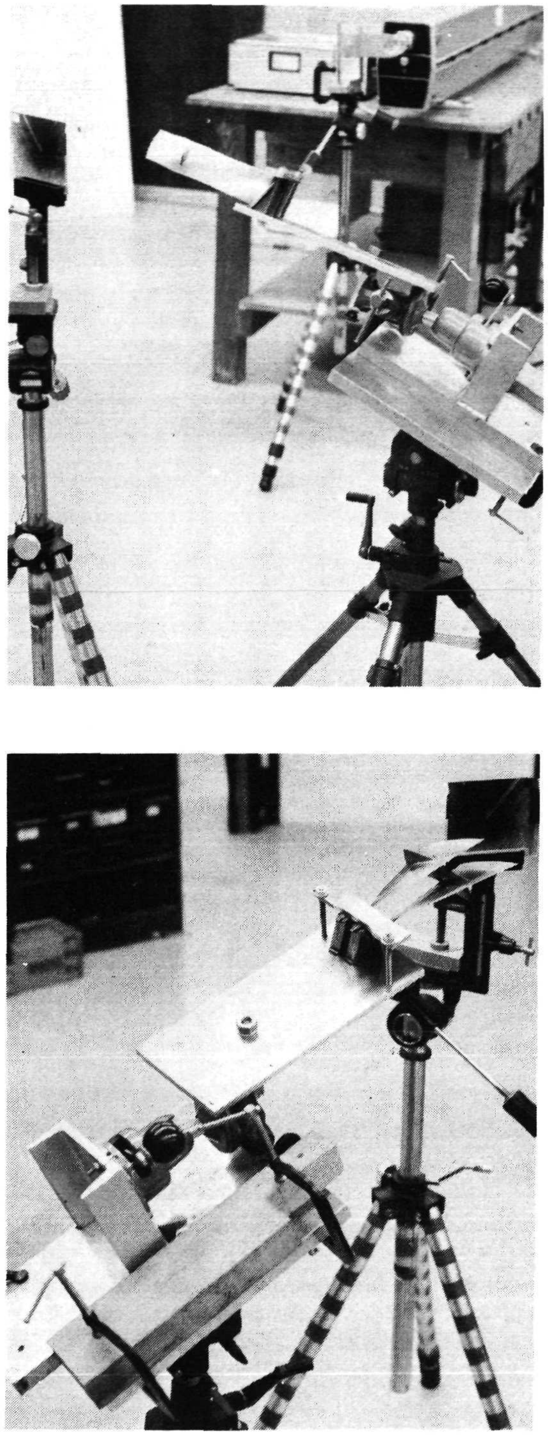

F-18509

Figure 34.--Setup for Reconstructing Holograms and Comparing the Holographic Images with a Pair of Actual Blades.

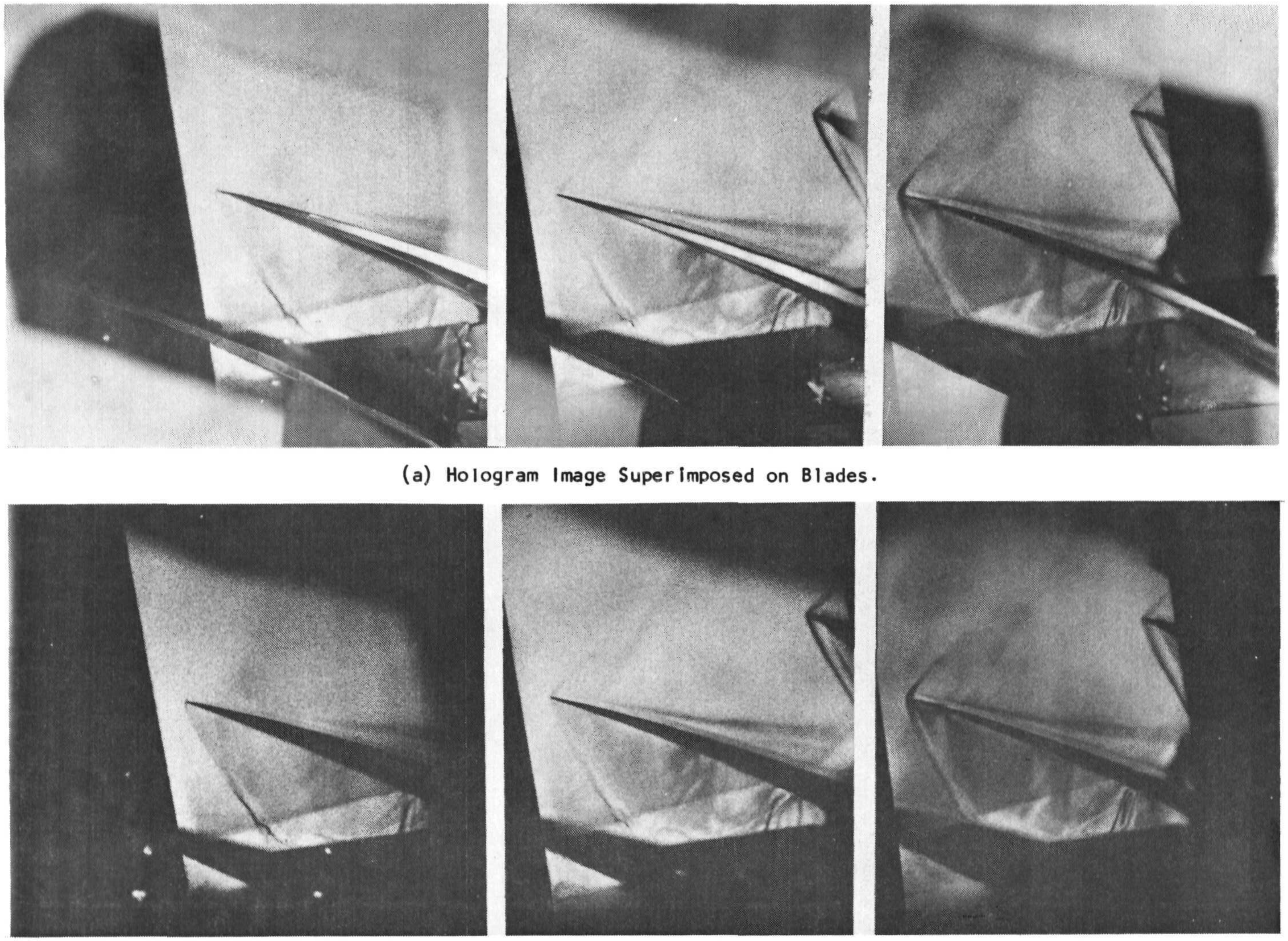

(a) Hologram Image Superimposed on Blades.

(b) Reconstructed Hologram.

F-18535

Figure 35.--Three Views of Reconstructed Hologram 339 Superimposed on Fan Rotor Blades and Corresponding Views of the Hologram Alone.

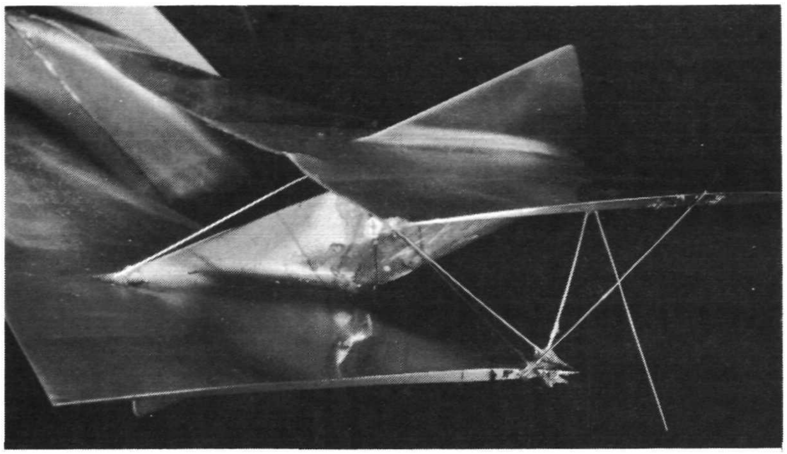

(a) Photograph of Model.

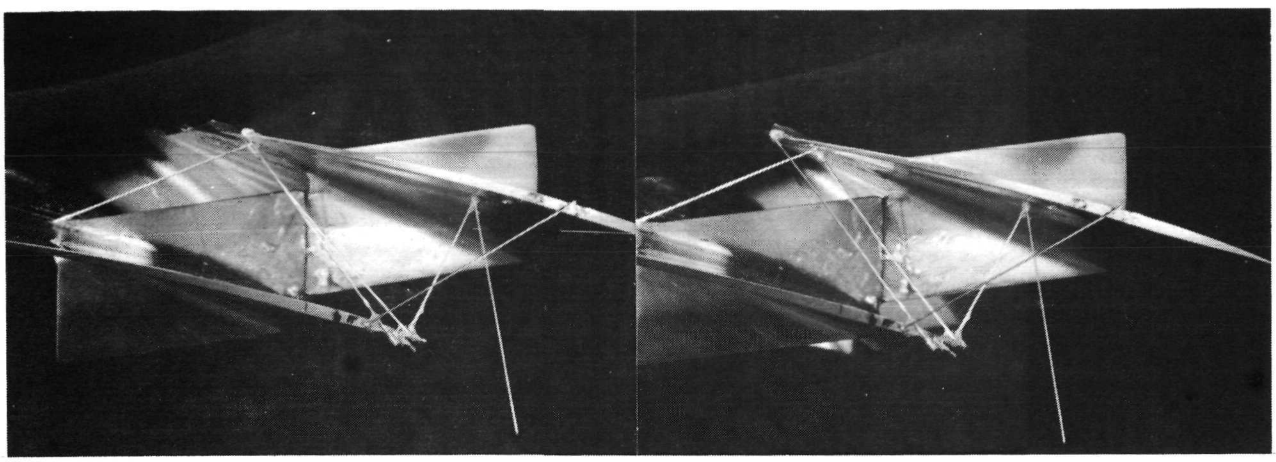

(b) Stereo Photograph of Model.

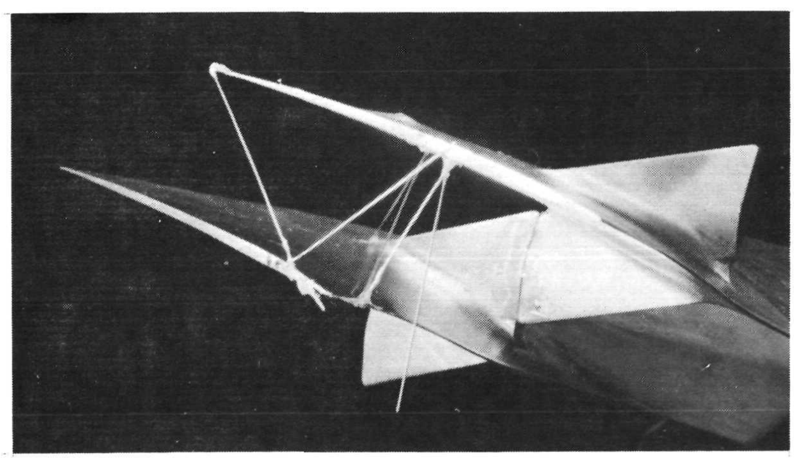

F-18530

(c) Model as Seen Through Hologram.

Figure 36.--Model of Interblade Passage Shock System using Wires to Represent Shock Fronts.

335, 337, and 338, which were recorded at design speed. The lower figure in the set shows the view of the blades as seen from the hologram. The center figures are mounted as stereo pairs that can be viewed three-dimensionally with the aid of a viewer. After the shock planes were defined by the network of wires, a model was constructed using transparent plastic sheets to define the various shock planes as shown in fig. 37.

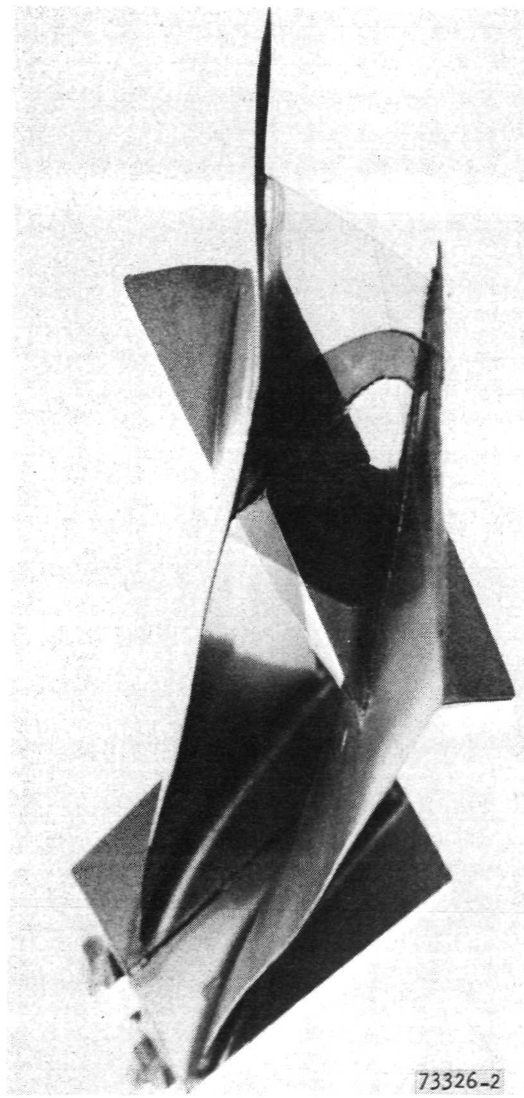

Figure 37.--Model of Interblade Passage Shock System Using Transparent Plastic Sheets to Define Various Shock Fronts.

AERODYNAMIC ANALYSIS AND INTERPRETATION OF HOLOGRAMS

This section presents the results of the successful holograms recorded during the test and the aerodynamic interpretation of the information obtained from the reconstructed holograms. Of the four basic types of holograms recorded, i.e., long-pulse, single-exposure; rapid double-exposure; long double-exposure; and scattered-light holograms, the rapid double-exposure holograms provided the best recordings insofar as location and identification of shock fringes. Although these recordings were mainly qualitative in nature, some quantitative information such as shock angle and relative shock strength could be determined from the holograms. Because of the angular view and limited viewing image, however, details upstream of the rotor and in the trailing edge section of the rotor passage were limited. Some quantitative information with respect to density and velocity distribution were also obtained from the double-exposure and scattered-light holograms.

The holography tests, as indicated earlier, were conducted in concert with the aerodynamic performance testing of the transonic fan stage (refs. 5 and 6). Combining the two test programs enabled testing to be accomplished with a minimum of setup and installation changes. The first phase of the holography tests was initiated after completion of the shakedown and performance testing and prior to distortion testing of the transonic fan. The test conditions (corrected speed and flow) were duplicated and the aerodynamic data obtained for both tests were identical. The same aerodynamic performance data (overall, blade element, and high response pressure data at the rotor tip) were therefore used for the aerodynamic analysis and interpretation of the reconstructed holograms.

Rapid Double-Exposure Holograms

Most of the more than 600 holograms recorded during the test were recorded using the rapid double-exposure technique. As stated earlier, this technique produced by far the most consistent and clearly definable recordings because of its relative insensitivity to interference effects (i.e., window distortion, rig vibration, oil deposits, etc.). These holograms also showed remarkable consistency of the interblade shock patterns observed for holograms taken at the same operating conditions.

Typical examples of the rapid double-exposure holograms recorded at 90, 95 100, and 110 percent design speed are presented in figs. 38 through 41. These holograms were recorded with a pulse separation time of 2 to 5 μsec. The blade movement during this time interval was approximately 5 percent of blade passage. Fig. 38 presents composite stereo photographs of a reconstructed rapid double-exposure hologram (352). In the upper figure (a), a stereo photograph, the hologram image is superimposed on the actual blade set. By this method of super-positioning, a three dimensionality is provided in the reconstructed image to help identify the location of the shock patterns. The neighboring photographs are stereo pairs that can be sterographically seen with a viewer. The lower figure (b) shows a stereo photograph of a hologram reconstruction. Each neighboring photograph corresponds to a change in viewing angle of 6-1/2 deg. This

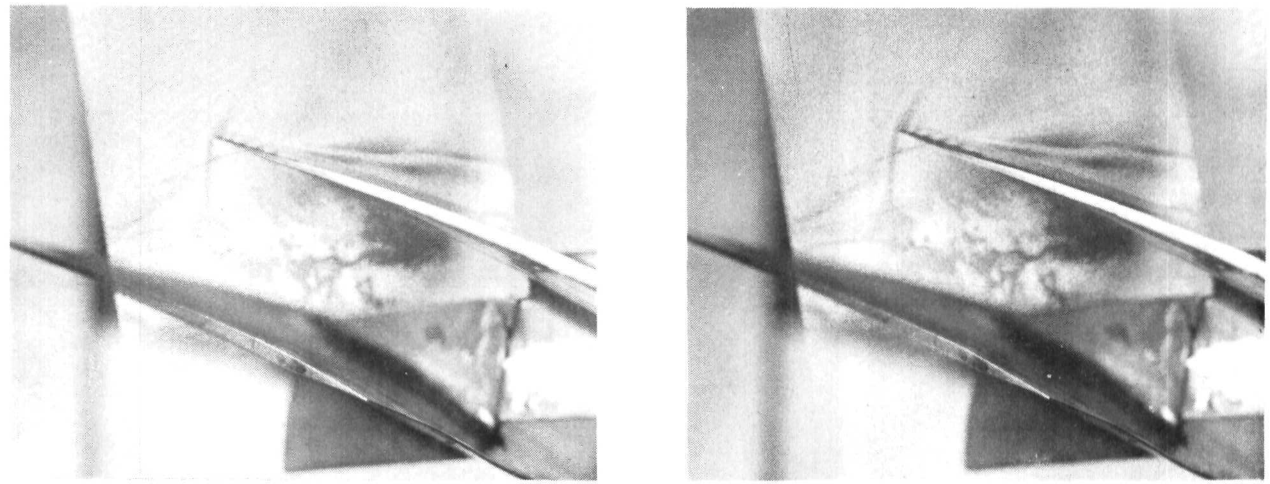

(a) Hologram Image Superimposed on Blades.

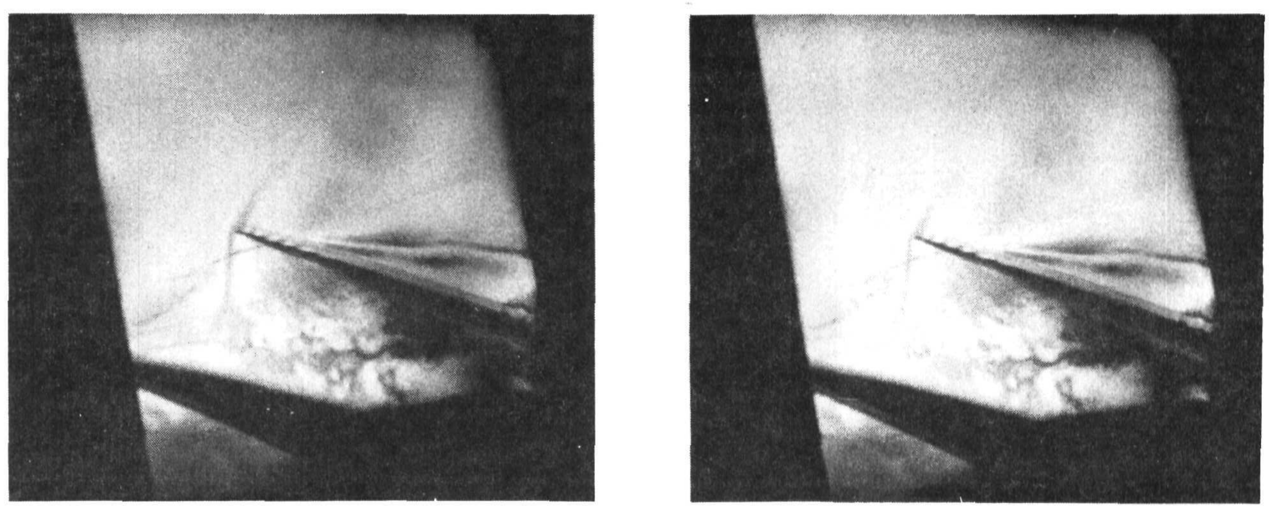

(b) Reconstructed Hologram.

F-18531

Figure 38.--Stereo Photographs of Reconstructed Double-Exposure Hologram 352 at 90 percent Design Speed - 5 μsec Pulse Separation.

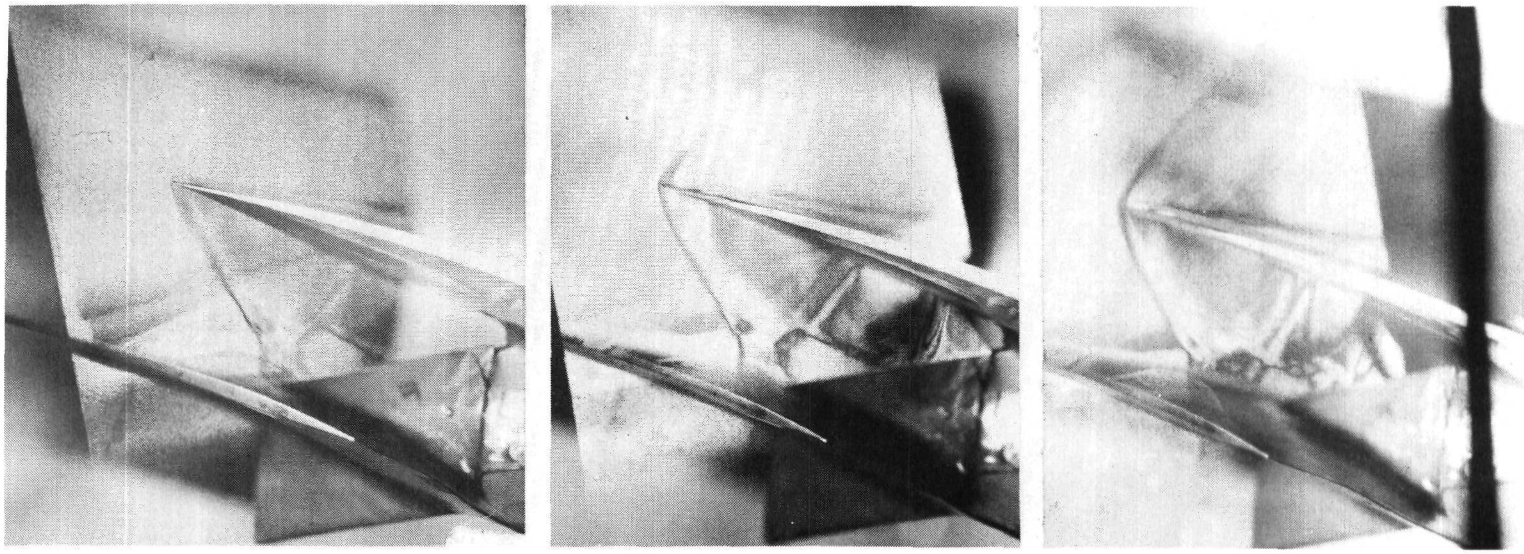

(a) Hologram Image Superimposed on Blades.

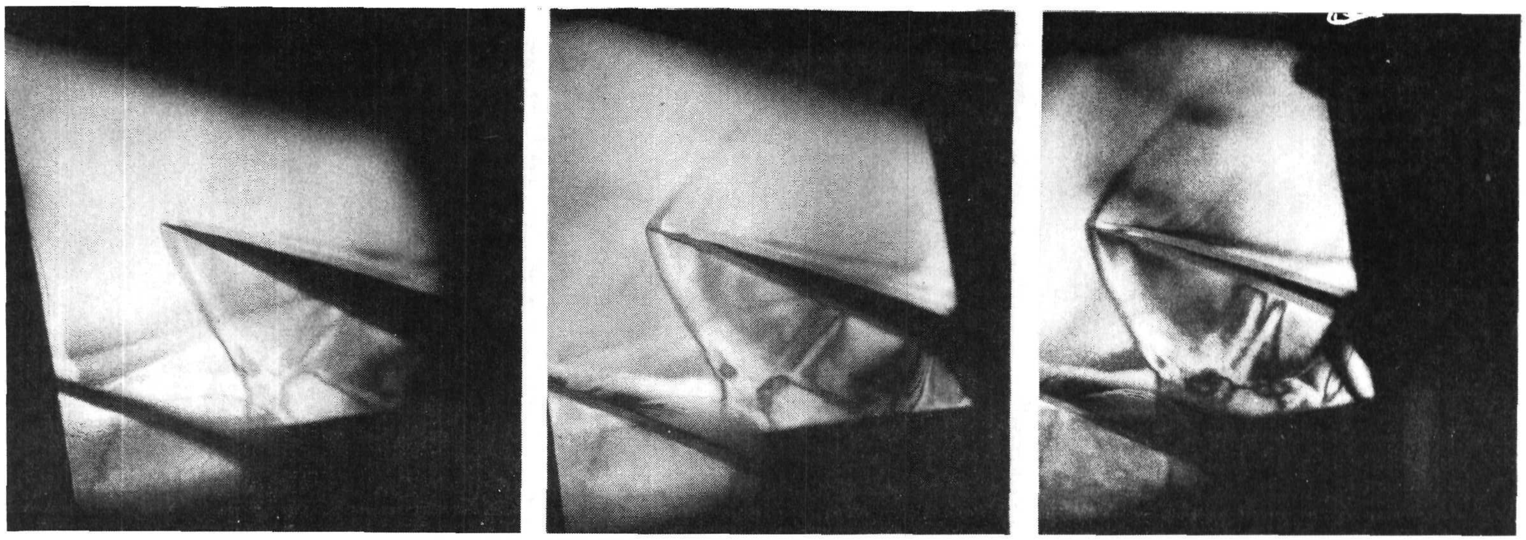

(b) Reconstructed Hologram.

F-18532

Figure 39.--Stereo Photographs of Reconstructed Double-Exposure Hologram 332 at 95 percent Design Speed - 5 μsec Pulse Separation.

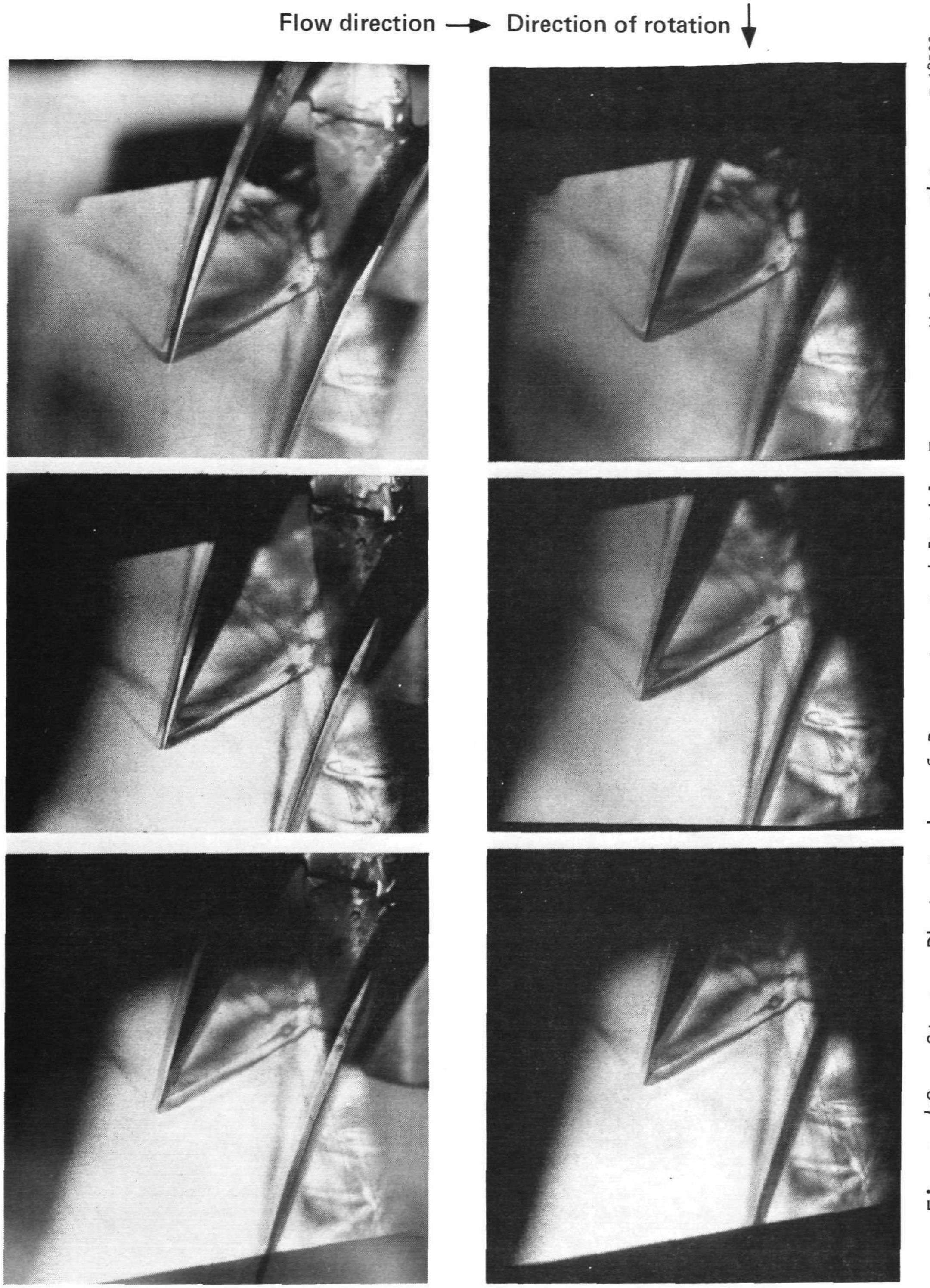

Figure 40.--Stereo Photographs of Reconstructed Double-Exposure Hologram 343 at Design Speed and Design Pressure Ratio - 5 μsec Pulse Separation.

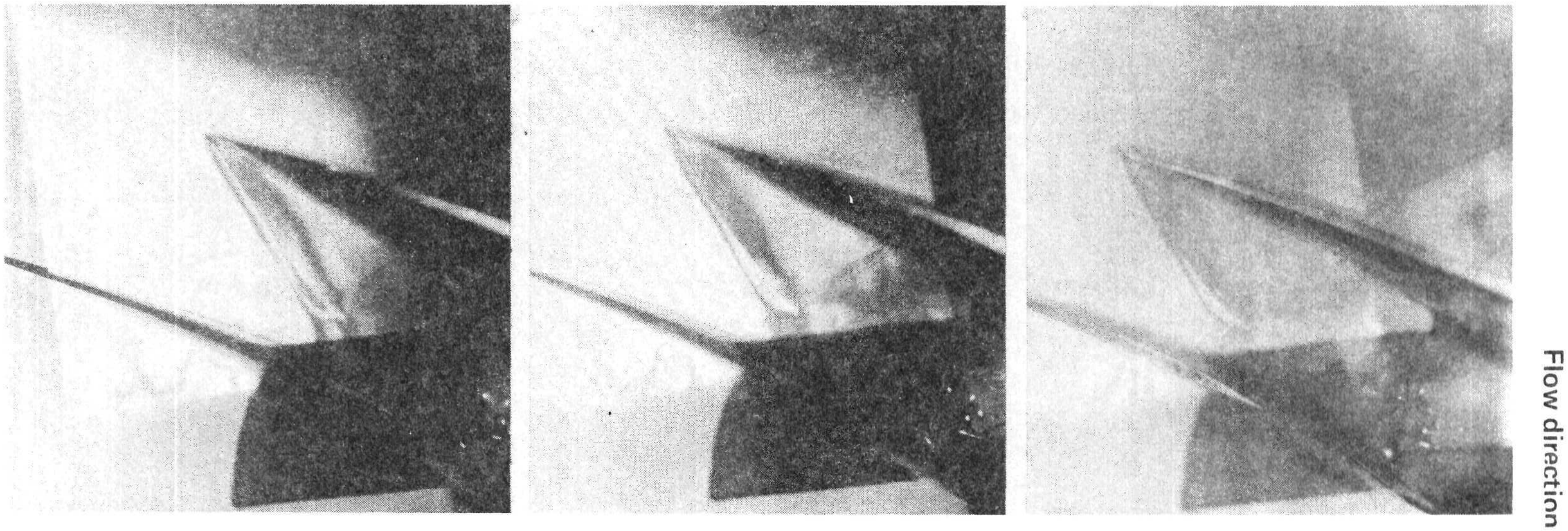

(a) Hologram Image Superimposed on Blades.

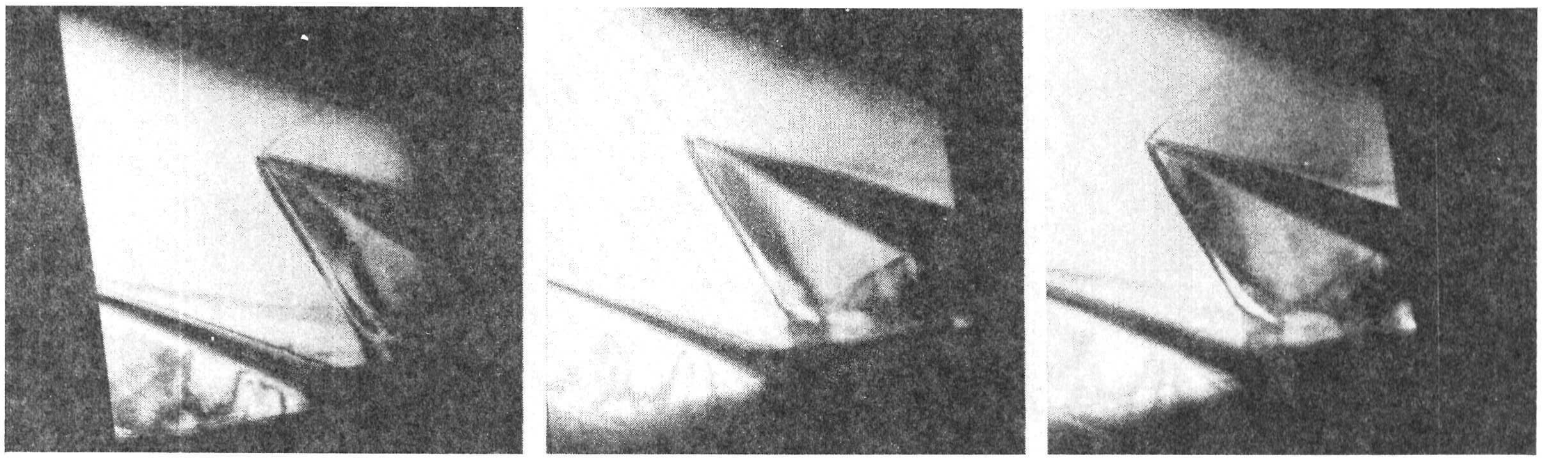

(b) Reconstructed Hologram.

F-19088

Figure 41.--Stereo Photographs of Reconstructed Double-Exposure Hologram 167 at 110 percent Design Speed - 5 μsec Pulse Separation.

hologram was taken at 90 percent design speed. For this condition, the rotor is operating with a strong normal shock at the blade leading edge. As the stage pressure ratio was increased, however, a strong detached bow shock was evident at the blade leading edge. Similar stereo photographs of hologram 332 taken at 95 percent design speed are presented in fig. 39. The image area shown is focused mainly about the leading-edge section of the blade passage because this is the region of greatest interest. It can be seen that at this condition the rotor is started and the leading-edge shock is nearly oblique and swept slightly into the passage. Details of the trailing-edge area are obscured by the midspan dampers in this figure. Fig. 40 presents a similar reconstruction of hologram 343 taken at design speed and design pressure ratio. For this design speed and pressure ratio condition, the leading-edge shock is slightly more oblique and curves to become almost perpendicular to the blade suction surface. Bright fringes nearly normal to the blade passage also are evident in the adjacent passage. Fig. 41 presents photographs of hologram 167 recorded at 110 percent design speed. The shock fringes at this condition appear to be fewer and more clearly defined.

Long Double-Exposure Holograms

Holograms 456 and 472 were selected as the most representative of long double-exposure type recordings. These recordings were taken with the 1/4-in.-thick (0.64 cm) viewing window. These holograms were photographically recorded using the real image projection technique in which the holograms were illuminated by a converging pencil of light from a helium-neon gas laser (Spectra Physics Model 125). The portion passing through the hologram was slightly more than 1 mm in diameter. When illuminated in this manner, the holograms project a pinhole-camera type of image, which has large depth-of-focus. This method of projection was important because the fringes in these holograms were at different focal depths. Illumination of the hologram at different points gave interferograms as viewed from the illuminated point. Fig. 42 (hologram 456) shows a typical example of an interferogram obtained from a single double-exposure hologram. The initial exposure was recorded at 60 percent design speed, and the second at 100 percent design speed. Inspection of the individual photographs shows inflection in the fringes due to a shock on the suction surface of the blade as well as a larger perturbation due to a shock on the pressure side of the blade. The general interference pattern, however, passes through the blade almost continuously. The lack of change from the suction to the pressure side strongly suggests that path changes are due more to window translation or warpage than to purely aerodynamic effects.

Figure 43 presents a similar series of interferograms taken from hologram 472. Again, initial exposure was recorded at 60 percent design speed followed by the final exposure at 95 percent design speed. The example includes more views of the same hologram taken by scanning the reconstructing beam over the hologram. The two top photographs were taken with wide-aperture projections (2- to 3-mm spot size). This destroyed the pinhole camera effect and caused the fringes to focus in space. Fringes beyond the film plane in the copy camera were out of focus. Reducing the size of the reconstructing beam ($\sim$1 mm) brings all the fringes into focus, as seen in the other four photographs.

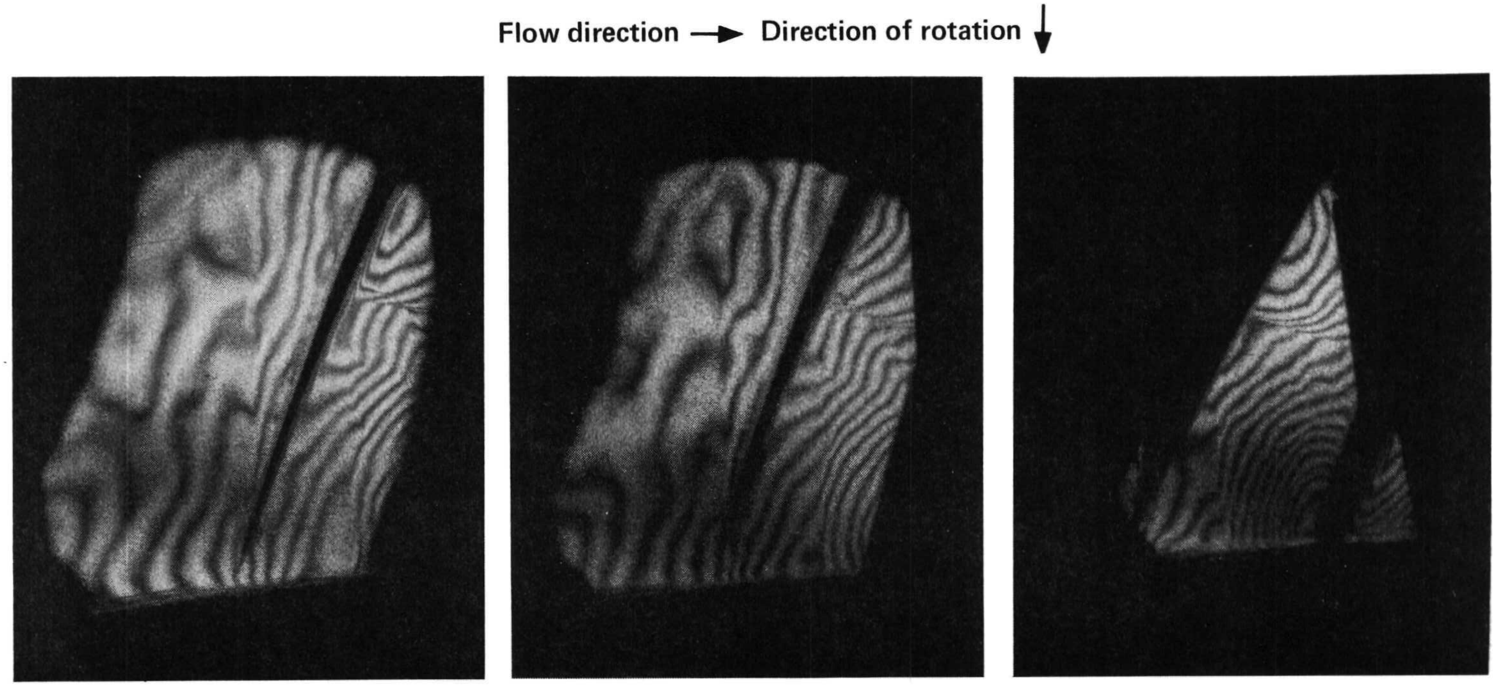

Figure 42.--Reconstruction of Double-Exposure Hologram 456 at 60 and 95 percent Design Speed.

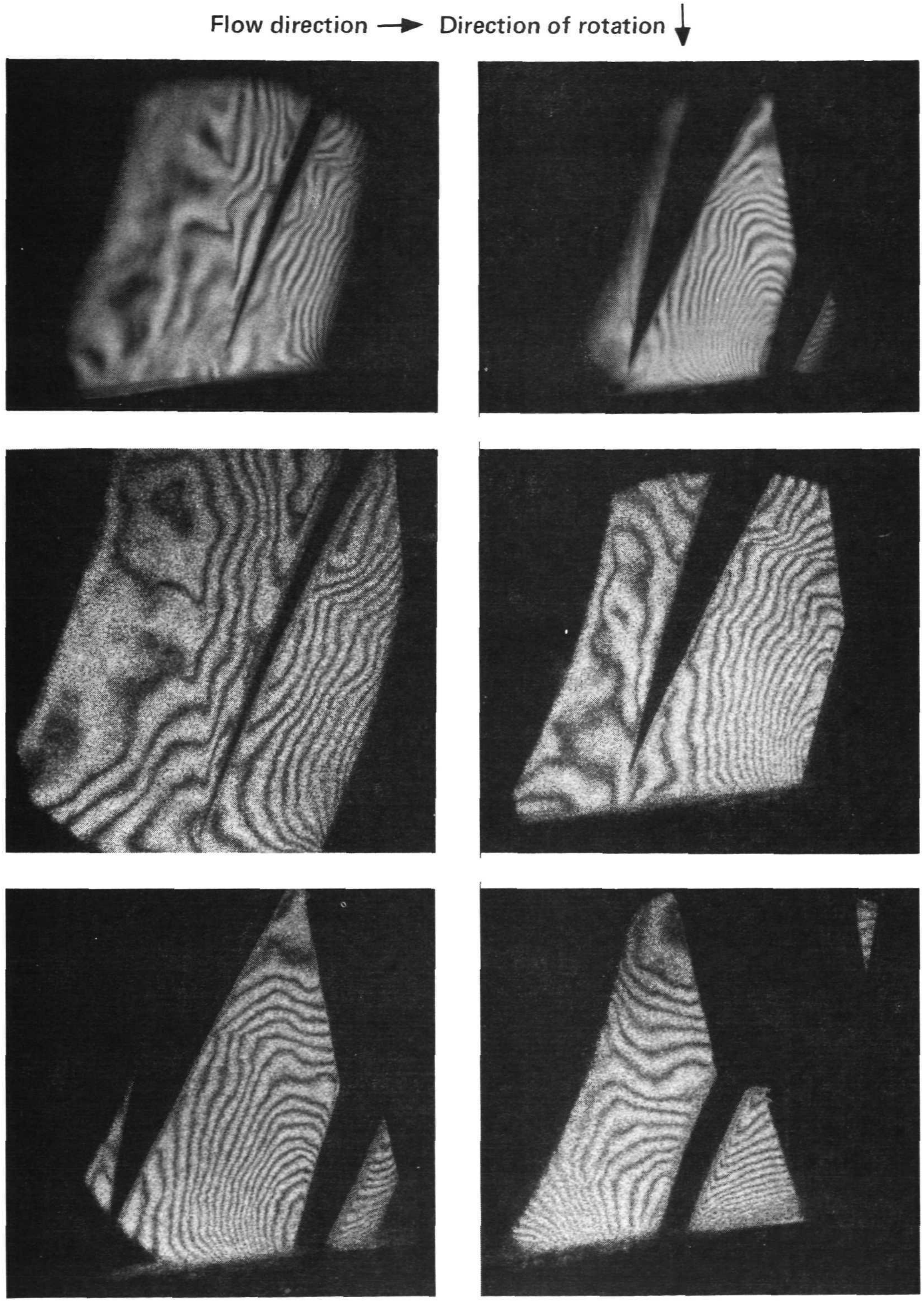

F-18539

Figure 43.--Reconstruction of Double-Exposure Hologram 472 using Wide Aperture and Narrow Aperture Projection at 60 and 95 percent Design Speed.

The long double-exposure holograms were confusing because the aerodynamic effects could not be completely isolated from the extraneous fringes. The principle effort was spent in attempting to isolate these fringes and determine their effect on the overall interference pattern.

Scattered-Light Holograms

Of the nearly 50 scattered-light holograms that were attempted at a speed of 1000 rpm (104.7 rad/sec), one in particular (hologram 512) was found that demonstrated the feasibility of velocity measurements using a rapid double-exposure scattered-light hologram. A photograph of a magnified portion of this hologram is shown in fig. 44. Inspection of this picture shows an array of pairs of bright dots. Each pair corresponds to a particle (a microballoon of ~30-micron size) photographed at two different times. The two laser pulses in this instance were separated by 60 μsec. An enlarged scale appears at each side of the picture. Each division of the scale is 1 mm. Measuring each particle separation and dividing by 60 μsec (the laser pulse separation) gives the in-plane velocity of each particle. Values of 32.7 ft/sec (10 m/sec) are typical in this case. Assuming the particle velocity and flow are identical (i.e., particle viscous force to be greater than inertial force), the local flow velocity can be obtained from such a measurement.

The background granularity pattern seen in this picture is not particulate, but instead is laser noise due to light being scattered from particles on the two windows. This example indicates that more scattering from the windows would make detection of the flow-entrained particles even more difficult. As the background scattering increases, the particles become hidden in the granularity of noise. Spatial filters can be used to reduce the noise; however, the simplest approach is to maintain clean windows to minimize such extraneous scattered light at the time of recording.

Fig. 45 shows reduced size photographs of the same hologram (512) that were made by direct image projection. The four photographs differ from one another in the location of the copying photographic film (i.e., by the focus of the hologram). The pictures show the location of predominant scattering of the direct laser beam by oil and particles adhering to the inner surface of the viewing window. The upper left figure was taken with the film plane focused at the inner surface of the viewing window. The window was at a distance of 6.7 in. (17 cm) from the hologram. This picture clearly shows the oil streaks and particles occluded on the surface. The upper right-hand picture was made with the film plane at a distance of 11.8 in. (30 cm) from the hologram. It corresponds to a focal position deep within the interblade flow field. Scattering from the window surface is completely out of focus. In this picture, a few flow-entrained particles are in sharp focus; the remaining particles are out of focus. The lower left and right figures differ from one another by only a few centimeters in the location of the recording film plane. The difference is sufficient to bring different flow-entrained particles into sharp focus. Again, the out-of-focus scattering of light from the oil and dust on the viewing window clearly dominates these two pictures. Any particles behind this region are obscured. Each flow-entrained particle is seen as a double dot, which identifies

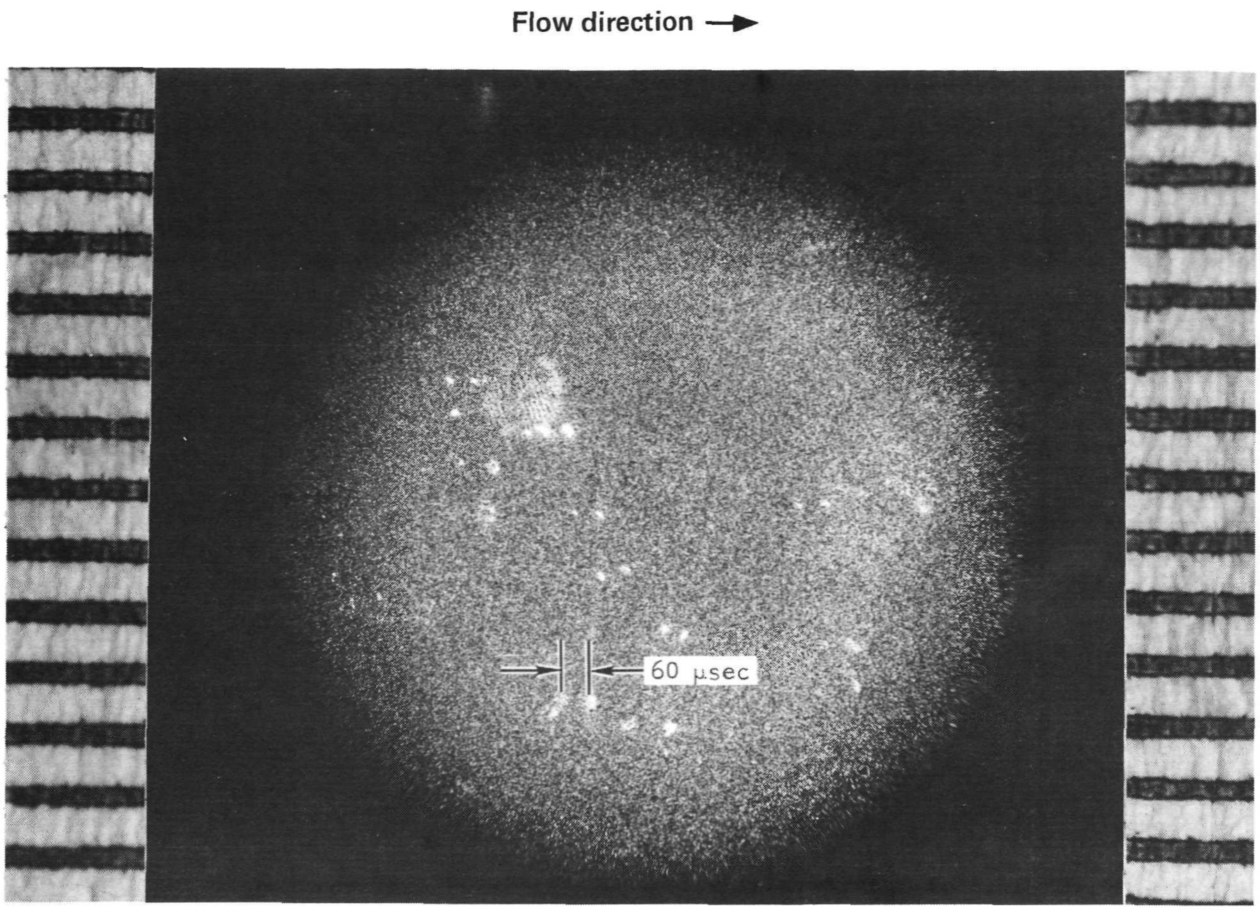

Scale is 1 mm per division (at border)

F-18540

Figure 44.--Enlarged Portion of Reconstruction of Double-Exposure, Scattered-Light Hologram 512 - 60 μsec Pulse Separation, ≃10 m/sec Flow Velocity.

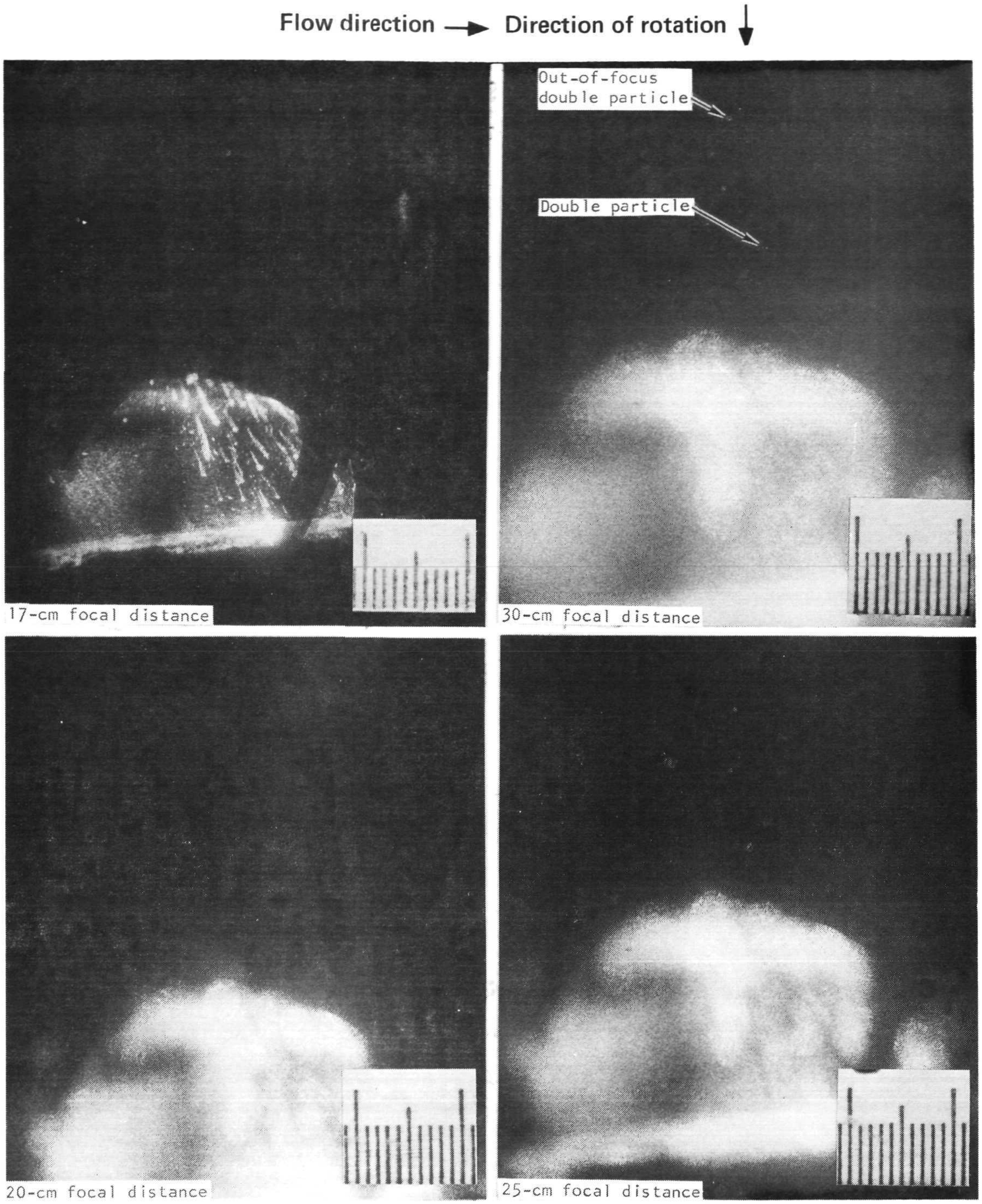

Scale is 1 mm per minor division

F-18517

Figure 45.--Real Image Projection Photographs from Double-Exposure, Scattered-Light Hologram 512 - Each View Differs in Hologram Focal Distance - Fan Rotating at 1000 rpm (104.7 rad/sec), Laser Pulses Separated by 60 μsec.

the position of a single microballon at the time of the first and second laser pulses. Fig. 44 was made by magnifying the area seen in the lower pair of pictures and sharply focusing on a pair of double images.

Ideally, such a hologram would be set up relative to a predetermined coordinate system. A measuring microscope would then be used to determine the position of each pair of dots--the X, Y, and Z coordinates of the particles at two instances of time would be found. Vector subtraction of coordinates of each particle would give the displacement. This quantity, when divided by the laser pulse separation, would give the average velocity at the average coordinates of each point. Such an analysis would obviously be time-consuming. Fig. 44 showed the flow to be heavily entrained with particles. Systematic analysis would therefore require measurement of each particle's position at two instances of time.

The significance of this new technique is that the measurement of velocity and direction at various operating conditions can be done in the laboratory with the fan stage at rest. Other methods of determining flow velocity, such as the laser doppler velocimeter, are point measurements that require continuous operation of the rig to record velocity at a wide variety of points.

Fig. 31 (hologram 530) is an example in which the two laser pulses were separated by 40 μsec. As before, the fan stage was rotating at 1000 rpm (104.7 rad/sec). The microballoon density was an order of magnitude greater than in figs. 44 and 45 (hologram 512). Even under high magnification, it is extremely difficult to separate pairs of particles.

In summary, scattered-light holograms clearly show that flow-entrained particles can be used to measure flow velocity. However, to use the technique at speeds of 12 000 to 13 000 rpm (1256 to 1360 rad/sec), the laser pulse duration must be decreased proportionally to approximately 5 nsec. This can be done by using the technique of pulse chopping (ref. 11). Such a modification was not within the scope of this program.

Aerodynamic Discussion

Aerodynamic analysis of holograms at 100 percent design speed.--The rotor blade model showing the shock system developed for the 100 percent design speed and design pressure ratio condition is presented in fig. 46. For this condition, the stage was operating with a flow approximately 4 percent higher than design. The rotor inlet relative Mach number as determined from the blade element performance was very close to the design value (1.62 at the tip); however, the exit relative Mach number was significantly lower (subsonic) in the midspan damper region. The rotor adiabatic efficiency at this condition is 86.7 percent and the overall stage efficiency is 81.0 percent. The shock models were developed from rapid, double-exposure holograms 294, 339, 340, 341, 342, and 343.

Referring to fig. 46, the shock system for the 100 percent design speed condition shows four major shock waves: a leading edge shock, a midspan damper shock, a second damper shock, and a trailing edge shock. Because of the angular view, the trailing edge shock details are limited to the outer wall near the blade trailing edge. Tip leakage vortices are seen along the suction surface of the blade making it difficult to identify shock patterns near the suction surface in the tip region. A weak oblique shock, slightly more oblique than design, extends from the blade leading edge to the suction surface near the trailing edge at the outer wall. The leading edge shock is oblique in accordance with design intent but does not appear to be completely canceled. The shock bends sharply to become nearly perpendicular at the intersection of the suction surface. A segment of this shock (very weak fringe) appears to continue obliquely, and intersects the blade further along the chord away from the tip region. Details of this shock near the suction surface are obscured, however, by the coalescence of the midspan damper and trailing edge shock fringes as well as the tip vortices. The leading edge shock becomes visible outboard of the midspan damper shock where it intersects with the shock from the midspan damper. The midspan damper shock appears to be a conical shaped shock emanating from the intersection of the leading edge of the midspan damper on the suction surface. The shock extends across the passage and the forward portion intersects at the pressure surface of the opposite blade well forward of the midspan damper leading edge. The shock extends radially outward and intersects the pressure surface immediately behind the blade leading edge. The shock extends across the passage and intersects the suction surface of the trailing edge near the outer wall. Further back in the passage, a second damper shock is observed that emanates from the intersection of the midspan damper and pressure side of the blade. This shock appears to originate at the midspan damper essentially along a plane perpendicular to the midspan damper. This shock is a highly warped surface which very nearly coincides with the midspan damper and trailing edge shock at the blade trailing edge.

The trailing edge shock appears as a single bright fringe at the blade trailing edge. This shock is similar to the design trailing edge shock but is displaced slightly forward of the trailing edge. The shock intersects the suction surface of the blade slightly downstream of the leading edge shock. The four shock fronts appear to coalesce near the blade trailing edge. The convergence of all the shock fringes makes it difficult to accurately define the shock pattern. Also, because of the limited view, the formulation of the trailing edge shock is not as well defined as the other major shock waves.

The shock system developed is superimposed on the conical development of the rotor sections in fig. 47. The position of the leading edge and trailing edge shocks is shown for comparison. As seen in fig. 47(a), the leading edge shock is slightly more oblique than design. The shock, however, bends sharply near the intersection at the suction surface. This deviation may be due to the blade boundary layer effect or tip leakage vortex or a combination thereof. The trailing edge shock is seen considerably forward of the anticipated shock location. Fig. 47(b) shows the shock development at the 13.8 percent span. Neither of the midspan damper shocks seen were considered in the design. The existence of these shocks undoubtedly affects the flow in the blade passage. The second

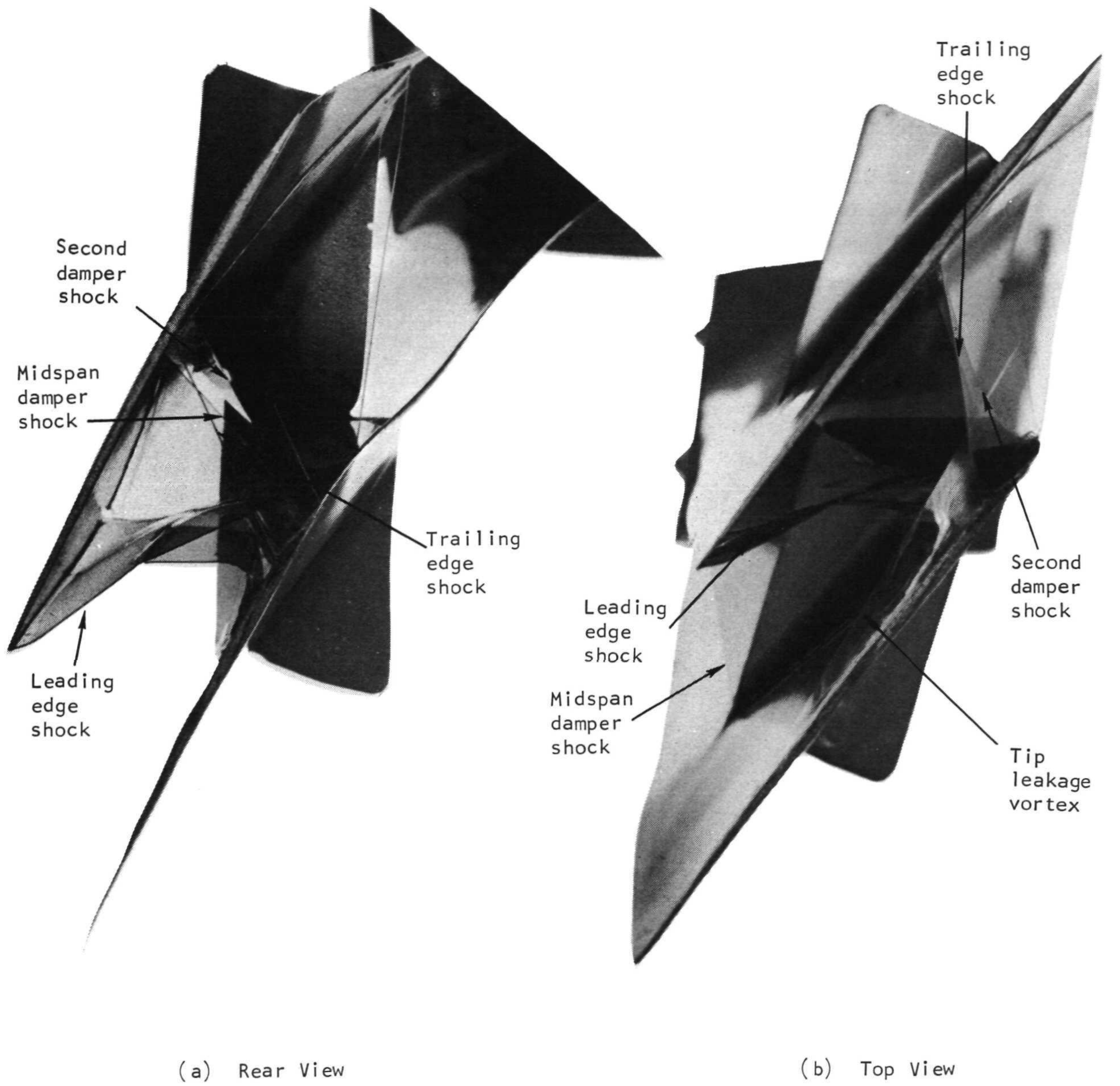

Figure 46.--Rotor Blade Model showing Passage Shock System at Design Speed and Design Pressure Ratio.

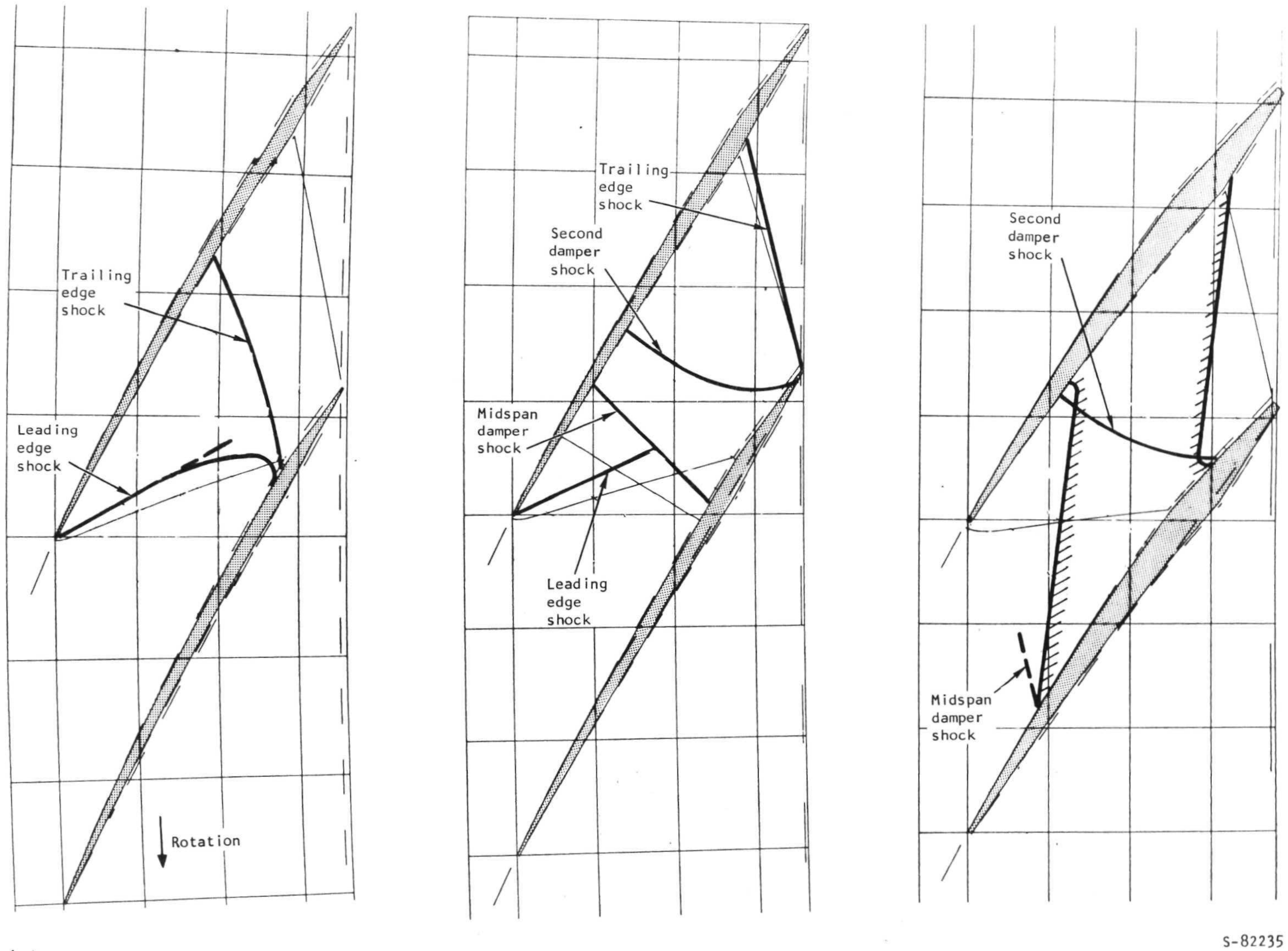

(a) Zero Percent Span (Tip).

(b) 13.8 Percent Span.

(c) 28.2 Percent Span.

Figure 47.--Rotor Passage Shock System Superimposed on Conical Development of Blade Section at Design Speed and Design Pressure Ratio.

damper shock is nearly normal to the flow direction, and extends from the midspan to a point slightly inboard of the tip section. Fig. 47(c) shows the shock development at the 28.2 percent span, just outboard of the midspan damper.

The rotor relative Mach number as determined from the blade element performance is shown as a function of percent span in Fig. 48. The inlet relative Mach number is essentially in accordance with design for the outboard section. The exit relative Mach number is supersonic over 22 percent of the span but slightly lower than design.

The rotor tip pressure countour plots at design speed and pressure ratio are shown in fig. 49. The shock waves developed from the blade model at the rotor tip are superimposed on the plot. It may be surmised from this plot that a weak oblique shock would exist at the leading edge if the pressure contours were shifted slightly forward. The pressure contour islands are also consistent with the sharp bend in the leading edge shock near the suction surface. Additional shifting and recontouring of the pressure contours would be required to be consistent with the trailing edge shock. The static pressure levels are generally consistent with the shock patterns observed.

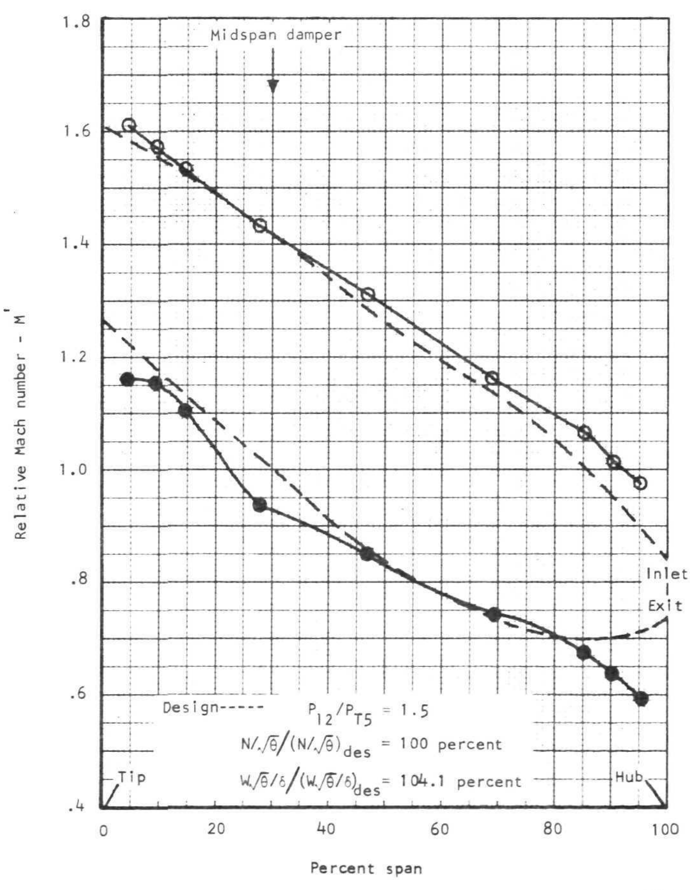

Figure 48.--Rotor Relative Mach Number at Design Speed and Design Pressure Ratio.

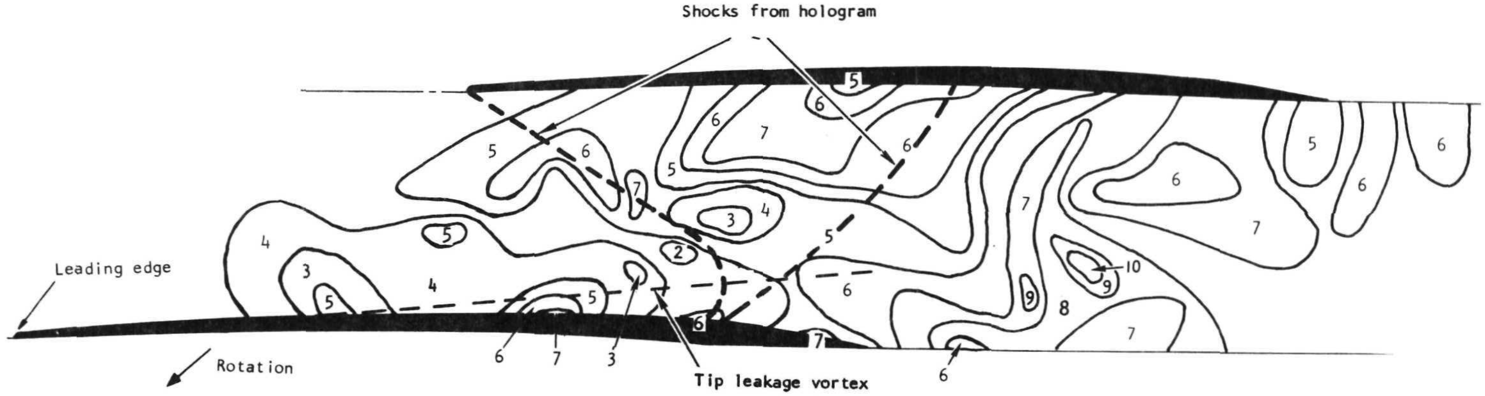

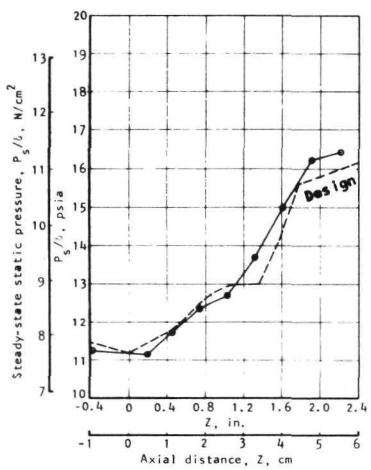

Reading	128
$\frac{N/\sqrt{\theta}}{N/\sqrt{\theta}_{des}}$	= 1.00
$\frac{W\sqrt{\theta}/\delta}{W\sqrt{\theta}/\delta_{des}}$	= 1.041
P_{T12}/P_{T5}	= 1.505

Static pressure contour code		
Code number	Static pressure range	
	psia	N/cm^2
1	3 to 5	2.07 to 3.45
2	5 to 7	3.45 to 4.83
3	7 to 9	4.83 to 6.21
4	9 to 11	6.21 to 7.58
5	11 to 13	7.58 to 8.96
6	13 to 15	8.96 to 10.34
7	15 to 17	10.34 to 11.72
8	17 to 19	11.72 to 13.10
9	19 to 21	13.10 to 14.48
10	21 to 23	14.48 to 15.86
11	23 to 25	15.86 to 17.24

S-81873

Figure 49.--Rotor Blade Tip Static Pressure Contours with Shock System Indicated at Design Speed and Design Pressure Ratio.

A similar model of a rotor blade shock system was developed for the 100 percent design speed and maximum flow condition. For this condition, the stage pressure ratio was 1.369:1 at the same 4 percent overflow condition. The shock system was developed from holograms 164, 290, 292, 335, 337, and 338.

The shock patterns developed are shown superimposed on the rotor blade section conical plots in fig. 50. Referring to fig. 50(a), the leading edge shock appears as a weak oblique shock. This shock is essentially in accordance with design and remains completely oblique to the intersection of the blade suction surface. The sharp bend in this shock near the suction surface that was seen at the design pressure ratio condition (fig. 46 and 47) was not present. The trailing edge shock is located slightly forward of the trailing edge, and intersects the leading edge shock at the same point on the blade suction surface. This shock is, however, consistent with the anticipated trailing edge shock angle. As stated earlier, locating the trailing edge shock accurately is extremely difficult. The tip vortex at this condition appears to be confined to the extreme outer wall. The shock waves at the 13.8 percent and 28.2 percent span were very similar to the shocks developed at the design speed and design pressure ratio condition (see fig. 47).

The rotor tip pressure contour plots at this condition are shown in fig. 51. As seen, many of the contours are again normal rather than parallel to the anticipated shock direction. It is evident from these plots that the rotor tip pressure contours do not explicitly define the shock pattern. The contour plots are obscured by factors such as tip clearance, wall boundary layer, effect of transducer size and sensitivity on signal wave forms, tip leakage vortices, and accuracy in defining the exact blade position relative to the signal.

Aerodynamic analysis of holograms at 90 percent speed.--Rapid double-exposure holograms recorded at 90 percent design speed for maximum and mid-flow range conditions are shown in fig. 52 (holograms 311, 312, 313, 318, 319, and 320). The hologram taken at the mid-flow range condition shows a strong and apparently normal shock in the leading edge region indicating that the rotor passage is unstarted in the tip region. The presence of a strong normal shock is consistent with the low level of stage efficiency at this speed. Both overall and blade element data show that the level of efficiency decreases rather uniformly up to 90 percent design speed. The efficiency then abruptly increases by approximately 3 points when speed is increased to 95 percent design speed, indicating transition from the unstarted to the started condition. The hologram obtained at wide-open-throttle (maximum flow) condition, however, shows that the leading edge shock is nearly oblique, and is indicative of the tip passage being started. This transition between the started and unstarted modes occurring at constant speed by reducing flow was further substantiated by the following from ref. 6.

(1) The level of rotor only adiabatic efficiency decayed from 88.5 percent at maximum flow to 85.8 percent with just a 1.3 percent reduction in flow (stage data did not reflect this efficiency characteristic step because of large stator losses).

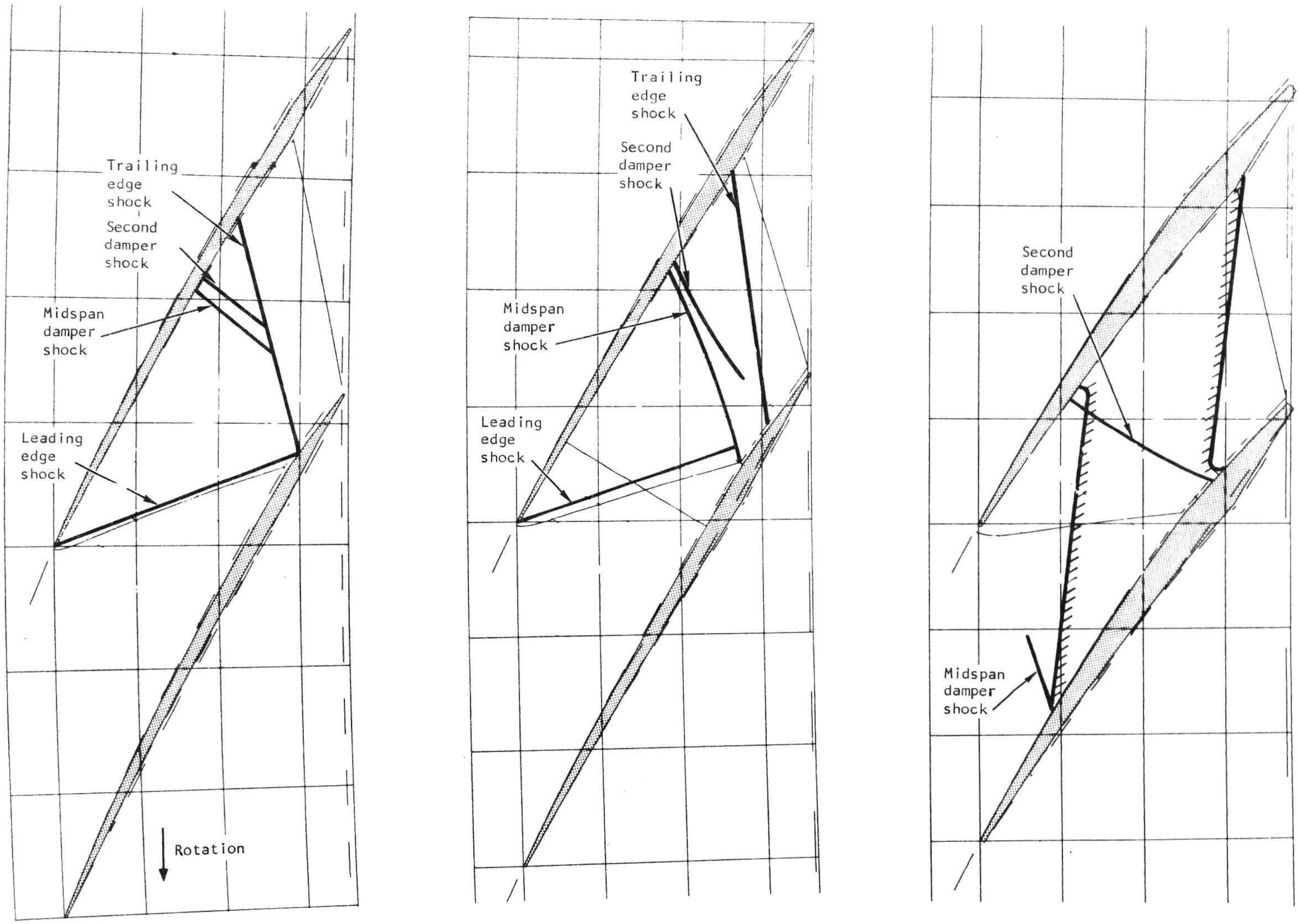

(a) Zero Percent Span (Tip). (b) 13.8 Percent Span. (c) 28.2 Percent Span.

Figure 50.--Rotor Passage Shock System Superimposed on Conical Development of Blade Section at Design Speed and Maximum Flow Condition.

S-82233

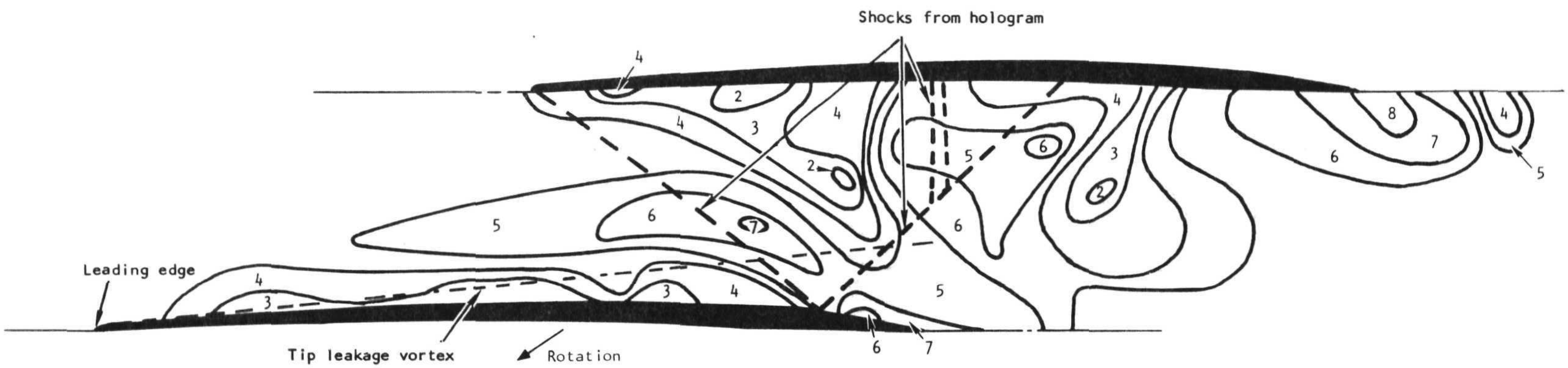

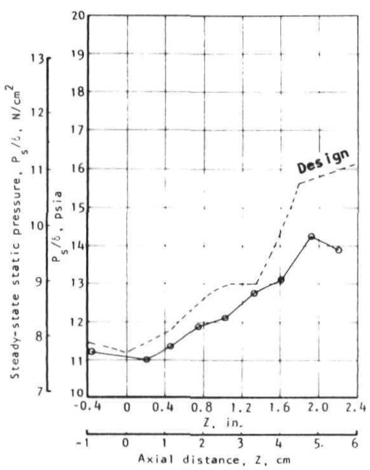

Reading	107
$\frac{N/\sqrt{\theta}}{N/\sqrt{\theta}_{des}}$	= 1.00
$\frac{W\sqrt{\theta}/\delta}{W\sqrt{\theta}/\delta_{des}}$	= 1.040
P_{T12}/P_{T5}	= 1.369

Static pressure contour code		
Code number	Static pressure range	
	psia	N/cm^2
1	3 to 5	2.07 to 3.45
2	5 to 7	3.45 to 4.83
3	7 to 9	4.83 to 6.21
4	9 to 11	6.21 to 7.58
5	11 to 13	7.58 to 8.96
6	13 to 15	8.96 to 10.34
7	15 to 17	10.34 to 11.72
8	17 to 19	11.72 to 13.10
9	19 to 21	13.10 to 14.48
10	21 to 23	14.48 to 15.86
11	23 to 25	15.86 to 17.24

S-8188 7

Figure 51.-- Rotor Blade Tip Static Pressure Contours with Shock System Indicated at Design Speed and Maximum Flow Condition.

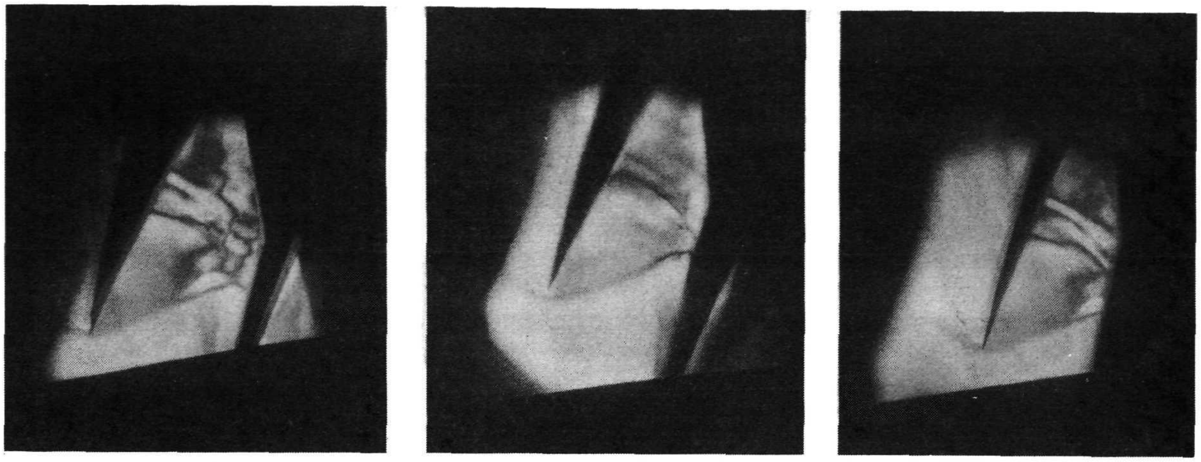

(a) Maximum Flow Condition showing Oblique Shock (Holograms 311, 312, and 313).

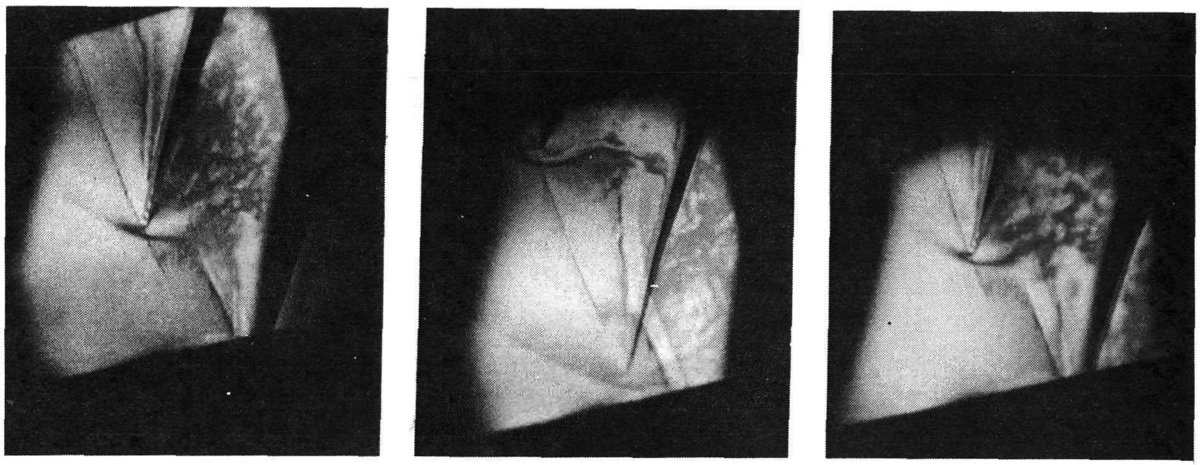

F-19084

(b) Midflow Condition showing Normal Shock (Holograms 318, 319, and 320).

Figure 52.--Reconstructed, Rapid Double-Exposure Holograms showing Rotor Started and Unstarted Condition at 90 percent Design Speed at Maximum and Mid-Flow Range.

(2) Rotor tip high-frequency-response pressure traces obtained in the region between wide-open-throttle and the immediately adjacent data point show large instabilities in pressure levels (passage-to-passage) in the area of the leading edge.

To further investigate the rotor passage starting development that occurred at 90 percent speed with only small closure of the discharge throttle, a series of holograms (358, 356, 352, 351, 349, and 347) was taken at 80 to 100 percent design speed along a constant-throttle line at approximately mid-flow range. Referring to fig. 53, the upper left-hand view shows a reconstruction of hologram 358 taken at 80 percent design speed. At this speed, a strong detached bow shock is evident. As the speed is increased to 86 percent (hologram 356), the bow shock is still detached, but begins to approach the blade leading edge. At 90 percent design speed (hologram 352) a strong normal shock, attached to the blade leading edge, is developed in the forward passage section (essentially a duplication of what is seen in holograms 318, 319, and 320). Referring to the lower series of views, at 92 percent design speed (hologram 351), a weak, nearly oblique shock is seen, indicating that the passage is started. As the speed is increased through 96 percent (hologram 347) to 100 percent design speed (hologram 307), the oblique shock continues to sweep further into the passage.

The rotor tip contour plots obtained at 90 percent design speed for the two flow conditions are presented in figs. 54 and 55. Fig. 54 shows the contour plots for the maximum flow condition, and fig. 55 shows a similar plot for the mid-flow range condition. The leading edge shock and tip leakage vortex that was observed from the holograms are superimposed on the plots. A comparison of the two resulting contour plots shows a noticeably different pressure contour formation. For the condition in which a near oblique shock is observed (see figs. 52(a) and 54), the pressure-contours are contained within the passage and appear to be somewhat in alignment with the oblique shock. On the other hand, in the contour plots for the mid-flow range conditions in which a strong normal shock is observed (see figs. 52(b) and 55), the pressure contours extend considerably forward of the leading edge with an attendant increase in static pressure level. The high static pressure level is an indication of a strong normal shock.

Aerodynamic analysis of hologram at 95 percent design speed.--A rotor blade model showing the interblade shock system at 95 percent design speed and mid-flow range is shown in fig. 56. These shock waves were developed from a series of rapid double-exposure holograms taken at the same condition using the superpositioning technique described earlier (holograms 278, 279, 280, 332, 333, and 334). A reconstruction of one of the holograms (332) used for the analysis was shown earlier in fig. 39.

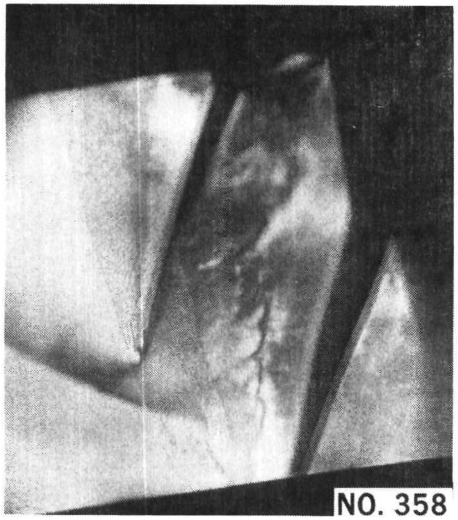

(a) 80% Design Speed

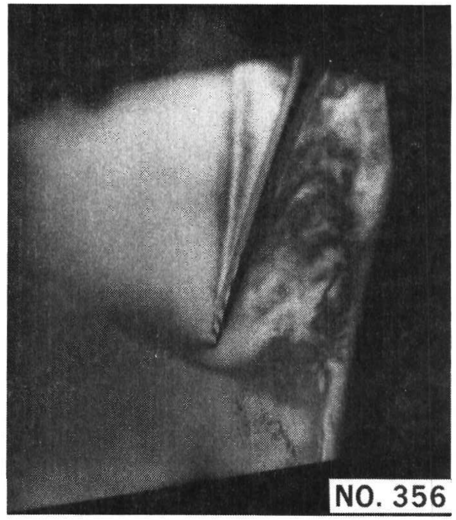

(b) 86% Design Speed

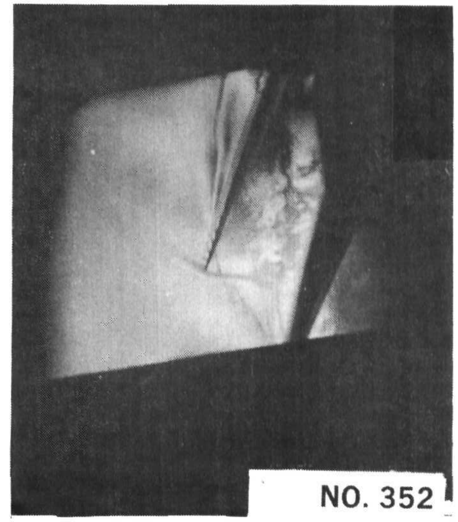

(c) 90% Design Speed

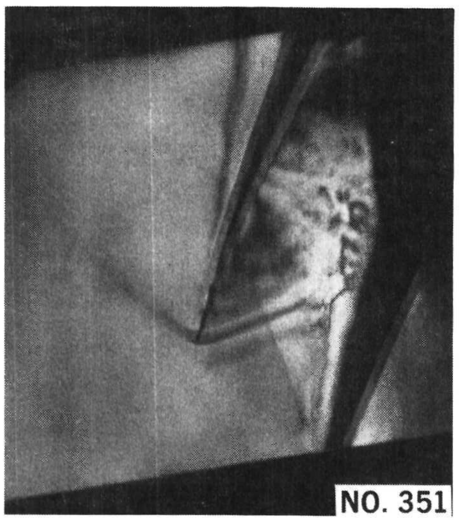

(d) 92% Design Speed

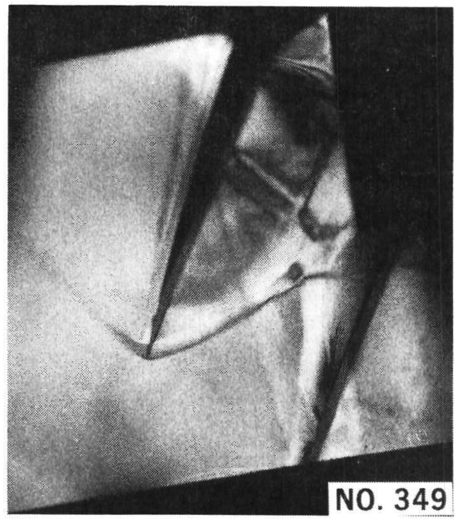

(e) 96% Design Speed

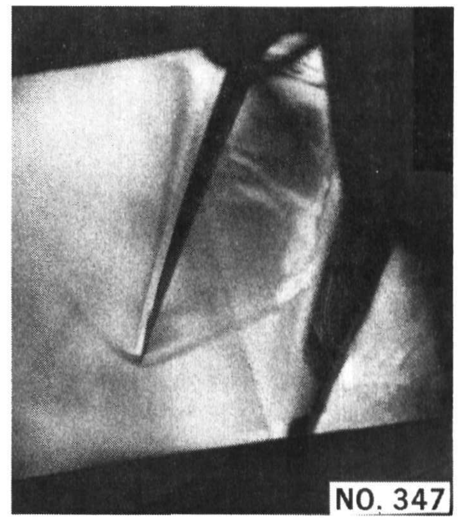

(f) Design Speed

F-18523

Figure 53.--Reconstructed Rapid, Double-Exposure Holograms showing Rotor Leading Edge Shock at Various Speeds.

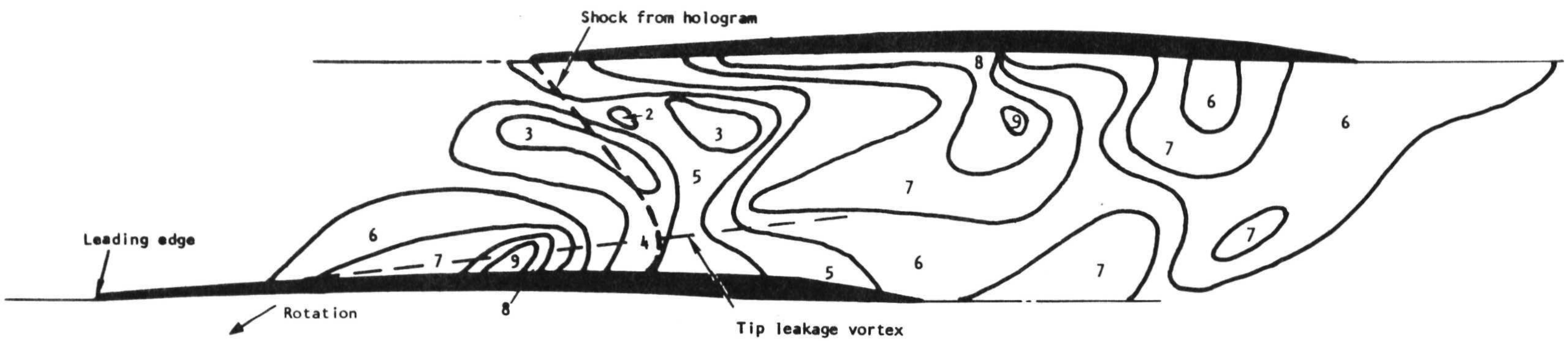

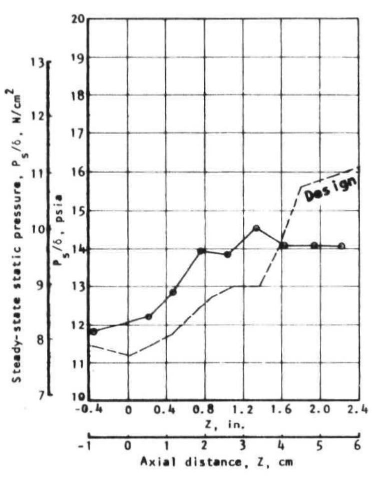

Reading	103
$\frac{N/\sqrt{\theta}}{N/\sqrt{\theta}_{des}}$	= 0.90
$\frac{W\sqrt{\theta}/\delta}{W\sqrt{\theta}/\delta_{des}}$	= 0.984
P_{T12}/P_{T5}	= 1.320

Static pressure contour code		
Code number	Static pressure range	
	psia	N/cm²
1	3 to 5	2.07 to 3.45
2	5 to 7	3.45 to 4.83
3	7 to 9	4.83 to 6.21
4	9 to 11	6.21 to 7.58
5	11 to 13	7.58 to 8.96
6	13 to 15	8.96 to 10.34
7	15 to 17	10.34 to 11.72
8	17 to 19	11.72 to 13.10
9	19 to 21	13.10 to 14.48
10	21 to 23	14.48 to 15.86
11	23 to 25	15.86 to 17.24

S-81880

Figure 54.--Rotor Blade Tip Static Pressure Contours with Shock System Indicated at 90 percent Design Speed and Maximum Flow Condition.

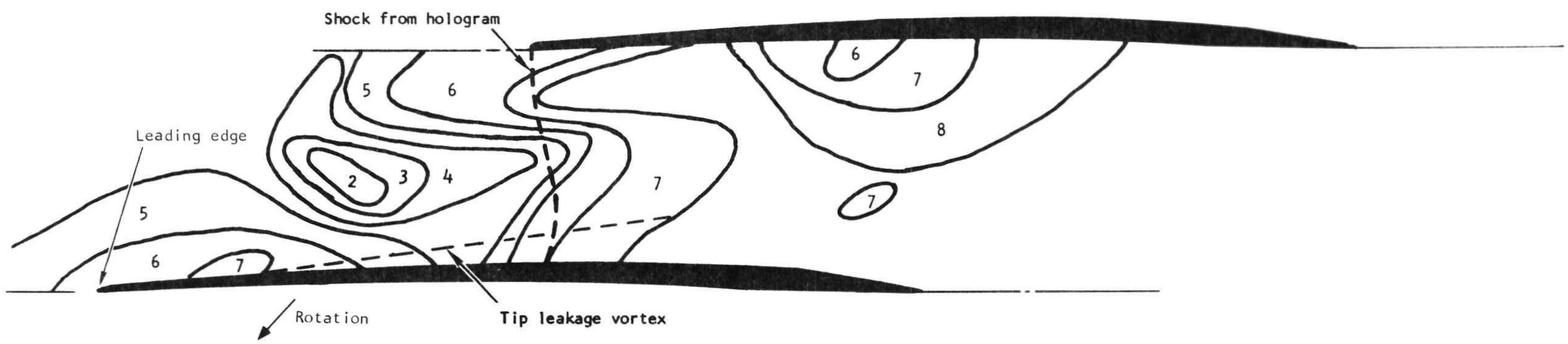

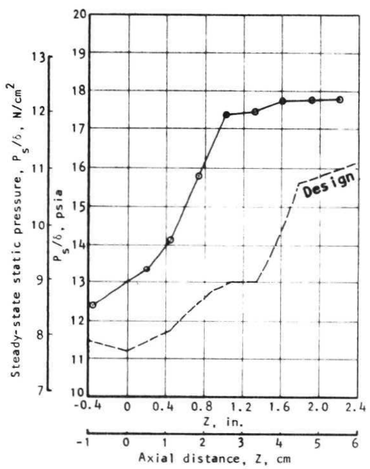

Reading	106
$\frac{N/\sqrt{\theta}}{N/\sqrt{\theta}_{des}}$	= 0.90
$\frac{W\sqrt{\theta}/\delta}{W\sqrt{\theta}/\delta_{des}}$	= 0.942
P_{T12}/P_{T5}	= 1.524

Static pressure contour code		
	Static pressure range	
Code number	psia	N/cm^2
1	3 to 5	2.07 to 3.45
2	5 to 7	3.45 to 4.83
3	7 to 9	4.83 to 6.21
4	9 to 11	6.21 to 7.58
5	11 to 13	7.58 to 8.96
6	13 to 15	8.96 to 10.34
7	15 to 17	10.34 to 11.72
8	17 to 19	11.72 to 13.10
9	19 to 21	13.10 to 14.48
10	21 to 23	14.48 to 15.86
11	23 to 25	15.86 to 17.24

S-81879

Figure 55.--Rotor Blade Tip Static Pressure Contours with Shock System Indicated at 90 percent Design Speed and Mid-Flow Condition.

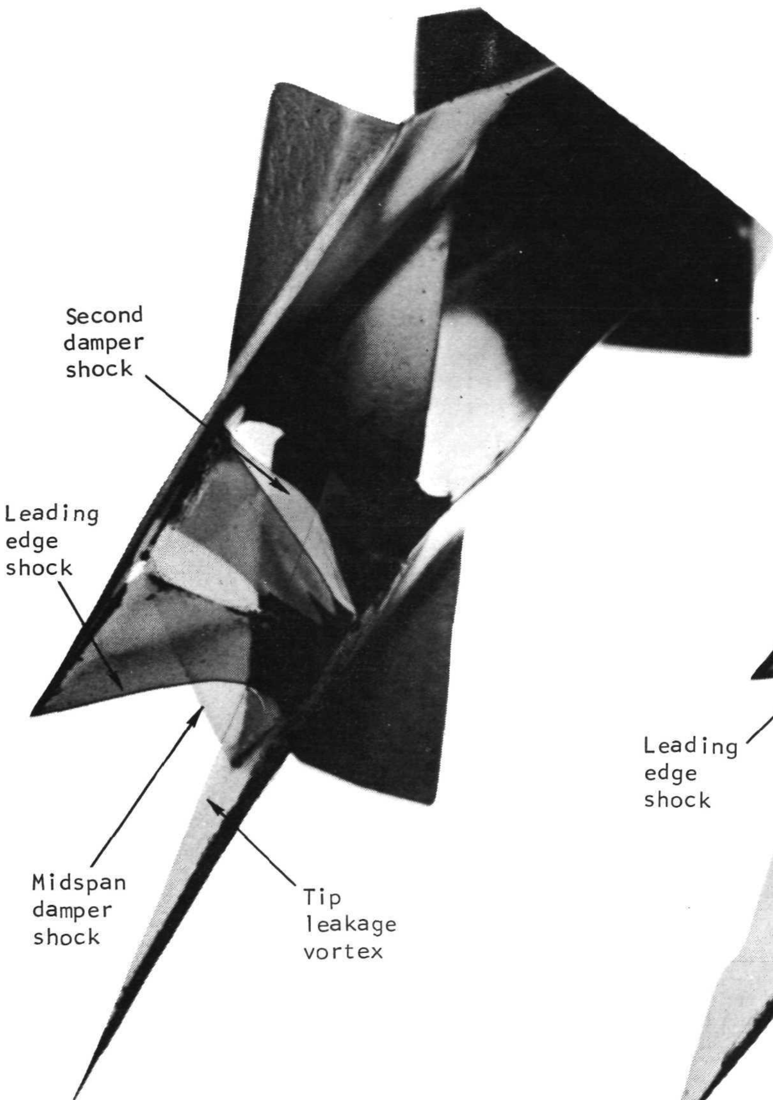

(a) Rear View

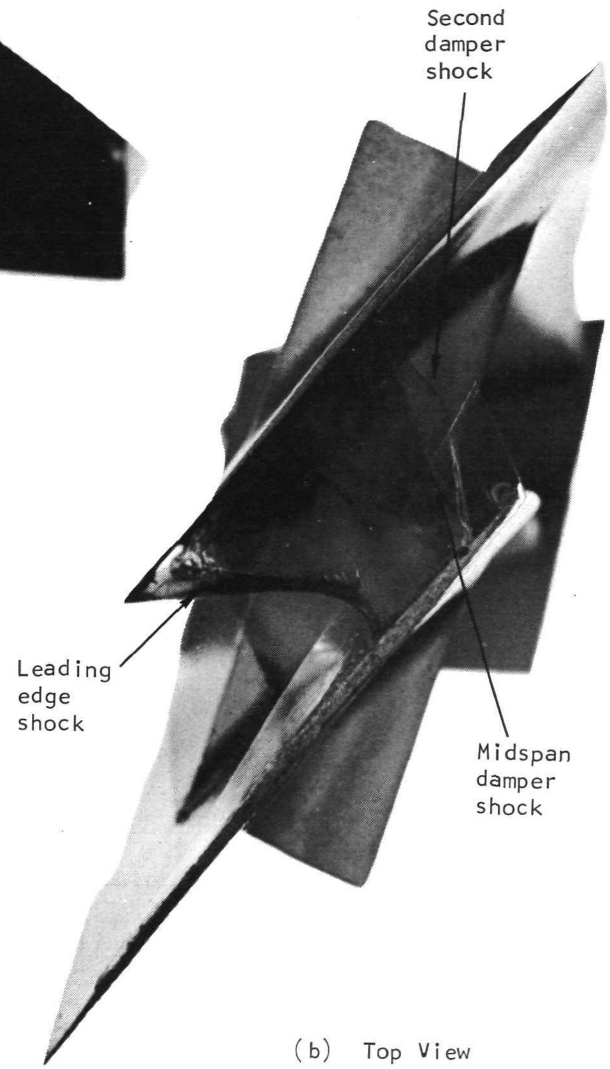

(b) Top View

F-18514

Figure 56.--Rotor Blade Model showing Passage Shock System at 95 percent Design Speed.

Referring to fig. 56, the shock system comprises three distinct shock waves identified as a leading edge shock, a midspan damper shock, and a second damper shock. In addition, a tip leakage vortex is seen along the suction surface of the blade. This tip vortex appears to emanate from the leading edge suction surface and extends approximately to mid-channel. The tip vortex tends to obscure shock definition near the suction surface in the tip region. A rather weak oblique shock is attached to the blade leading edge and terminates at the suction surface of the blade near the trailing edge. The shock bends to become nearly perpendicular at the intersection of the suction surface. The design intent of the leading edge shock was to be always oblique. This deviation may be due to either blade boundary layer effects at the suction surface, tip leakage vortices, or a combination of these effects. The tip vortex was quite evident in the majority of the holograms and appeared to have a dominant effect on the shock waves at the outer wall. The leading edge shock extends spanwise to just outboard of the midspan damper and intersects the shock from the midspan damper leading edge. This shock starts at the leading edge of the midspan damper (suction surface) and extends from blade to blade. The shock is swept in the direction of flow at an angle that is slightly less than the sweep back angle of the midspan damper. It extends across the passage and intersects the outer wall near the blade trailing edge. Because of the limited viewing angle, the exact leading edge of the shock front across the passage could not be determined. The shock front appears as bright fringes when viewed at an angle normal to the interference fringe. Based on the location and characteristic of the shock wave, it appears to be somewhat conical in shape, starting at the midspan damper leading edge of the blade suction surface. This shock intersects the pressure surface of the adjacent blade slightly behind the leading edge. A second damper shock in the forward section of the passage and slightly behind the midspan damper shock is observed. This shock, which appears to be a rather strong oblique shock, emanates from the midspan damper region and extends to the outer surface almost coincident with the midspan damper shock. The trailing edge shock was not evident at this speed.

The shock system developed is shown in fig. 57 by heavy lines superimposed on the conical development of the rotor blade section. The two-shock system at the design point is shown by the lighter lines. Rotor sections are shown for three streamlines corresponding to (a) tip, (b) 13.8 percent span, and (c) 28.2 percent span. The dotted lines represent the effective blade surface, and the solid lines represent actual blade surface obtained by considering boundary layer displacement thickness corrections. The measured shock angles, locations, and intersections of shock and blade surfaces are shown. At this condition, the rotor inlet relative number determined from the blade element data is supersonic in the outer 30 percent span. Exit relative Mach number is subsonic throughout the span.

The rotor tip pressure contour plots at 95 percent speed and mid-flow range are shown in fig. 58. The shock patterns at the rotor tip section are shown superimposed on the plots. The resulting contour plots show no well-defined shock patterns. Interpretation of these contours is extremely difficult since many contours are normal rather than parallel to the anticipated shock direction and to the shock direction indicated by the hologram. Tip leakage vortex is again evident but appears to be confined mostly to the outermost tip

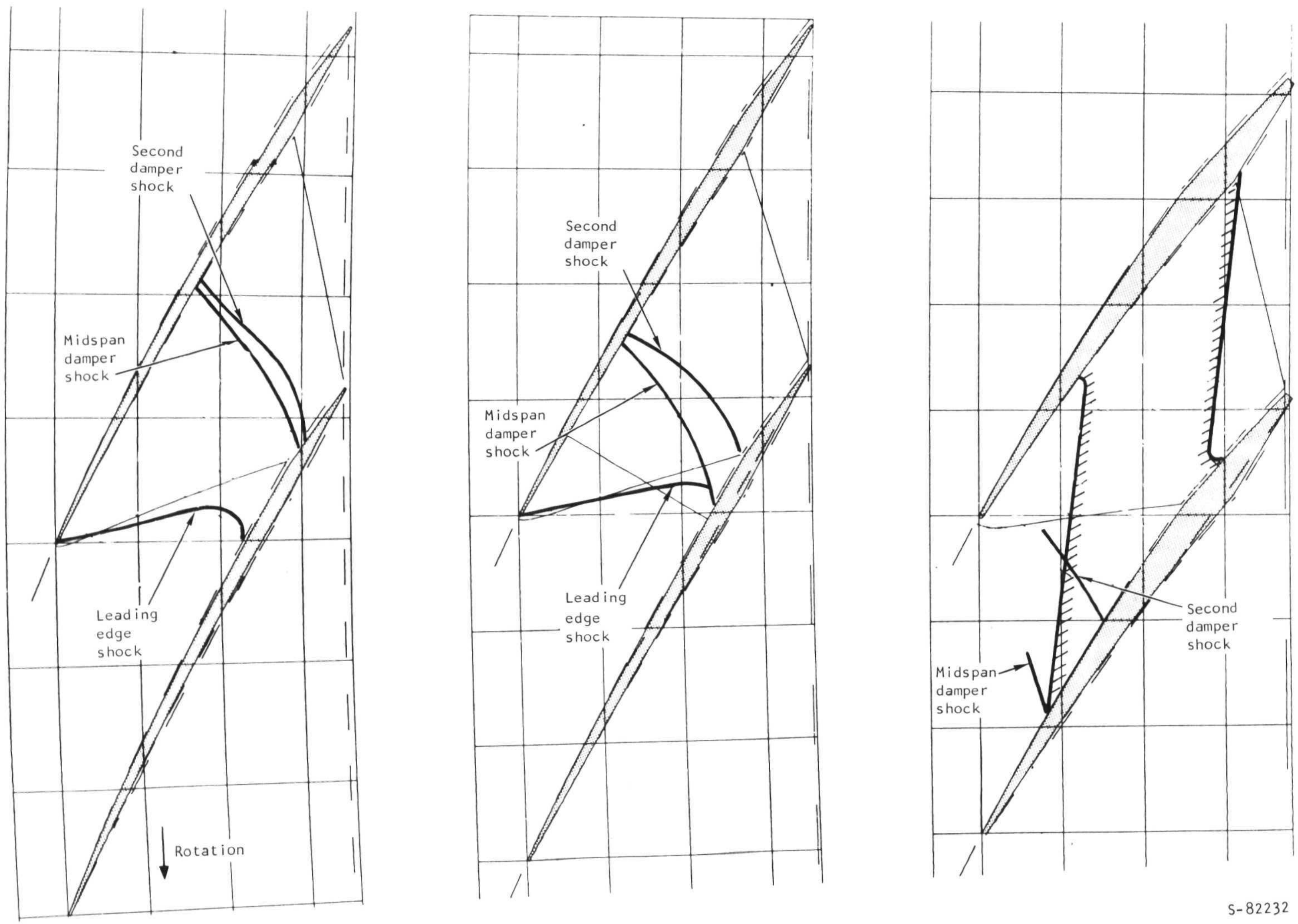

(a) Zero Percent Span (Tip).   (b) 13.8 Percent Span.   (c) 28.2 Percent Span.

Figure 57.--Rotor Passage Shock System Superimposed on Conical Development of Blade Section at 95 percent Design Speed and Mid-Flow Condition.

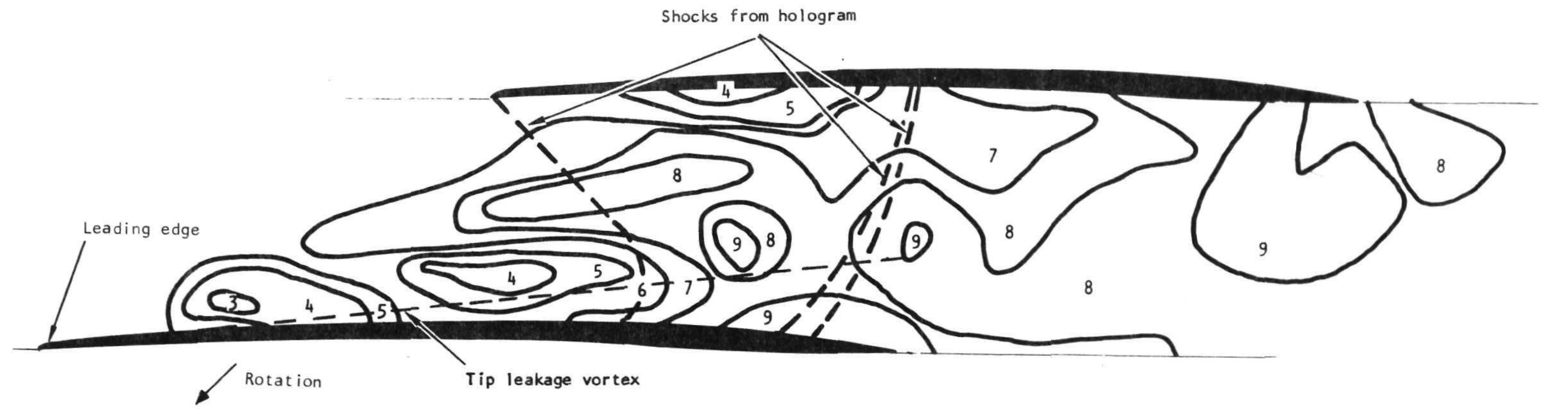

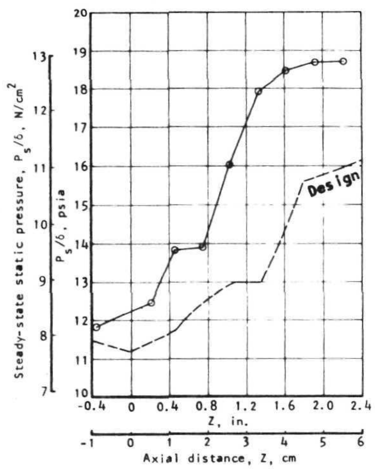

Reading	118
$\frac{N/\sqrt{\theta}}{N/\sqrt{\theta}_{des}}$	= 0.95
$\frac{W\sqrt{\theta}/\delta}{W\sqrt{\theta}/\delta_{des}}$	= 0.995
P_{T12}/P_{T5}	= 1.604

Static pressure contour code		
Code number	Static pressure range	
	psia	N/cm^2
1	3 to 5	2.07 to 3.45
2	5 to 7	3.45 to 4.83
3	7 to 9	4.83 to 6.21
4	9 to 11	6.21 to 7.58
5	11 to 13	7.58 to 8.96
6	13 to 15	8.96 to 10.34
7	15 to 17	10.34 to 11.72
8	17 to 19	11.72 to 13.10
9	19 to 21	13.10 to 14.48
10	21 to 23	14.48 to 15.86
11	23 to 25	15.86 to 17.24

S-81875

Figure 58.--Rotor Blade Tip Static Pressure Contours with Shock System Indicated at 95 percent Design Speed.

section at this condition. This tip vorticity may have an effect on the static pressure contours and thus complicate the interpretation of pressure contours. The leading edge shock bends sharply in the vicinity of the tip vortex and becomes nearly perpendicular at the suction surface. The midspan damper and second damper shocks intersect the outer wall at essentially the same location. As seen, these two shocks at the outer wall are almost normal to the mean flow direction. The contour islands in the area of the tip vorticity are consistent with the region of turbulence indicated in the holograms. In summary, the static pressure contours did not explicitly define shock locations, however, the region of static pressure levels appear to be consistent with the shock patterns defined in the hologram.

Aerodynamic analysis of holograms at 110 percent design speed.--The inter-blade shock system for 110 percent design speed and mid-flow range is shown in fig. 59. At this condition, the rotor inlet relative velocity is considerably higher than design (approximately 1.85 at the tip). The exit relative Mach numbers were essentially at design. At this overspeed condition, the overall stage pressure ratio was 1.597 at a flow rate of 108.2 percent of design flow. Hologram 167 was used for development of the shock system.

Referring to fig. 59, the three major shock waves identified are the leading edge shock, midspan damper shock and the second damper shock. The tip leakage vortex is evident at this condition but appears largely confined to the extreme outer tip. Effect of tip vortex on shock disturbance at the tip is minimal. A weak oblique passage shock, considerably more oblique than design, extends from the blade leading edge to the suction surface of the trailing edge. The leading edge shock intersects the suction surface at precisely the blade trailing edge. The leading edge shock starts spanwise outboard of the midspan damper and intersects the shock from the midspan damper. At this overspeed condition, the midspan damper shock is swept into the direction of flow but at a considerably greater angle than previously seen at 95 and 100 percent speed. The intersection of this shock on the pressure surface occurs well within the passage. This shock extends across the passage and intersects the blade suction surface below the outer tip. The midspan damper shock is also surmised to be conical in shape. Another strong oblique shock appears to start in the midspan damper region slightly behind the midspan damper shock, and extends toward the outer wall. This shock appears to be essentially parallel to the midspan damper shock.

The shock system developed for this overspeed condition is shown superimposed on the conical plots for the three rotor sections in fig. 60. Fig. 60(a) shows the leading edge shock extending from the blade leading edge to the blade trailing edge. This shock becomes progressively more oblique as speed is increased. This can be seen by comparing the leading edge shocks for a 90, 95, 100, and 110 percent speed condition. Both midspan damper and secondary passage shocks normally seen at the outer wall are not evident. Fig. 60(b) and 60(c) show the shock development of the midspan damper and second damper shocks at 13.8 and 28.2 percent span. As indicated earlier, the midspan damper shock angle is considerably larger, resulting in the shock being swept further into the passage. At this overspeed condition, rotor tip pressure data were not recorded. Rotor tip pressure contour plots are therefore not available for the 110 percent design speed condition.

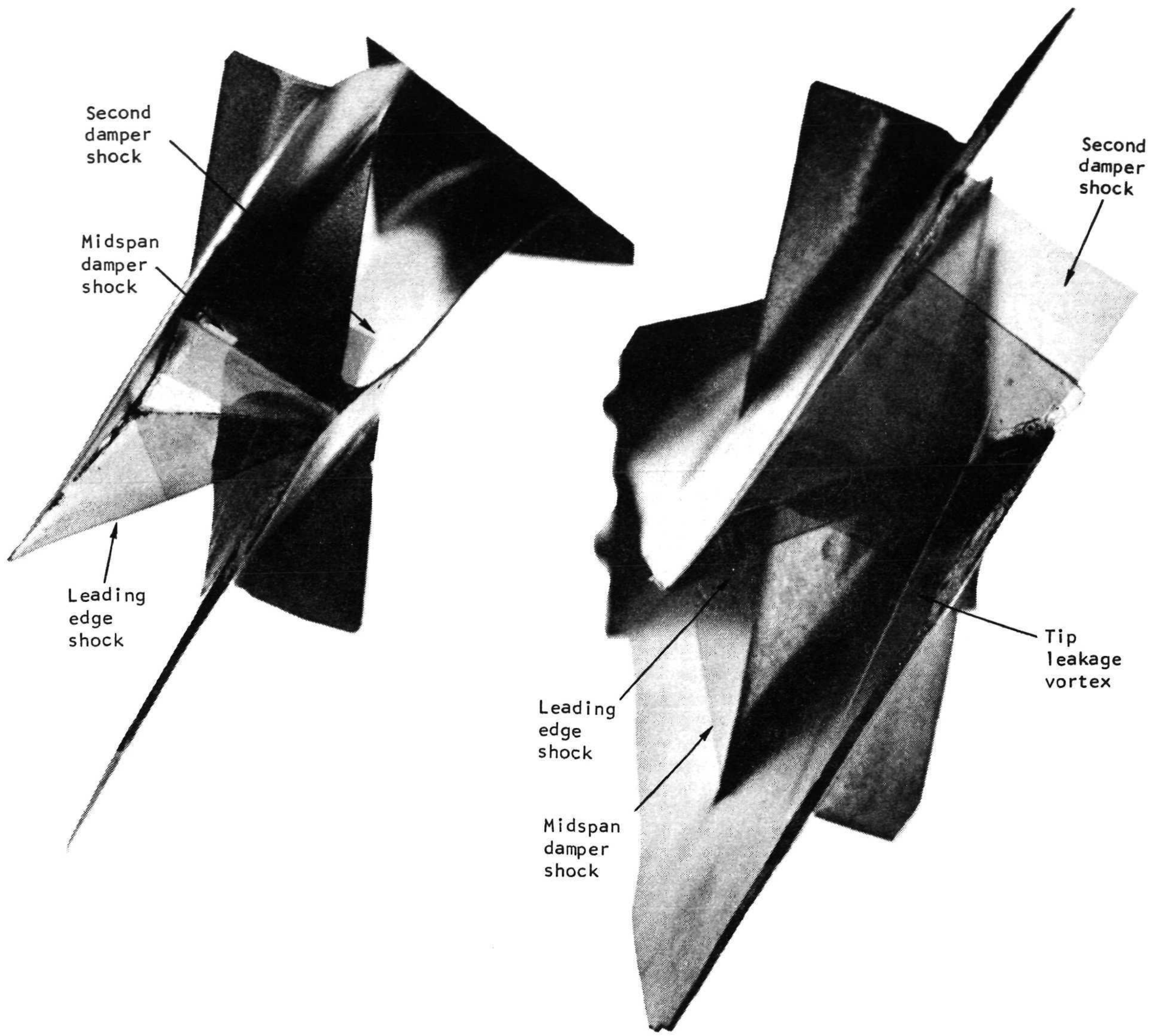

(a) Rear View

(b) Top View

F-18515

Figure 59.--Rotor Blade Model showing Passage Shock System at 110 percent Design Speed.

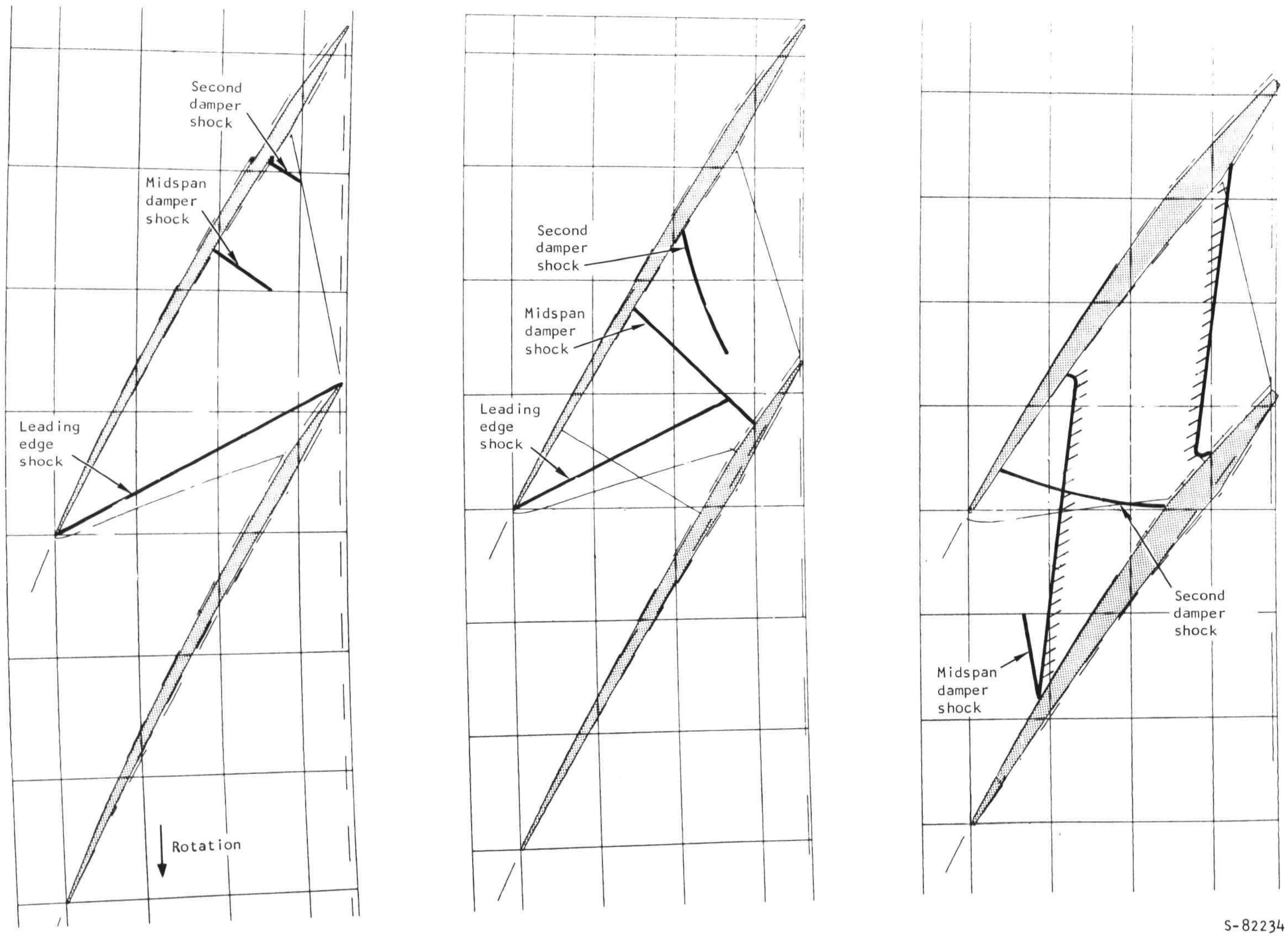

(a) Zero Percent Span (Tip). (b) 13.8 Percent Span. (c) 28.2 Percent Span.

Figure 60.--Rotor Passage Shock System Superimposed on Conical Development of Blade Section at 110 percent Design Speed and Mid-Flow Condition.

CONCLUDING REMARKS

The application of pulsed laser transmission holography for flow visualization within the rotating blade passages of a transonic fan stage was successfully demonstrated. A holocamera was developed for recording both single- and double-exposure, bright-field holograms and dark-field, scattered-light holograms. A summary of the major accomplishments follows.

(1) The rapid, double-exposure holograms provided excellent recordings with respect to the location and identification of shock fronts in the forward passage section. However, details in the trailing edge region were not well defined. Enlargement of the viewing window and holographic plate would increase the image area and improve the quality of the hologram. Standard 8 by 10 in. (20.3 by 25.4 cm) holographic plates are commercially available.

(2) Rapid, double-exposure holograms provided the most consistency and clarity because of their insensitivity to extraneous interference fringes. These holograms were made using a laser that emitted two pulses within a very short interval. Double-pulsing moved the shocks slightly and enhanced the shock fringes recorded. A double (inter-cavity) Kerr cell arrangement capable of producing 5-μsec pulses was developed. Use of a second power supply would provide even shorter pulse separation on the order of 2 μsec. Shorter pulse separation would be highly desirable and would produce even sharper shock fringes and possibly more clearly define shock intensity.

(3) A technique for interpreting the reconstructed hologram and transferring the shock system to a model blade was developed. This technique consisted of superimposing the three-dimensional shadow image from the hologram onto the model blades. The shock fringes were then located by parallax. Models of the shock system were developed for 95, 100, and 110 percent design speed. These models compared favorably with theoretical predictions and the overall and blade element performance data. At 100 percent design speed, the hologram showed four distinct shocks: an oblique leading edge shock, a conical shock associated with the midspan damper, a second damper shock, and a trailing edge shock. The midspan damper and second damper shocks were not considered in the design but undoubtedly affect flow condition in the tip region. At the maximum flow condition, the leading edge shock is considerably more oblique than design. As the stage is throttled (increased back pressure), the leading edge shock approaches design.

(4) Transition of the rotor passages from the started to the unstarted mode was successfully demonstrated. Holograms taken at 90 percent design speed (maximum flow condition) showed the leading edge shock to be nearly oblique, indicating that rotor passage was started. As the stage was back-pressured to mid-flow range, a strong normal shock developed at the leading edge, indicating an unstarted condition. This

condition was consistent with a corresponding decay in rotor efficiency and large fluctuations in pressure levels (passage-to-passage) in the area of the leading edge.

(5) The angular view and midspan damper restricted the image area of the rotor passage. Enlarging the windows would greatly improve the field of view. Modification or removal of the midspan dampers in one or more passages would be ideal from the standpoint of rotor passage visibility as well as for aerodynamic considerations. This can be coupled with the aerodynamic evaluation to study the influence of midspan damper design (i.e. thickness, sweepback angle, and location).

(6) A limited number of scattered-light holograms in which 30-micron-diameter particles were injected in the flow stream were successfully recorded. By tracing the particle path, and knowing the exposure time, flow velocity was determined. Because of the 50-nsec pulse duration limitation, scattered-light holograms were restricted to rotor speeds on the order of 1000 rpm (104.7 rad/sec). A pulse duration of $\cong$5 nsec is required at the higher speed. Shorter laser pulse duration can be obtained by the use of a pulse chopper.

(7) Oil leakage past the front carbon face seal centrifuged out along the blades onto the viewing window and caused additional interference fringes. Simple design modification could be made to eliminate this problem.

(8) Further work on long-pulse, single-exposure holograms could lead to improved holograms with better shock fringe definition.

APPENDIX A

BLADE ELEMENT PERFORMANCE DATA FOR UNIFORM INLET FLOW

This appendix presents representative blade element performance data for the transonic fan stage tested (ref. 6). Data are included for the following test points.

Data Point	$N/\sqrt{\theta}/(N/\sqrt{\theta})_{des}$	Reading No.
2	0.90	106
4	0.95	118
6	1.00	128
8	1.10	113

ROTOR EXIT TRAVERSE PLANE . READING NUMBER 106 TIME 10H 32M 27S UNIFORM INLET FLOW STATOR ANGLE 2.00

MASS AVERAGED PT	22.5522	(22.7117)
MASS AVERAGED TT	598.5466	(601.1857)
TOTAL WEIGHT FLOW	135.0023	(PROBE INTEGRATION)
CORR. TOTAL FLOW	135.6588	

PROBE TYPE - NASA 4 PARAMETER LOCATION - STA 9.0, 104 DEG.

IMMERSION (IN.)	0.3100	0.6400	0.9600	1.8100	3.0200	4.4300	5.3600	5.6800	5.9500
TOTAL PRESSURE	23.1772	23.6249	23.4590	23.1496	22.7029	21.9991	21.6036	21.4291	21.5914
STATIC PRESSURE	17.5151	17.2459	17.0679	16.7716	16.6957	16.2735	16.0092	15.9234	16.0270
WEDGE PRESSURE	18.2611	18.1718	18.0033	17.7153	17.5505	17.0753	16.7900	16.6848	16.7988
TOTAL TEMPERATURE	620.3714	616.3206	608.9847	613.4796	594.6461	586.6539	583.0947	581.7969	586.9167
ANGLE (DEG.)	37.8076	34.8802	34.2084	41.1252	39.4633	41.6038	41.5557	42.7543	45.9163
APPARENT MACH NO.	0.5939	0.6242	0.6269	0.6304	0.6178	0.6128	0.6114	0.6088	0.6098

PROBE TYPE - NASA 2 PARAMETER LOCATION - STA 9.0, 300 DEG.

STATIC PRESSURE	17.6828	17.7355	17.8591	17.9775	17.7418	17.3554	16.9973	16.8485	16.7239
WEDGE PRESSURE	17.7818	17.8450	17.9604	18.0673	17.8268	17.4336	17.0754	16.9261	16.8089
ANGLE (DEG.)	34.9360	29.0144	34.2568	31.4530	34.2150	35.5399	36.6744	37.3158	38.0777
APPARENT MACH NO.	0.6273	0.6462	0.6298	0.6059	0.5981	0.5862	0.5899	0.5905	0.6090

MEASURING PLANE

MACH NO.	0.6342	0.6536	0.6367	0.6122	0.6042	0.5921	0.5958	0.5964	0.6154
ABSOLUTE VELOCITY	742.9427	762.0684	740.2014	716.5313	697.4729	680.0926	682.8745	682.0169	704.3615
SWIRL VELOCITY	454.3908	434.8514	415.3788	470.9912	443.2872	450.3981	449.7634	458.5975	500.9655
WEIGHT FLOW	13.6874	9.8118	16.9395	24.4979	28.4907	20.9650	9.9954	4.3432	6.1856
AXIAL VELOCITY	585.6386	623.8056	611.0196	539.4297	538.4542	507.2297	507.3716	496.0349	485.1952

CALCULATING PLANE

SWIRL VELOCITY	451.3882	432.2318	413.4528	469.8195	443.6972	454.2599	456.2193	466.6030	512.6612
AXIAL VELOCITY	551.9280	588.4163	577.9335	517.9760	521.3927	488.5298	480.0666	467.5198	455.9010
ABSOLUTE VELOCITY	719.2524	734.8046	714.0108	700.3865	685.4806	669.6133	669.8049	670.4466	698.3102
MERIDIONAL VELOCITY	558.9632	593.2247	581.1170	518.4307	521.5071	490.9573	489.3858	480.4048	473.1075
ANGLE (DEG.)	39.2269	36.2535	35.5330	42.1540	40.3431	42.8598	43.4813	44.8825	48.2915
MACH NO.	0.6124	0.6283	0.6125	0.5974	0.5931	0.5823	0.5836	0.5856	0.6097
WEIGHT FLOW	13.6914	9.8208	16.9462	24.5126	28.5142	20.9972	9.9859	4.3451	6.1885
WHEEL SPEED	1360.0952	1327.2549	1294.4498	1206.7445	1082.5206	934.7440	838.5497	803.5953	771.5469
RELAT. TANG. VELOC.	908.7068	895.0231	880.9969	736.9248	638.8233	480.4841	382.3303	336.9923	258.8858
RELATIVE FLOW ANGLE	58.4037	56.4636	56.5908	54.8736	50.7735	44.3824	37.9986	35.0488	28.6877
RELATIVE VELOCITY	1066.8590	1073.7699	1055.3919	901.0151	824.6603	686.9526	621.0281	586.8155	539.3075
RELATIVE MACH NO.	0.9084	0.9182	0.9054	0.7686	0.7135	0.5974	0.5411	0.5125	0.4709
DEVIATION	2.4037	0.1636	0.6908	3.6736	3.7735	5.6824	10.0986	12.1488	10.0877
AIR TURNING ANGLE	8.0717	8.0421	6.7593	6.5169	7.7386	10.4815	14.2158	15.2424	20.1431
REL. MACH NO.(WHL.)	1.0666	1.0486	1.0289	0.9750	0.8922	0.7879	0.7173	0.6907	0.6666
IDEAL PRESS. RATIO	0.9568	0.9629	0.9714	0.9878	1.0041	1.0194	1.0382	1.0449	1.0541
ROTOR PRESS. RATIO	1.5904	1.6076	1.5976	1.5754	1.5410	1.4931	1.4639	1.4567	1.4732
ROTOR TEMP. RATIO	1.1904	1.1846	1.1727	1.1820	1.1475	1.1331	1.1289	1.1240	1.1310
ADIABATIC EFFY.	0.7422	0.7846	0.8276	0.7601	0.8900	0.9101	0.8997	0.9139	0.8922
POLYTR. EFFICIENCY	0.7584	0.7985	0.8385	0.7749	0.8965	0.9151	0.9049	0.9183	0.8979
TOTAL LOSS COEFF.	0.1929	0.1615	0.1264	0.1962	0.0865	0.0769	0.0991	0.0865	0.1225
SHOCK LOSS COEFF.	0.0255	0.0318	0.0398	0.0646	0.0359	0.0100	0.0005	-0.0011	-0.0035
PROFILE LOSS COEFF.	0.1673	0.1296	0.0865	0.1316	0.0505	0.0668	0.0936	0.0876	0.1260
TOTAL LOSS PARAM.	0.0308	0.0269	0.0208	0.0333	0.0158	0.0153	0.0210	0.0185	0.0274
PROFILE LOSS PARAM.	0.0267	0.0216	0.0142	0.0223	0.0092	0.0133	0.0209	0.0187	0.0282
ROTOR DIFFUS. FACT.	0.3816	0.3622	0.3594	0.4418	0.4435	0.4939	0.4994	0.5191	0.5596
STATIC PRESS.(ALT.)	17.9969	18.1107	18.2137	18.1884	17.8968	17.4860	17.1530	16.9901	16.7999
RADIUS RATIO	0.9775	0.9531	0.9287	0.8656	0.7759	0.6696	0.6000	0.5756	0.5534
STREAMLINE SLOPE	-9.1000	-7.3000	-6.0000	-2.4000	1.2000	5.7000	11.2000	13.3000	15.5000
SOLIDITY	1.6400	1.6580	1.6700	1.6940	1.7300	1.7680	1.8530	1.9100	1.9540
METAL CAMBER	6.2000	4.9000	4.6000	7.2000	9.1000	13.6000	20.5000	25.1000	29.3000

ROTOR INLET TRAVERSE PLANE   READING NUMBER 106   TIME 10H 32M 27S   UNIFORM INLET FLOW   STATOR ANGLE 3.

DISTORTION INDEX 0.000

SPEED (RPM)	11444.8720	
ACTUAL ORIFICE FLOW	137.9053	
THETA	0.9956	
DELTA	0.9929	
MASS AVERAGED PT	14.5927	(14.6960)
MASS AVERAGED TT	516.4110	(518.6881)
TOTAL WEIGHT FLOW	143.5846	(PROBE INTEGRATION)
EQUIV. WEIGHT FLOW	144.2828	
EQUIV. SPEED	11470.0767	
PERCENT SPEED	89.7431	

PROBE TYPE - NASA 4 PARAMETER   LOCATION - STA 5.5, 328 DEG.

IMMERSION(IN.)	0.4000	0.8400	1.2900	2.3600	3.8700	5.6100	6.9300	7.4300	7.9400
TOTAL PRESSURE	14.5728	14.6950	14.6830	14.6936	14.7323	14.7338	14.7103	14.7098	14.6557
STATIC PRESSURE	12.0365	11.7676	11.5245	11.2520	11.2785	11.4408	11.6911	11.9483	12.1418
WEDGE PRESSURE	12.2222	12.0340	11.8455	11.6521	11.6806	11.7964	11.9781	12.1776	12.3212
TOTAL TEMPERATURE	521.1118	520.2386	519.2939	519.0142	518.1962	517.7178	516.4998	517.5937	518.9184
ANGLE (DEG.)	1.7591	2.3295	1.9905	1.9020	1.3783	1.3957	1.7197	1.6494	2.0264
APPARENT MACH NO.	0.5075	0.5418	0.5623	0.5851	0.5854	0.5725	0.5497	0.5265	0.5040

PROBE TYPE - NASA 2 PARAMETER   LOCATION - STA 5.5, 260 DEG.

STATIC PRESSURE	12.3336	12.2551	12.0738	11.9404	11.9462	12.1117	12.3765	12.4257	12.4994
WEDGE PRESSURE	12.3624	12.2875	12.1095	11.9790	11.9853	12.1476	12.4069	12.4552	12.5267
ANGLE (DEG.)	1.3261	0.3295	0.5642	1.9365	2.7053	4.2545	6.2338	6.7756	6.7698
APPARENT MACH NO.	0.4904	0.5120	0.5318	0.5480	0.5509	0.5323	0.4991	0.4932	0.4788

MEASURING PLANE

MACH NO.	0.4939	0.5158	0.5360	0.5525	0.5554	0.5365	0.5028	0.4968	0.4822
ABSOLUTE VELOCITY	538.5754	561.2705	582.0488	598.8934	601.8905	582.5132	547.8133	541.5864	526.3097
SWIRL VELOCITY	16.0634	22.3159	19.9010	19.7762	14.4772	14.0948	15.9316	14.8803	17.4332
WEIGHT FLOW	13.5432	9.8032	16.5466	26.7382	30.0077	23.4012	11.2399	5.5407	6.9493
AXIAL VELOCITY	523.0196	548.5713	572.6048	595.5025	601.6834	578.4833	530.6154	516.7497	492.7092

CALCULATING PLANE

ANGLE (DEG.)	1.5892	2.0588	1.7817	1.7510	1.2693	1.2656	1.5017	1.3927	1.6750
SWIRL VELOCITY	16.3389	22.6277	20.1273	19.9387	14.4638	13.9402	15.5086	14.3425	16.6137
AXIAL VELOCITY	587.9231	628.4446	646.0435	651.2269	651.7407	629.9726	590.5421	588.9144	567.1208
MERIDONAL VELOCITY	601.0577	637.3702	652.0767	653.3313	651.7448	633.2143	603.0723	609.6889	599.7983
ABSOLUTE VELOCITY	602.3014	638.7860	653.3975	654.6401	652.9074	634.3756	604.2969	610.8960	601.0877
MACH NO.	0.5558	0.5918	0.6063	0.6075	0.6058	0.5874	0.5578	0.5642	0.5546
WEIGHT FLOW	13.3798	9.8039	16.5570	26.7593	30.0122	23.4082	11.1658	5.5418	6.9563
WHEEL SPEED	1397.0435	1359.2369	1319.4586	1217.7507	1078.5147	913.7044	793.4124	748.4859	702.4981
RELAT. TANG. VELOC.	1380.7042	1336.6092	1299.3311	1197.8120	1064.0509	899.7642	777.9037	734.1433	685.8843
RELATIVE FLOW ANGLE	66.4754	64.5058	63.3502	61.3905	58.5122	54.8640	52.2154	50.2913	48.8308
RELATIVE VELOCITY	1505.8597	1480.7984	1453.7760	1364.4028	1247.7878	1100.2435	984.2917	954.2990	911.1505
RELATIVE MACH NO.	1.3897	1.3719	1.3490	1.2663	1.1578	1.0188	0.9085	0.8814	0.8407
MCL INCIDENCE	4.2754	3.3058	2.8501	2.9905	2.4122	2.5640	3.8154	2.2913	0.9308
SURFACE INCIDENCE	2.0754	1.3058	0.7502	0.5905	0.0122	-0.1359	0.1154	-1.5086	-3.1691
RELATIVE TOTAL PRESS	38.6938	37.5005	35.7908	31.6171	27.4391	23.4431	21.1313	20.6037	19.8587
STATIC TEMPERATURE	490.7533	486.1473	483.6889	483.2927	482.7188	484.2563	486.2056	486.5706	488.8075
RELAT. TOTAL TEMP.	680.5206	669.3473	659.9473	638.4630	612.2962	584.9098	566.5759	562.2744	557.9945
STATIC PRESS.(ALT.)	11.8134	11.5939	11.4534	11.4505	11.4963	11.6637	11.9077	11.8504	11.8909
RADIUS RATIO	0.9736	0.9464	0.9179	0.8469	0.7495	0.6347	0.5505	0.5198	0.4885
STREAMLINE SLOPE	-12.0000	-9.6000	-7.8000	-4.6000	0.2000	5.8000	11.7000	15.0000	19.0000

STATOR INLET TRAVERSE PLANE READING NUMBER 106 TIME 10H 32M 27S UNIFORM INLET FLOW STATOR ANGLE 3.

MASS AVERAGED PT	22.5521	(22.7116)
MASS AVERAGED TT	598.5446	(601.1838)
TOTAL WEIGHT FLOW	135.0119	(PROBE INTEGRATION)
EQUIV. WEIGHT FLOW	135.6684	

MEASURING PLANE									
IMMERSION (IN.)	0.3100	0.6400	0.9600	1.8100	3.0200	4.4300	5.3600	5.6800	5.9500
TOTAL PRESSURE	23.1772	23.6249	23.4590	23.1496	22.7029	21.9991	21.6036	21.4291	21.5914
STATIC PRESSURE	17.6828	17.7355	17.8591	17.9775	17.7418	17.3554	16.9973	16.8485	16.7239
WEDGE PRESSURE	17.7818	17.8450	17.9604	18.0673	17.8268	17.4336	17.0754	16.9261	16.8089
TOTAL TEMPERATURE	620.3713	616.3204	608.9846	613.4795	594.6460	586.6537	583.0946	581.7969	586.9165
ANGLE (DEG.)	37.8076	34.8802	34.2084	41.1252	39.4633	41.6038	41.5537	42.7543	45.9163
MACH NO.	0.6342	0.6536	0.6367	0.6122	0.6042	0.5921	0.5958	0.5964	0.6154
ABSOLUTE VELOCITY	742.9426	762.0682	740.2015	716.5312	697.4729	680.0925	682.8743	682.0172	704.3614
SWIRL VELOCITY	454.3907	434.8512	415.3788	470.9910	443.2872	450.3979	449.7632	458.5976	500.9654
AXIAL VELOCITY	585.6385	623.8054	611.0199	539.4298	538.4542	507.2298	507.3714	496.0351	485.1951
WEIGHT FLOW	13.6874	9.8118	16.9395	24.4979	28.4907	20.9650	9.9954	4.3432	6.1856
CALCULATING PLANE									
ANGLE (DEG.)	37.9919	34.8484	33.8383	40.3364	37.9445	39.9540	39.8861	40.9917	44.0197
MACH NO.	0.6325	0.6551	0.6452	0.6244	0.6261	0.6081	0.6071	0.6068	0.6236
SWIRL VELOCITY	456.0761	436.1729	416.9975	472.1683	443.2872	447.0721	444.0038	452.4978	492.8451
AXIAL VELOCITY	582.9239	625.4425	621.0030	555.0458	567.5158	532.6681	530.2828	519.6894	509.0060
ABSOLUTE VELOCITY	741.1061	763.7125	749.2668	729.7586	720.9165	697.2386	694.8710	693.0542	713.1199
WEIGHT FLOW	13.6966	9.8175	16.9522	24.4999	28.5251	20.9757	10.0057	4.3492	6.1896
MERIDIONAL VELOCITY	583.1513	625.9040	621.5038	555.4189	567.5193	534.0348	533.5046	523.9362	514.3938
STATIC TEMPERATURE	574.5605	567.7439	562.2963	569.2244	551.4902	546.3127	543.1167	541.9419	544.6195
STATIC PRESS.(ALT.)	17.7074	17.7127	17.7346	17.8025	17.4339	17.1390	16.8481	16.7121	16.6133
MCL INCIDENCE	9.0067	5.5941	4.2456	9.3935	4.2947	5.8465	5.7384	6.8167	9.8756
SUC SUR INCIDENCE	2.5819	-0.9315	-2.3216	3.1464	-1.8154	-0.3559	-0.6738	0.3217	3.2696
RADIUS RATIO	0.9766	0.9534	0.9295	0.8694	0.7839	0.6868	0.6223	0.5991	0.5810
STREAMLINE SLOPE	-1.6000	-2.2000	-2.2999	-2.1000	-0.2000	4.0999	6.2999	7.2999	6.3000

STATOR INCIDENCE PLOTS (UNIFORM INLET FLOW)

RDG NO= 106 PCT DES SPD= 90.00 FAN INLET TOT TEMP= 518.688
OUTER WALL STATIC PRES= 18.750 HUB STATIC PRES= 18.600

PCT IM-MERSION	IN RADIUS	EX BL ANG	SOLIDITY	EX FLO ANG	INC ANG SS	IN VEL	IN TANG VELOCITY	IN STAT TEMP	IN STAT PRES	IN TOT PRES
.050	13.4800	-7.4000	1.0400	.5000	2.6000	741.0000	456.0000	574.6000	17.7100	23.1700
.100	13.1600	-7.5000	1.0600	6.7600	-.9000	763.7000	436.2000	567.7000	17.7100	23.6200
.150	12.8300	-7.6000	1.0900	5.4000	-2.3000	749.3000	417.0000	562.3000	17.7300	23.4600
.282	12.0000	-8.4000	1.1700	5.4000	3.1400	729.8000	472.2000	569.2200	17.8000	23.1500
.470	10.8200	-10.1000	1.3000	1.4000	-1.8000	721.0000	443.3000	551.5000	17.4300	22.7000
.689	9.4800	-9.8000	1.4700	1.4000	-.3600	797.2000	447.0000	546.3000	17.1400	22.0000
.850	8.5900	-9.2000	1.6200	2.1000	-.6800	694.9000	444.0000	543.1000	16.8500	21.6100
.900	8.2700	-9.1000	1.6700	2.0000	.3000	693.0000	452.5000	541.9000	16.7100	21.4300
.937	8.0200	-9.0000	1.7300	1.8700	3.2700	713.0000	492.8000	544.6000	16.6100	21.5900

PCT IMMERSION	EX RADIUS	EX TOT TEMP	EX TOT PRES
.0500	13.4700	614.4000	22.3200
.1000	13.1500	612.6700	23.1500
.1500	12.8400	607.0000	23.2800
.2822	11.9700	606.3400	22.8500
.4702	10.8300	592.0000	22.4300
.6887	9.5700	584.3500	21.9400
.8500	8.6700	581.7600	21.1100
.9000	8.4000	582.4000	21.0000
.9372	8.1200	586.0400	20.7200

PCT IMMERS	DIF FACT	LOSS COEF	LOSS PARAM	POLY EFF	DEV ANG	EX MACH NO	EX COR VEL	EX COR AX VELOCITY	EX COR TANG VELOCITY
.0500	.4835	.1557	.0748	.9489	4.9000	.5059	599.5606	599.5377	5.2321
.1000	.3611	.0795	.0373	1.0190	11.2600	.5583	657.2505	652.6812	77.3654
.1500	.3319	.0314	.0143	1.0921	10.0000	.5664	663.1511	660.2080	62.4080
.2822	.3698	.0561	.0239	2.3711	10.8000	.5426	636.4175	633.5931	59.8922
.4702	.3932	.0512	.0197	1.0645	8.5000	.5183	602.2521	602.0723	14.7143
.6887	.4753	.0123	.0042	1.1542	8.2000	.4879	564.8823	564.7137	13.8013
.8500	.4743	.1050	.0324	.8674	8.3000	.4272	496.0832	495.7500	18.1783
.9000	.4841	.0911	.0273	.8196	8.1000	.4187	486.8153	486.5187	16.9896
.9372	.5450	.1747	.0505	.7614	7.8700	.3950	461.5949	461.3490	15.0627

PCT IMMERS	EX STAT PRES
.0500	18.7416
.1000	18.7336
.1500	18.7258
.2822	18.7039
.4702	18.6753
.6887	18.6436
.8500	18.6210
.9000	18.6142
.9372	18.6072

ROTOR INLET TRAVERSE PLANE   READING NUMBER   118   TIME   15H 27M 37S   UNIFORM INLET FLOW   STATOR ANGLE 3.

DISTORTION INDEX   0.000

SPEED (RPM)	12087.2007	
ACTUAL ORIFICE FLOW	144.0143	
THETA	0.9976	
DELTA	0.9913	
MASS AVERAGED PT	14.5694	(14.6960)
MASS AVERAGED TT	517.4794	(518.6881)
TOTAL WEIGHT FLOW	149.5953	(PROBE INTEGRATION)
EQUIV. WEIGHT FLOW	150.7191	
EQUIV. SPEED	12101.3090	
PERCENT SPEED	94.6820	

PROBE TYPE - NASA 4 PARAMETER		LOCATION - STA 5.5, 328 DEG.							
IMMERSION(IN.)	0.4000	0.8400	1.2900	2.3600	3.8700	5.6100	6.9300	7.4300	7.9400
TOTAL PRESSURE	14.5815	14.6711	14.6794	14.7010	14.7404	14.7310	14.7083	14.7077	14.6398
STATIC PRESSURE	11.5075	11.2515	11.0489	10.6894	10.8771	11.1763	11.3696	11.6423	11.8433
WEDGE PRESSURE	11.8113	11.6461	11.5067	11.2689	11.4057	11.6086	11.7392	11.9403	12.0820
TOTAL TEMPERATURE	519.6574	519.4416	519.4601	518.7818	518.6908	517.9098	517.7921	517.8793	518.2607
ANGLE (DEG.)	1.3757	2.3240	2.3879	2.7703	2.0802	1.6298	1.8174	1.8124	1.9711
APPARENT MACH NO.	0.5569	0.5838	0.6001	0.6280	0.6164	0.5933	0.5767	0.5538	0.5309
PROBE TYPE - NASA 2 PARAMETER		LOCATION - STA 5.5, 260 DEG.							
STATIC PRESSURE	11.9874	11.9644	11.8026	11.6525	11.6050	11.7608	12.0298	12.0947	12.2042
WEDGE PRESSURE	12.0229	12.0020	11.8437	11.6971	11.6514	11.8037	12.0658	12.1305	12.2366
ANGLE (DEG.)	6.5590	2.6482	2.7945	4.3653	6.5772	6.2460	7.4555	7.2448	7.1318
APPARENT MACH NO.	0.5322	0.5432	0.5622	0.5807	0.5893	0.5714	0.5392	0.5318	0.5125
MEASURING PLANE									
MACH NO.	0.5364	0.5476	0.5669	0.5858	0.5945	0.5763	0.5435	0.5359	0.5164
ABSOLUTE VELOCITY	582.4062	593.9100	613.5946	632.7107	641.5409	623.1316	589.7643	581.9769	561.8623
SWIRL VELOCITY	13.5855	23.5585	25.1659	30.4243	23.2859	17.6056	18.1255	17.5696	18.1031
WEIGHT FLOW	14.3379	10.1732	17.1092	27.6801	31.2256	24.4399	11.8106	5.8226	7.2766
AXIAL VELOCITY	565.6823	580.4746	603.4835	628.7436	641.0830	618.7547	571.2209	555.2448	526.0078
CALCULATING PLANE									
ANGLE (DEG.)	1.2064	2.0349	2.1208	2.5464	1.9316	1.4683	1.5565	1.5151	1.6201
SWIRL VELOCITY	13.8186	23.8876	25.4521	30.6743	23.2642	17.4125	17.6443	16.9345	17.2521
AXIAL VELOCITY	655.1528	671.2958	686.2903	688.7408	688.8014	678.2994	648.3155	639.2434	608.9608
MERIDONAL VELOCITY	669.7892	680.8300	692.6993	690.9666	688.8056	681.7896	662.0716	661.7934	644.0492
ABSOLUTE VELOCITY	670.9539	682.2631	694.1756	692.6503	690.1988	683.0185	663.3293	663.0469	645.3391
MACH NO.	0.6238	0.6352	0.6472	0.6457	0.6432	0.6360	0.6152	0.6159	0.5983
WEIGHT FLOW	14.3492	10.1795	17.1216	27.6256	30.9572	24.4407	11.8216	5.8277	7.2719
WHEEL SPEED	1475.9874	1435.1390	1391.8491	1285.0548	1137.3260	963.8097	836.0310	789.4595	741.6286
RELAT. TANG. VELOC.	1462.1685	1411.2512	1366.3971	1254.3804	1114.0617	946.3971	818.3855	772.5250	724.3764
RELATIVE FLOW ANGLE	65.3887	64.2461	63.1173	61.1523	58.2724	54.2310	51.0274	49.4147	48.3596
RELATIVE VELOCITY	1608.2765	1566.8946	1531.9505	1432.0979	1309.8038	1166.4064	1052.6606	1017.2341	969.2886
RELATIVE MACH NO.	1.4954	1.4589	1.4284	1.3350	1.2206	1.0861	0.9779	0.9450	0.8986
MCL INCIDENCE	3.1887	3.0461	2.6173	2.7523	2.1724	1.9310	2.6274	1.4147	0.4596
SURFACE INCIDENCE	0.9887	1.0461	0.5173	0.3523	-0.2275	-0.7689	-1.0725	-2.3852	-3.6403
RELATIVE TOTAL PRESS	43.7250	41.4043	39.1054	33.8793	28.9200	24.6877	22.2006	21.5004	20.6139
STATIC TEMPERATURE	482.0886	480.6115	479.2607	478.8105	479.0087	479.1069	481.2023	481.3146	483.5976
RELAT. TOTAL TEMP.	697.9448	685.4186	675.0413	649.6804	621.9169	592.2684	573.3436	567.3773	561.7957
STATIC PRESS.(ALT.)	11.2156	11.1803	11.0757	11.1063	11.1591	11.2189	11.3830	11.3850	11.4920
RADIUS RATIO	0.9736	0.9464	0.9179	0.8469	0.7495	0.6347	0.5505	0.5198	0.4385
STREAMLINE SLOPE	-12.0000	-9.6000	-7.8000	-4.6000	0.2000	5.8000	11.7000	15.0000	19.0000

ROTOR EXIT TRAVERSE PLANE   READING NUMBER 118   TIME 15H 27M 37S   UNIFORM INLET FLOW   STATOR ANGLE 3.00

MASS AVERAGED PT	23.8900	(24.0976)
MASS AVERAGED TT	611.5923	(613.0209)
TOTAL WEIGHT FLOW	141.9837	(PROBE INTEGRATION)
CORR. TOTAL FLOW	143.0503	

PROBE TYPE - NASA 4 PARAMETER   LOCATION - STA 9.0, 104 DEG.

IMMERSION (IN.)	0.3100	0.6400	0.9600	1.8100	3.0200	4.4300	5.3600	5.6800	5.9500
TOTAL PRESSURE	24.9530	25.2622	25.1171	24.7194	23.9885	23.0506	22.5035	22.3450	22.3486
STATIC PRESSURE	18.2157	17.9161	17.6862	17.3694	17.1116	16.6829	16.4815	16.4821	16.3482
WEDGE PRESSURE	19.2147	19.0748	18.8635	18.5354	18.1874	17.6463	17.3679	17.3287	17.2329
TOTAL TEMPERATURE	636.1062	628.6753	620.0819	625.9361	606.9301	596.6213	590.5474	590.8166	593.5882
ANGLE (DEG.)	38.8891	36.2207	35.1232	42.1968	40.9501	43.1499	43.8544	45.3769	46.9995
APPARENT MACH NO.	0.6229	0.6467	0.6531	0.6550	0.6417	0.6299	0.6201	0.6139	0.6210

PROBE TYPE - NASA 2 PARAMETER   LOCATION - STA 9.0, 300 DEG.

STATIC PRESSURE	18.4381	18.1430	18.1238	18.6375	18.4070	17.8822	17.5444	17.3519	17.2559
WEDGE PRESSURE	18.5628	18.2860	18.2632	18.7496	18.5064	17.9721	17.6299	17.4386	17.3454
ANGLE (DEG.)	40.7944	34.2033	32.4197	30.1740	32.4573	34.4623	36.4741	36.8053	37.3823
APPARENT MACH NO.	0.6644	0.6958	0.6906	0.6413	0.6204	0.6071	0.6013	0.6059	0.6129

MEASURING PLANE

MACH NO.	0.6723	0.7046	0.6993	0.6485	0.6271	0.6135	0.6075	0.6122	0.6193
ABSOLUTE VELOCITY	794.8794	825.0568	813.8059	763.4929	728.9971	708.7497	698.8503	703.9915	713.0115
SWIRL VELOCITY	497.9288	486.4990	467.3689	512.5313	477.7699	483.5279	480.9848	496.7039	516.5092
WEIGHT FLOW	14.7461	10.5738	18.5942	26.2302	29.7023	21.6499	10.0633	4.3580	6.2498
AXIAL VELOCITY	617.3323	664.2149	664.4288	565.3085	550.5805	515.8100	500.6152	490.2138	481.6642

CALCULATING PLANE

SWIRL VELOCITY	494.6384	483.5682	465.2018	511.2563	478.2118	487.6738	487.8889	505.3746	528.5677
AXIAL VELOCITY	581.1355	624.2752	626.2650	542.5837	532.6198	488.9367	474.9638	462.9004	452.7143
ABSOLUTE VELOCITY	769.5734	794.4959	783.7224	746.5831	716.6329	693.0057	688.0850	694.7189	707.8658
MERIDIONAL VELOCITY	588.5430	629.3767	629.7145	543.0601	532.7365	491.3662	484.1850	475.6580	469.8006
ANGLE (DEG.)	40.3545	37.7173	36.5620	43.2447	41.8657	44.8674	45.7088	47.4501	49.3578
MACH NO.	0.6490	0.6761	0.6711	0.6330	0.6156	0.5988	0.5975	0.6035	0.6145
WEIGHT FLOW	14.7549	10.5763	18.6018	26.2544	29.7084	21.4021	10.0704	4.3635	6.2516
WHEEL SPEED	1436.9512	1401.3715	1365.4687	1273.4402	1141.5504	986.0028	883.5928	847.5857	814.5239
RELAT. TANG. VELOC.	942.3127	917.8031	900.2667	762.1836	663.3383	498.3289	395.7038	342.2111	285.9562
RELATIVE FLOW ANGLE	58.0124	55.5601	55.0283	54.5301	51.2317	45.4032	39.2578	35.7331	31.3279
RELATIVE VELOCITY	1111.0066	1112.8690	1098.6449	935.8620	850.7794	699.8374	625.3131	585.9685	549.9849
RELATIVE MACH NO.	0.9370	0.9470	0.9407	0.7935	0.7309	0.6047	0.5429	0.5091	0.4774
DEVIATION	2.0124	-0.7398	-0.8716	3.3301	4.2317	6.7032	11.3578	12.8331	12.7279
AIR TURNING ANGLE	7.3762	8.6860	8.0889	6.6222	7.0406	8.8277	11.7696	13.6815	17.0316
REL. MACH NO.(WHL.)	1.1114	1.0934	1.0735	1.0199	0.9341	0.8261	0.7523	0.7255	0.7009
IDEAL PRESS. RATIO	0.9532	0.9598	0.9689	0.9867	1.0045	1.0214	1.0421	1.0496	1.0600
ROTOR PRESS. RATIO	1.7112	1.7219	1.7110	1.6814	1.6273	1.5647	1.5303	1.5192	1.5265
ROTOR TEMP. RATIO	1.2240	1.2102	1.1937	1.2065	1.1701	1.1519	1.1405	1.1408	1.1453
ADIABATIC EFFY.	0.7376	0.7961	0.8538	0.7725	0.8756	0.8964	0.9186	0.8999	0.8825
POLYTR. EFFICIENCY	0.7565	0.8110	0.8644	0.7884	0.8838	0.9027	0.9233	0.9056	0.8893
TOTAL LOSS COEFF.	0.2084	0.1605	0.1121	0.1957	0.1039	0.0918	0.0739	0.1022	0.1332
SHOCK LOSS COEFF.	0.0113	0.0118	0.0163	0.0453	0.0529	0.0205	0.0055	0.0027	-0.0000
PROFILE LOSS COEFF.	0.1971	0.1486	0.0958	0.1504	0.0510	0.0712	0.0733	0.0995	0.1333
TOTAL LOSS PARAM.	0.0336	0.0273	0.0192	0.0335	0.0188	0.0180	0.0164	0.0217	0.0291
PROFILE LOSS PARAM.	0.0318	0.0253	0.0164	0.0257	0.0092	0.0139	0.0152	0.0211	0.0291
ROTOR DIFFUS. FACT.	0.4018	0.3819	0.3731	0.4519	0.4568	0.5191	0.5350	0.5594	0.5793
STATIC PRESS.(ALT.)	18.8058	18.6051	18.5776	18.8787	18.5779	18.0899	17.6833	17.4713	17.3226
RADIUS RATIO	0.9775	0.9531	0.9287	0.8656	0.7759	0.6696	0.6000	0.5756	0.5534
STREAMLINE SLOPE	-9.1000	-7.3000	-6.0000	-2.4000	1.2000	5.7000	11.2000	13.3000	15.5000
SOLIDITY	1.6400	1.6580	1.6700	1.6940	1.7300	1.7880	1.8580	1.9100	1.9540
METAL CAMBER	6.2000	4.9000	4.6000	7.2000	9.1000	13.6000	20.5000	25.1000	29.3000

STATOR INLET TRAVERSE PLANE   READING NUMBER 118   TIME 15H 27M 37S   UNIFORM INLET FLOW   STATOR ANGLE 3.

MASS AVERAGED PT	23.8880	(24.0955)
MASS AVERAGED TT	611.5583	(612.9867)
TOTAL WEIGHT FLOW	142.2862	(PROBE INTEGRATION)
EQUIV. WEIGHT FLOW	143.3551	

MEASURING PLANE									
IMMERSION (IN.)	0.3100	0.6400	0.9600	1.8100	3.0200	4.4300	5.3600	5.6800	5.9500
TOTAL PRESSURE	24.9530	25.2622	25.1171	24.7194	23.9885	23.0506	22.5035	22.3450	22.3486
STATIC PRESSURE	18.4381	18.1430	18.1238	18.6375	18.4070	17.8822	17.5444	17.3519	17.2559
WEDGE PRESSURE	18.5628	18.2860	18.2632	18.7496	18.5064	17.9721	17.6299	17.4386	17.3454
TOTAL TEMPERATURE	636.1061	628.6751	620.0818	625.9360	606.9299	596.6211	590.5473	590.8165	593.5880
ANGLE (DEG.)	38.8891	36.2207	35.1232	42.1968	40.9501	43.1499	43.8544	45.3769	46.9994
MACH NO.	0.6723	0.7046	0.6993	0.6485	0.6271	0.6135	0.6075	0.6122	0.6193
ABSOLUTE VELOCITY	794.8793	825.0567	813.8059	763.4932	728.9972	708.7496	698.8502	703.9917	713.0115
SWIRL VELOCITY	497.9286	486.4988	467.3688	512.5314	477.7699	483.5278	480.9846	496.7041	516.5091
AXIAL VELOCITY	617.3323	664.2150	664.4290	565.3090	550.5808	515.8100	500.6152	490.2140	481.6642
WEIGHT FLOW	14.7461	10.5738	18.5942	26.2302	29.7023	21.6499	10.0633	4.3580	6.2498
CALCULATING PLANE									
ANGLE (DEG.)	39.0924	36.1773	34.7124	41.3601	39.3986	41.4714	42.1781	43.6365	45.1323
MACH NO.	0.6703	0.7065	0.7093	0.6618	0.6492	0.6293	0.6175	0.6209	0.6266
SWIRL VELOCITY	499.7754	487.9775	469.1902	513.8126	477.7659	479.9574	474.8254	490.0974	508.1367
AXIAL VELOCITY	614.1432	666.2937	676.2861	582.6268	580.6756	542.0385	523.0615	512.9980	504.7965
ABSOLUTE VELOCITY	792.7624	827.0796	824.3763	777.8706	752.7390	725.7872	709.5414	713.2508	720.7491
WEIGHT FLOW	14.7499	10.5812	18.6072	26.2464	29.7403	21.6701	10.0759	4.3628	6.2511
MERIDIONAL VELOCITY	614.3827	666.7851	676.8314	583.0183	580.6792	543.4292	526.2394	517.1900	510.1397
STATIC TEMPERATURE	583.8770	571.8289	563.5805	575.7100	559.8607	552.9090	548.7712	548.5958	550.4470
STATIC PRESS.(ALT.)	18.4692	18.1121	17.9623	18.4300	18.0740	17.6542	17.4051	17.2317	17.1550
MCL INCIDENCE	10.1076	6.9240	5.1203	10.4179	5.7489	7.3678	8.0444	9.4830	11.0000
SUC SUR INCIDENCE	3.6824	0.3973	-1.4475	4.1701	-0.3613	1.1614	1.6181	2.9665	4.3823
RADIUS RATIO	0.9766	0.9534	0.9295	0.8694	0.7839	0.6868	0.6223	0.5991	0.5810
STREAMLINE SLOPE	-1.6000	-2.2000	-2.2999	-2.1000	-0.2000	4.0999	6.2999	7.2999	8.3000

STATOR INCIDENCE PLOTS (UNIFORM INLET FLOW)

RDG NO= 118 PCT DES SPD= 95.00 FAN INLET TOT TEMP= 518.688
OUTER WALL STATIC PRES= 19.480 HUB STATIC PRES= 19.280

PCT IM-MERSION	IN RADIUS	EX BL ANG	SOLIDITY	EX FLO ANG	INC ANG SS	IN VEL	IN TANG VELOCITY	IN STAT TEMP	IN STAT PRES	IN TOT PRES
.050	13.4800	-7.4000	1.0400	5.9900	3.7000	792.8000	499.8000	583.9000	18.4700	24.9500
.100	13.1600	-7.5000	1.0600	7.9200	.4000	827.1000	487.9800	571.8000	18.1100	25.2600
.150	12.8300	-7.6000	1.0900	6.0600	-1.4400	824.4000	469.2000	563.6000	17.9600	25.1200
.282	12.0000	-8.4000	1.1700	6.1100	4.1700	777.9000	513.8000	575.7000	18.4300	24.7200
.470	10.8200	-10.1000	1.3000	5.0200	-.4000	752.7000	477.8000	559.9000	18.0700	24.0000
.689	9.4800	-9.8000	1.4700	2.9000	1.1600	725.8000	479.9000	552.9000	17.6500	23.0500
.850	8.5900	-9.2000	1.6200	2.1000	1.6100	709.5000	474.8000	548.8000	17.4100	22.5100
.900	8.2700	-9.1000	1.6700	5.2100	2.9700	713.2000	490.1000	548.6000	17.2300	22.3400
.937	8.0200	-9.0000	1.7300	3.5200	4.3800	720.7000	508.1000	550.4000	17.1500	22.3500

PCT IMMERSION	EX RADIUS	EX TOT TEMP	EX TOT PRES
.0500	13.4700	625.4300	23.6600
.1000	13.1500	620.8400	24.5500
.1500	12.8400	613.6400	24.3200
.2822	11.9700	611.7900	24.1900
.4702	10.8300	601.8700	23.7000
.6887	9.5700	592.2000	22.9700
.8500	8.6700	588.3300	22.0200
.9000	8.4000	589.6000	21.4300
.9372	8.1200	593.0000	21.0300

PCT IMMERS	DIF FACT	LOSS COEF	LOSS PARAM	POLY EFF	DEV ANG	EX MACH NO	EX COR VEL	EX COR AX VELOCITY	EX COR TANG VELOCITY
.0500	.4580	.1991	.0952	1.1572	10.3900	.5352	638.0697	634.5859	66.5857
.1000	.3870	.0993	.0464	1.2926	12.4200	.5860	692.3024	685.6988	95.3925
.1500	.4020	.1117	.0510	1.0732	10.6600	.5743	675.4269	671.6526	71.3047
.2822	.3839	.0843	.0358	-7.5714	11.5100	.5691	668.7439	664.9450	71.1795
.4702	.3712	.0506	.0194	1.3521	12.1200	.5439	635.5991	633.1611	55.6171
.6887	.4049	.0148	.0050	1.3388	9.7000	.5020	584.2973	583.5490	29.5613
.8500	.4780	.0961	.0296	.9238	8.3000	.4374	510.4014	510.0586	18.7030
.9000	.5458	.1781	.0531	.7687	11.3100	.3897	456.9958	455.1078	41.4981
.9372	.6139	.2538	.0732	.6736	9.5200	.3535	416.7640	415.9777	25.5880

PCT IMMERS	EX STAT PRES
.0500	19.4688
.1000	19.4581
.1500	19.4477
.2822	19.4186
.4702	19.3804
.6887	19.3381
.8500	19.3080
.9000	19.2989
.9372	19.2896

ROTOR INLET TRAVERSE PLANE   READING NUMBER 128   TIME 9H 26M 50S   UNIFORM INLET FLOW   STATOR ANGLE 3.

DISTORTION INDEX 0.000

SPEED (RPM)	12755.9901	
ACTUAL ORIFICE FLOW	152.7661	
THETA	0.9935	
DELTA	0.9922	
MASS AVERAGED PT	14.5826	(14.6960)
MASS AVERAGED TT	515.3284	(518.6881)
TOTAL WEIGHT FLOW	157.5906	(PROBE INTEGRATION)
EQUIV. WEIGHT FLOW	158.3004	
EQUIV. SPEED	12797.5019	
PERCENT SPEED	100.1291	

PROBE TYPE - NASA 4 PARAMETER   LOCATION - STA 5.5, 328 DEG.

IMMERSION(IN.)	0.4000	0.8400	1.2900	2.3600	3.8700	5.6100	6.9300	7.4300	7.9400
TOTAL PRESSURE	14.5549	14.6933	14.7074	14.7325	14.7271	14.7159	14.6934	14.7024	14.6078
STATIC PRESSURE	10.8403	10.6564	10.4758	10.0848	10.2931	10.6765	10.7813	11.0226	11.2683
WEDGE PRESSURE	11.3301	11.2448	11.1373	10.9205	11.0372	11.2645	11.3295	11.4946	11.6421
TOTAL TEMPERATURE	519.5878	520.2177	519.4173	519.2085	518.9961	517.4174	517.6327	517.2146	516.8844
ANGLE (DEG.)	1.0721	2.3139	2.2010	2.2474	1.9402	1.9180	1.7277	1.7099	1.5498
APPARENT MACH NO.	0.6089	0.6300	0.6428	0.6681	0.6552	0.6297	0.6212	0.6034	0.5786

PROBE TYPE - NASA 2 PARAMETER   LOCATION - STA 5.5, 260 DEG.

STATIC PRESSURE	11.5105	11.4968	11.3708	11.2834	11.2506	11.3676	11.5694	11.7101	11.8108
WEDGE PRESSURE	11.5552	11.5445	11.4217	11.3368	11.3047	11.4187	11.6157	11.7535	11.8503
ANGLE (DEG.)	1.0597	2.2270	2.6630	3.1502	4.0004	4.9863	6.3001	6.4064	6.2121
APPARENT MACH NO.	0.5836	0.5971	0.6119	0.6233	0.6263	0.6129	0.5896	0.5745	0.5548

MEASURING PLANE

MACH NO.	0.5887	0.6024	0.6175	0.6291	0.6322	0.6185	0.5948	0.5794	0.5594
ABSOLUTE VELOCITY	635.6959	649.4790	664.5840	676.1986	679.2808	665.6563	641.8251	626.3021	605.9285
SWIRL VELOCITY	11.5568	25.6506	25.1252	26.3816	22.9976	22.1318	18.7526	17.8390	15.3511
WEIGHT FLOW	15.2429	10.8419	18.1113	29.0144	32.4201	25.5586	12.5375	6.1451	7.6958
AXIAL VELOCITY	617.5079	634.7909	653.7157	672.2250	678.8539	660.8794	621.6731	597.5637	567.3746

CALCULATING PLANE

ANGLE (DEG.)	0.9228	1.9852	1.9227	2.0336	1.7589	1.7121	1.4603	1.4228	1.2539
SWIRL VELOCITY	11.7551	26.0090	25.4109	26.5984	22.9762	21.8891	18.2547	17.1943	14.6294
AXIAL VELOCITY	728.7344	749.3304	755.9228	748.0527	747.2028	731.2657	715.0451	691.2217	667.3223
MERIDONAL VELOCITY	745.0147	759.9730	762.9822	750.4699	747.2073	735.0284	730.2170	715.6053	705.7736
ABSOLUTE VELOCITY	746.1320	761.4333	764.4165	751.9464	748.5628	736.3633	731.4702	716.8514	706.9878
MACH NO.	0.7002	0.7160	0.7191	0.7062	0.7027	0.6902	0.6851	0.6702	0.6602
WEIGHT FLOW	15.2524	10.8472	18.1171	29.0338	32.4252	25.5525	12.5394	6.1209	7.7018
WHEEL SPEED	1561.0063	1516.5711	1471.9840	1358.4261	1202.4030	1019.7429	884.2643	835.4137	785.3383
RELAT. TANG. VELOC.	1549.2512	1490.5622	1446.5728	1331.8275	1179.4266	997.8537	866.0094	818.2193	770.7086
RELATIVE FLOW ANGLE	64.3179	62.9851	62.1912	60.5994	57.6445	53.6245	49.8626	48.8276	47.5184
RELATIVE VELOCITY	1719.0767	1673.1208	1635.4554	1528.7148	1396.1966	1239.3457	1132.7792	1087.0019	1045.0398
RELATIVE MACH NO.	1.6134	1.5734	1.5386	1.4358	1.3107	1.1616	1.0611	1.0163	0.9759
MCL INCIDENCE	2.1179	1.7851	1.6912	2.1994	1.5445	1.3245	1.4626	0.8276	-0.3815
SURFACE INCIDENCE	-0.0820	-0.2148	-0.4087	-0.2005	-0.8554	-1.3755	-2.2373	-2.9723	-4.4816
RELATIVE TOTAL PRESS	49.9164	46.9973	44.1678	37.7835	31.6407	26.2385	23.5561	22.5992	21.7459
STATIC TEMPERATURE	473.1318	471.7790	470.6724	472.0599	472.2896	472.3566	473.1504	474.5266	475.3893
RELAT. TOTAL TEMP.	719.7354	705.6536	693.7961	666.9317	634.7748	600.0003	579.8304	572.6804	566.0540
STATIC PRESS.(ALT.)	10.4895	10.4394	10.4200	10.5606	10.5899	10.7006	10.7352	10.8784	10.9017
RADIUS RATIO	0.9736	0.9464	0.9179	0.8469	0.7495	0.6347	0.5505	0.5198	0.4885
STREAMLINE SLOPE	-12.0000	-9.6000	-7.8000	-4.6000	0.2000	5.8000	11.7000	15.0000	19.0000

ROTOR EXIT TRAVERSE PLANE READING NUMBER 128 TIME 9H 26M 50S UNIFORM INLET FLOW STATOR ANGLE 3.00

MASS AVERAGED PT	22.5272	(22.7023)
MASS AVERAGED TT	597.4841	(601.3793)
TOTAL WEIGHT FLOW	155.7481	(PROBE INTEGRATION)
CORR. TOTAL FLOW	156.4496	

PROBE TYPE - NASA 4 PARAMETER LOCATION - STA 9.0, 104 DEG.

IMMERSION (IN.)	0.3100	0.6400	0.9600	1.8100	3.0200	4.4300	5.3600	5.6800	5.9500
TOTAL PRESSURE	23.5112	23.1981	23.0822	22.0953	22.1088	23.1709	22.7276	22.3282	22.2889
STATIC PRESSURE	16.2465	15.9608	15.7513	15.5650	15.7165	16.0152	15.7165	15.4792	15.4668
WEDGE PRESSURE	17.3991	17.1123	16.9239	16.5879	16.7117	17.1502	16.8282	16.5634	16.5460
TOTAL TEMPERATURE	613.3773	603.7144	601.6621	610.4101	597.5564	596.5741	592.0078	592.1520	592.5303
ANGLE (DEG.)	26.9306	25.4184	27.0726	34.7721	34.6042	35.4861	35.9186	37.2487	40.6881
APPARENT MACH NO.	0.6704	0.6740	0.6810	0.6535	0.6453	0.6701	0.6696	0.6675	0.6666

PROBE TYPE - NASA 2 PARAMETER LOCATION - STA 9.0, 300 DEG.

STATIC PRESSURE	16.2806	16.1139	16.5559	16.6982	16.6621	16.6131	16.2153	16.0774	15.8915
WEDGE PRESSURE	16.4342	16.2637	16.6872	16.7972	16.7626	16.7451	16.3434	16.2024	16.0215
ANGLE (DEG.)	13.6774	18.0058	17.4708	25.5212	32.6972	31.5316	31.8257	31.9188	32.2475
APPARENT MACH NO.	0.7342	0.7309	0.6970	0.6384	0.6416	0.6974	0.7026	0.6928	0.7034

MEASURING PLANE

MACH NO.	0.7442	0.7409	0.7059	0.6456	0.6488	0.7063	0.7116	0.7015	0.7124
ABSOLUTE VELOCITY	856.3588	845.6391	808.6368	750.6248	746.3500	807.2081	809.5152	799.4248	811.3029
SWIRL VELOCITY	386.7258	362.0140	367.2416	427.7935	423.8390	467.1537	470.9438	478.4892	522.7365
WEIGHT FLOW	17.0141	11.3670	19.0204	26.3399	30.7273	26.2003	12.3929	5.2968	7.4580
AXIAL VELOCITY	761.2714	761.7710	718.5004	616.1555	614.2944	655.2643	650.1403	629.2776	607.9948

CALCULATING PLANE

SWIRL VELOCITY	384.1703	359.8332	365.5388	426.7293	424.2311	471.1592	477.7038	486.8419	534.9405
AXIAL VELOCITY	707.6844	709.2594	673.7139	589.6181	589.7386	626.7992	610.6003	588.7442	568.8320
ABSOLUTE VELOCITY	814.0692	801.3922	770.6423	729.0702	727.3930	787.4357	785.4456	777.3377	797.4012
MERIDIONAL VELOCITY	716.7049	715.0554	677.4248	590.1357	589.8681	629.9137	622.4548	604.9699	590.3008
ANGLE (DEG.)	28.4616	26.8678	28.4474	35.8486	35.6835	36.8879	37.9923	39.5400	43.1909
MACH NO.	0.7038	0.6982	0.6696	0.6256	0.6310	0.6873	0.6834	0.6803	0.6990
WEIGHT FLOW	17.0165	11.3723	19.0236	26.3493	30.6147	26.2246	12.3836	5.2970	7.4663
WHEEL SPEED	1519.7219	1480.8873	1444.0846	1346.1483	1206.8690	1043.2241	934.5701	896.9235	862.5297
RELAT. TANG. VELOC.	1135.5514	1121.0541	1078.5457	919.4189	782.6377	572.0647	456.8653	410.0816	327.5891
RELATIVE FLOW ANGLE	57.7420	57.4687	57.8676	57.3055	52.9951	42.2447	36.2778	34.1316	29.0283
RELATIVE VELOCITY	1342.8117	1329.6867	1273.6424	1092.5157	980.0335	850.9106	772.1247	730.8594	675.1071
RELATIVE MACH NO.	1.1609	1.1585	1.1067	0.9374	0.8502	0.7427	0.6758	0.6396	0.5918
DEVIATION	1.7420	1.1687	1.9676	6.1055	5.9951	3.5447	8.3778	11.2316	10.4283
AIR TURNING ANGLE	6.5758	5.5163	4.3235	3.2938	4.6493	11.3797	13.5848	14.6959	18.4900
REL. MACH NO.(WHL.)	1.1571	1.1393	1.1195	1.0643	0.9777	0.8680	0.7911	0.7637	0.7384
IDEAL PRESS. RATIO	0.9493	0.9564	0.9662	0.9855	1.0049	1.0236	1.0456	1.0551	1.0667
ROTOR PRESS. RATIO	1.6153	1.5788	1.5694	1.4997	1.5012	1.5745	1.5462	1.5186	1.5258
ROTOR TEMP. RATIO	1.1805	1.1605	1.1583	1.1756	1.1513	1.1529	1.1436	1.1448	1.1463
ADIABATIC EFFY.	0.8116	0.8667	0.8664	0.6974	0.8118	0.9038	0.9216	0.8739	0.8755
POLYTR. EFFICIENCY	0.8238	0.8750	0.8746	0.7141	0.8223	0.9098	0.9253	0.8811	0.8827
TOTAL LOSS COEFF.	0.1202	0.0799	0.0813	0.2104	0.1310	0.0794	0.0700	0.1199	0.1274
SHOCK LOSS COEFF.	0.0141	0.0132	0.0123	0.0148	0.0547	0.0369	0.0161	0.0097	0.0053
PROFILE LOSS COEFF.	0.1060	0.0666	0.0690	0.1956	0.0762	0.0425	0.0539	0.1102	0.1220
TOTAL LOSS PARAM.	0.0195	0.0129	0.0129	0.0335	0.0227	0.0164	0.0152	0.0259	0.0285
PROFILE LOSS PARAM.	0.0172	0.0108	0.0110	0.0311	0.0132	0.0088	0.0116	0.0238	0.0273
ROTOR DIFFUS. FACT.	0.2877	0.2706	0.2893	0.3690	0.3878	0.4235	0.4374	0.4516	0.4936
STATIC PRESS.(ALT.)	16.8964	16.7534	17.0916	16.9754	16.9096	16.8954	16.5554	16.3811	16.0841
RADIUS RATIO	0.9775	0.9531	0.9287	0.8656	0.7759	0.6696	0.6000	0.5756	0.5534
STREAMLINE SLOPE	-9.1000	-7.3000	-6.0000	-2.4000	1.2000	5.7000	11.2000	13.3000	15.5000
SOLIDITY	1.6400	1.6580	1.6700	1.6940	1.7300	1.7880	1.8530	1.9100	1.9540
METAL CAMBER	6.2000	4.9000	4.6000	7.2000	9.1000	13.6000	20.5000	25.1000	29.3000

STATOR INLET TRAVERSE PLANE   READING NUMBER 128   TIME 9H 26M 50S   UNIFORM INLET FLOW   STATOR ANGLE 3.

MASS AVERAGED PT	22.5264	(22.7015)
MASS AVERAGED TT	597.4860	(601.3813)
TOTAL WEIGHT FLOW	155.7495	(PROBE INTEGRATION)
EQUIV. WEIGHT FLOW	156.4511	

MEASURING PLANE									
IMMERSION (IN.)	0.3100	0.6400	0.9600	1.8100	3.0200	4.4300	5.3600	5.6800	5.9500
TOTAL PRESSURE	23.5112	23.1981	23.0822	22.0953	22.1088	23.1709	22.7276	22.3282	22.2889
STATIC PRESSURE	16.2806	16.1139	16.5559	16.6982	16.6621	16.6131	16.2163	16.0774	15.8915
WEDGE PRESSURE	16.4341	16.2637	16.6872	16.7972	16.7626	16.7451	16.3484	16.2024	16.0215
TOTAL TEMPERATURE	613.3772	603.7141	601.6620	610.4100	597.5563	596.5740	592.0077	592.1519	592.5302
ANGLE (DEG.)	26.9306	25.4184	27.0726	34.7721	34.6042	35.4861	35.9186	37.2487	40.6881
MACH NO.	0.7442	0.7409	0.7059	0.6456	0.6488	0.7063	0.7116	0.7015	0.7124
ABSOLUTE VELOCITY	856.3588	845.6392	808.6366	750.6247	746.3499	807.2082	809.5151	799.4248	811.3026
SWIRL VELOCITY	386.7258	362.0139	367.2415	427.7934	423.8388	467.1537	470.9437	478.4891	522.7363
AXIAL VELOCITY	761.2714	761.7710	718.5003	616.1555	614.2944	655.2646	650.1405	629.2776	607.9945
WEIGHT FLOW	17.0141	11.3670	19.0204	26.3399	30.7273	26.2003	12.3929	5.2968	7.4580

CALCULATING PLANE									
ANGLE (DEG.)	27.1531	25.3814	26.7051	33.9194	33.0698	33.8224	34.1292	35.4102	38.6874
MACH NO.	0.7389	0.7428	0.7176	0.6626	0.6776	0.7327	0.7336	0.7206	0.7287
SWIRL VELOCITY	388.1601	363.1142	368.6726	428.8628	423.8388	463.7042	464.9130	472.1247	514.2631
AXIAL VELOCITY	755.7988	764.3572	731.8618	636.7474	649.9160	691.0863	684.9159	663.0906	641.1922
ABSOLUTE VELOCITY	850.8016	847.6382	820.8994	768.8922	776.7496	834.5490	832.0855	819.2445	828.0465
WEIGHT FLOW	17.0192	11.3748	19.0224	26.3635	30.7192	26.0983	12.3939	5.2977	7.4553
MERIDIONAL VELOCITY	756.0938	764.9211	732.4520	637.1753	649.9200	692.8594	689.0782	668.5093	647.9793
STATIC TEMPERATURE	553.1531	543.8361	545.5846	561.2522	547.3825	538.8296	534.5712	536.5196	535.7331
STATIC PRESS. (ALT.)	16.3623	16.0847	16.3802	16.4596	16.2577	16.2171	15.8937	15.8013	15.6574
MCL INCIDENCE	-1.8362	-3.8798	-2.8933	2.9722	-0.5799	-0.3008	-0.0533	1.1896	4.4869
SUC SUR INCIDENCE	-8.2568	-10.3985	-9.4548	-3.2705	-6.6901	-6.4875	-6.4307	-5.2597	-2.0625
RADIUS RATIO	0.9766	0.9534	0.9295	0.8694	0.7839	0.6868	0.6223	0.5991	0.5810
STREAMLINE SLOPE	-1.6000	-2.2000	-2.2999	-2.1000	-0.2000	4.0999	6.2999	7.2999	8.3000

STATOR INCIDENCE PLOTS (UNIFORM INLET FLOW)

RDG NO= 128 PCT DES SPD=100.00 FAN INLET TOT TEMP= 518.688
OUTER WALL STATIC PRES= 17.480 HUB STATIC PRES= 17.350

PCT IM-MERSION	IN RADIUS	EX BL ANG	SOLIDITY	EX FLO ANG	INC ANG SS	IN VEL	IN TANG VELOCITY	IN STAT TEMP	IN STAT PRES	IN TOT PRES
.050	13.4800	-7.4000	1.0400	5.8700	-8.2600	850.8000	388.2000	553.1000	16.4000	23.5100
.100	13.1600	-7.5000	1.0600	5.7200	-10.4000	847.6000	363.1000	543.8000	16.0800	23.2000
.150	12.8300	-7.6000	1.0900	4.2300	-9.5000	820.9000	368.7000	545.6000	16.3800	23.0800
.282	12.0000	-8.4000	1.1700	4.6600	-3.3000	768.9000	428.9000	561.3000	16.4600	22.0900
.470	10.8200	-10.1000	1.3000	2.2100	-7.0000	776.7000	423.8000	547.4000	16.2600	22.1100
.689	9.4800	-9.8000	1.4700	2.7900	-6.5000	834.5000	463.7000	538.8000	16.2200	23.1700
.850	8.5900	-9.2000	1.6200	1.8200	-6.4000	832.1000	464.9000	534.6000	15.8900	22.7200
.900	8.2700	-9.1000	1.6700	1.9100	-5.3000	819.2000	472.1000	536.5000	15.8000	22.3200
.937	8.0200	-9.0000	1.7300	2.8400	-2.1000	828.0000	514.3000	535.7000	15.6600	22.2900

PCT IMMERSION	EX RADIUS	EX TOT TEMP	EX TOT PRES
.0500	13.4700	608.2600	21.8600
.1000	13.1500	605.9200	22.7100
.1500	12.8400	601.5700	22.8700
.2822	11.9700	602.0200	21.7500
.4702	10.8300	594.2600	21.8100
.6887	9.5700	592.6000	22.8200
.8500	8.6700	589.7200	22.0400
.9000	8.4000	589.6700	21.4400
.9372	8.1200	590.7600	20.3500

PCT IMMERS	DIF FACT	LOSS COEF	LOSS PARAM	POLY EFF	DEV ANG	EX MACH NO	EX COR VEL	EX COR AX VELOCITY	EX COR TANG VELOCITY
.0500	.3894	.2321	.1110	.5829	10.2700	.5749	673.1107	669.5813	68.8402
.1000	.3062	.0688	.0323	.7125	10.2200	.6241	725.3439	721.7323	72.2929
.1500	.2835	.0313	.0143	.8882	8.8300	.6332	732.4767	730.4814	54.0277
.2822	.3438	.0604	.0257	2.3821	10.0600	.5707	665.0389	662.8406	54.0295
.4702	.3386	.0513	.0197	1.0990	9.3100	.5762	666.7652	666.2693	25.7119
.6887	.2995	.0504	.0171	1.1352	9.5900	.6355	729.4506	728.5860	35.5063
.8500	.3430	.0996	.0307	.8453	8.0200	.5934	682.7746	682.4301	21.6847
.9000	.3775	.1350	.0404	.7872	8.0100	.5573	643.7308	643.3732	21.4553
.9372	.4903	.2926	.0845	.5611	8.8400	.4823	561.6673	560.9774	27.8290

PCT IMMERS	EX STAT PRES
.0500	17.4727
.1000	17.4658
.1500	17.4590
.2822	17.4401
.4702	17.4152
.6887	17.3878
.8500	17.3682
.9000	17.3623
.9372	17.3562

ROTOR INLET TRAVERSE PLANE READING NUMBER 113 TIME 13H 45M 6S UNIFORM INLET FLOW STATOR ANGLE 3.

DISTORTION INDEX 0.000

SPEED (RPM)	14050.4546	
ACTUAL ORIFICE FLOW	156.9819	
THETA	1.0041	
DELTA	0.9891	
MASS AVERAGED PT	14.5369	(14.6960)
MASS AVERAGED TT	520.8335	(518.6881)
TOTAL WEIGHT FLOW	162.0186	(PROBE INTEGRATION)
EQUIV. WEIGHT FLOW	164.1294	
EQUIV. SPEED	14021.4861	
PERCENT SPEED	109.7056	

PROBE TYPE - NASA 4 PARAMETER		LOCATION - STA 5.5, 328 DEG.							
IMMERSION(IN.)	0.4000	0.8400	1.2900	2.3600	3.8700	5.6100	6.9300	7.4300	7.9400
TOTAL PRESSURE	14.5525	14.7012	14.7094	14.7379	14.7362	14.7087	14.6949	14.6868	14.5821
STATIC PRESSURE	10.4055	10.1284	9.9282	9.6352	9.9307	10.4178	10.5626	10.8008	11.0422
WEDGE PRESSURE	11.0438	10.9340	10.8251	10.6814	10.8362	11.1035	11.1849	11.3395	11.4766
TOTAL TEMPERATURE	518.6683	519.2212	518.2046	519.5922	518.8502	518.6365	517.7161	517.7543	517.5172
ANGLE (DEG.)	1.3998	2.0658	2.0448	2.0686	1.9440	1.9794	1.9029	1.5925	1.8953
APPARENT MACH NO.	0.6402	0.6642	0.6764	0.6939	0.6774	0.6466	0.6357	0.6191	0.5949
PROBE TYPE - NASA 2 PARAMETER		LOCATION - STA 5.5, 260 DEG.							
STATIC PRESSURE	11.1105	11.1087	10.9569	10.8845	10.8623	10.9911	11.2675	11.4005	11.4823
WEDGE PRESSURE	11.1641	11.1656	11.0176	10.9476	10.9259	11.0510	11.3205	11.4502	11.5282
ANGLE (DEG.)	2.2857	2.9810	2.9835	4.1391	5.2864	5.7225	6.1372	6.9391	6.2421
APPARENT MACH NO.	0.6270	0.6393	0.6559	0.6656	0.6678	0.6522	0.6219	0.6070	0.5891
MEASURING PLANE									
MACH NO.	0.6329	0.6454	0.6624	0.6724	0.6746	0.6587	0.6277	0.6125	0.5943
ABSOLUTE VELOCITY	680.0249	692.4010	709.1612	718.9621	721.1467	705.4915	674.7888	659.5752	641.3238
SWIRL VELOCITY	16.1405	24.4154	24.9089	25.8196	24.4629	24.2064	21.7141	17.4969	19.8689
WEIGHT FLOW	15.7767	11.1977	18.6869	29.8088	33.2933	26.1862	12.8229	6.2906	7.9056
AXIAL VELOCITY	660.4916	676.8491	697.6321	714.8201	720.6921	700.4034	653.5426	629.3438	600.4219
CALCULATING PLANE									
ANGLE (DEG.)	1.1765	1.7274	1.7433	1.8438	1.7363	1.7415	1.5855	1.2965	1.5120
SWIRL VELOCITY	16.4174	24.7565	25.1922	26.0317	24.4402	23.9410	21.1377	16.8644	18.9349
AXIAL VELOCITY	798.3661	819.8843	826.6786	807.6267	805.2105	786.4148	762.1417	744.1344	716.3309
MERIDONAL VELOCITY	816.2021	831.5289	834.3986	810.2365	805.2154	790.4613	778.3127	770.3845	757.6061
ABSOLUTE VELOCITY	817.3873	832.9083	835.7859	811.6544	806.5835	791.8265	779.6194	771.6029	758.8989
MACH NO.	0.7748	0.7913	0.7944	0.7687	0.7633	0.7478	0.7350	0.7266	0.7134
WEIGHT FLOW	15.7774	11.1998	18.6900	29.8143	33.3085	26.1982	12.8284	6.2930	7.9088
WHEEL SPEED	1711.8206	1663.2135	1614.6542	1487.8001	1317.5890	1115.9601	968.7597	914.8378	859.9238
RELAT. TANG. VELOC.	1695.4030	1638.4569	1589.4618	1461.7682	1293.1486	1092.0189	947.6219	897.9731	840.9888
RELATIVE FLOW ANGLE	64.2931	63.0921	62.3027	61.0012	58.0905	54.1011	50.6028	49.3734	47.9860
RELATIVE VELOCITY	1881.6417	1837.3838	1795.1626	1671.3014	1523.3528	1348.0853	1226.2780	1183.1518	1131.9138
RELATIVE MACH NO.	1.7836	1.7457	1.7063	1.5829	1.4417	1.2731	1.1561	1.1142	1.0641
MCL INCIDENCE	2.0931	1.8921	1.8026	2.6012	1.9905	1.8011	2.2028	1.3733	0.0860
SURFACE INCIDENCE	-0.1068	-0.1078	-0.2972	0.2012	-0.4094	-0.8988	-1.4971	-2.4265	-4.0139
RELATIVE TOTAL PRESS	62.2699	58.7676	54.6095	45.1163	36.6781	29.3720	25.8233	24.7808	23.4645
STATIC TEMPERATURE	463.0207	461.3795	460.0751	464.6261	464.6453	466.4179	467.1839	468.2522	469.6535
RELAT. TOTAL TEMP.	757.9130	742.8588	728.2475	697.6830	657.9940	617.7734	592.2039	584.6419	576.1326
STATIC PRESS.(ALT.)	9.7847	9.7262	9.7022	9.9676	10.0180	10.1480	10.2604	10.3344	10.3851
RADIUS RATIO	0.9736	0.9464	0.9179	0.8469	0.7495	0.6347	0.5505	0.5196	0.4885
STREAMLINE SLOPE	-12.0000	-9.6000	-7.8000	-4.6000	0.2000	5.8000	11.7000	15.0000	19.0000

ROTOR EXIT TRAVERSE PLANE READING NUMBER 113 TIME 13H 45M 6S UNIFORM INLET FLOW STATOR ANGLE 3.00

MASS AVERAGED PT	24.0224	(24.2852)
MASS AVERAGED TT	623.0958	(620.5292)
TOTAL WEIGHT FLOW	160.9256	(PROBE INTEGRATION)
CORR. TOTAL FLOW	163.0222	

PROBE TYPE - NASA 4 PARAMETER		LOCATION - STA 9.0, 104 DEG.							
IMMERSION (IN.)	0.3100	0.6400	0.9600	1.8100	3.0200	4.4300	5.3600	5.6800	5.9500
TOTAL PRESSURE	25.4053	25.1522	24.7905	23.4189	23.5862	24.8313	24.2911	23.9245	23.1655
STATIC PRESSURE	16.9344	16.7419	16.4839	16.1928	16.2026	16.7684	16.3994	16.1412	15.7990
WEDGE PRESSURE	18.3524	18.1507	17.8761	17.3794	17.4190	18.1087	17.7114	17.4356	17.0172
TOTAL TEMPERATURE	638.6489	622.7702	621.7797	627.8033	619.2456	613.8166	607.2325	606.1861	605.8663
ANGLE (DEG.)	28.8622	28.0580	28.4066	35.5606	38.1480	37.9985	37.9035	39.4771	45.0045
APPARENT MACH NO.	0.6981	0.6992	0.7000	0.6672	0.6728	0.6873	0.6874	0.6880	0.6789

PROBE TYPE - NASA 2 PARAMETER		LOCATION - STA 9.0, 300 DEG.							
STATIC PRESSURE	16.8648	17.3014	17.2975	17.5073	17.3465	17.1846	16.9882	16.7869	16.6967
WEDGE PRESSURE	17.0571	17.4697	17.4548	17.6181	17.4668	17.3472	17.1411	16.9356	16.8259
ANGLE (DEG.)	17.5977	14.6672	20.9041	27.7280	33.9341	33.0457	32.3739	32.5843	32.6544
APPARENT MACH NO.	0.7768	0.7411	0.7264	0.6511	0.6696	0.7348	0.7239	0.7204	0.6918

MEASURING PLANE									
MACH NO.	0.7885	0.7514	0.7362	0.6586	0.6776	0.7449	0.7336	0.7301	0.7005
ABSOLUTE VELOCITY	920.7928	870.5862	854.8468	775.0001	790.6855	858.1076	842.5896	838.1477	807.2509
SWIRL VELOCITY	443.2221	408.4648	405.8264	450.4036	488.3849	526.7711	513.6032	527.2889	565.0396
WEIGHT FLOW	17.9258	11.8220	20.0442	27.3167	31.1914	27.1780	12.8034	5.4926	7.0429
AXIAL VELOCITY	804.1523	766.3390	750.3544	630.0344	621.7885	674.2742	659.5516	640.1763	564.9537

CALCULATING PLANE									
SWIRL VELOCITY	440.2934	406.0041	403.9447	449.2830	488.8367	531.2878	520.9755	536.4936	578.2311
AXIAL VELOCITY	744.4766	714.1572	701.8780	603.2274	600.6652	644.7006	621.3003	599.3030	530.5046
ABSOLUTE VELOCITY	873.9841	827.4531	814.0418	753.3815	775.3184	838.6577	820.8863	817.5110	799.1078
MERIDIONAL VELOCITY	753.9661	719.9933	705.7442	603.7571	600.7969	647.9042	633.3625	615.8197	550.5269
ANGLE (DEG.)	30.5671	29.5843	29.8861	36.6335	39.0931	39.4480	39.9355	41.7875	47.4112
MACH NO.	0.7438	0.7103	0.6975	0.6387	0.6633	0.7262	0.7128	0.7102	0.6927
WEIGHT FLOW	17.9262	11.8299	20.0451	27.3438	31.2166	27.1997	12.8190	5.4934	7.0514
WHEEL SPEED	1666.5474	1624.0794	1584.0501	1474.3528	1322.4830	1141.6567	1023.8721	982.1952	944.4464
RELAT. TANG. VELOC.	1226.2539	1218.0752	1180.1053	1025.0698	833.6460	610.3689	502.8966	445.7017	366.2154
RELATIVE FLOW ANGLE	58.4148	59.4132	59.1193	59.5025	54.2204	43.2914	38.4501	35.8954	33.6323
RELATIVE VELOCITY	1439.5009	1414.9547	1375.0354	1189.6596	1027.5809	890.1290	808.7354	760.1866	661.2059
RELATIVE MACH NO.	1.2252	1.2147	1.1783	1.0087	0.8791	0.7708	0.7022	0.6604	0.5732
DEVIATION	2.4148	3.1132	3.2193	8.3025	7.2204	4.5914	10.5501	12.9954	15.0323
AIR TURNING ANGLE	5.8782	3.6788	3.1833	1.4987	3.8701	10.8096	12.1527	13.4779	14.3536
REL. MACH NO.(WHL.)	1.2358	1.2169	1.1976	1.1404	1.0525	0.9374	0.8578	0.8282	0.8021
IDEAL PRESS. RATIO	0.9424	0.9504	0.9614	0.9834	1.0057	1.0276	1.0549	1.0650	1.0790
ROTOR PRESS. RATIO	1.7457	1.7108	1.6853	1.5890	1.6005	1.6882	1.6530	1.6289	1.5886
ROTOR TEMP. RATIO	1.2313	1.1994	1.1998	1.2082	1.1934	1.1835	1.1729	1.1707	1.1707
ADIABATIC EFFY.	0.7429	0.8288	0.8021	0.6769	0.7411	0.8770	0.8910	0.8738	0.8263
POLYTR. EFFICIENCY	0.7621	0.8412	0.8160	0.6971	0.7576	0.8857	0.8984	0.8822	0.8372
TOTAL LOSS COEFF.	0.1830	0.1129	0.1334	0.2361	0.1996	0.1072	0.1033	0.1243	0.1818
SHOCK LOSS COEFF.	0.0182	0.0173	0.0162	0.0134	0.0136	0.0657	0.0355	0.0261	0.0166
PROFILE LOSS COEFF.	0.1648	0.0955	0.1172	0.2227	0.1859	0.0415	0.0678	0.0982	0.1651
TOTAL LOSS PARAM.	0.0292	0.0173	0.0205	0.0353	0.0337	0.0218	0.0217	0.0263	0.0387
PROFILE LOSS PARAM.	0.0263	0.0146	0.0180	0.0333	0.0314	0.0084	0.0142	0.0208	0.0351
ROTOR DIFFUS. FACT.	0.3039	0.2939	0.2996	0.3653	0.4170	0.4500	0.4573	0.4798	0.5522
STATIC PRESS.(ALT.)	17.6023	17.9706	17.9162	17.8012	17.5618	17.4854	17.3157	17.0933	16.8120
RADIUS RATIO	0.9775	0.9531	0.9287	0.8656	0.7759	0.6696	0.6000	0.5756	0.5534
STREAMLINE SLOPE	-9.1000	-7.3000	-6.0000	-2.4000	1.2000	5.7000	11.2000	13.3000	15.5000
SOLIDITY	1.6400	1.6580	1.6700	1.6940	1.7300	1.7880	1.8530	1.9100	1.9540
METAL CAMBER	6.2000	4.9000	4.6000	7.2000	9.1000	13.6000	20.5000	25.1000	29.3000

STATOR INLET TRAVERSE PLANE READING NUMBER 113 TIME 13H 45M 6S UNIFORM INLET FLOW STATOR ANGLE 3.

MASS AVERAGED PT	24.0230	(24.2858)
MASS AVERAGED TT	623.1103	(620.5437)
TOTAL WEIGHT FLOW	160.7570	(PROBE INTEGRATION)
EQUIV. WEIGHT FLOW	162.8514	

MEASURING PLANE									
IMMERSION (IN.)	0.3100	0.6400	0.9600	1.8100	3.0200	4.4300	5.3600	5.6800	5.9500
TOTAL PRESSURE	25.4053	25.1522	24.7905	23.4188	23.5862	24.8313	24.2911	23.9245	23.1655
STATIC PRESSURE	16.8648	17.3014	17.2975	17.5073	17.3465	17.1846	16.9832	16.7869	16.6967
WEDGE PRESSURE	17.0571	17.4697	17.4548	17.6181	17.4668	17.3471	17.1410	16.9356	16.8259
TOTAL TEMPERATURE	638.6488	622.7701	621.7796	627.8032	619.2455	613.8165	607.2324	606.1860	605.8662
ANGLE (DEG.)	28.8622	28.0580	28.4066	35.5606	38.1480	37.9985	37.9035	39.4771	45.0045
MACH NO.	0.7885	0.7514	0.7362	0.6586	0.6776	0.7449	0.7336	0.7301	0.7005
ABSOLUTE VELOCITY	920.7928	870.5861	854.8470	775.0001	790.6854	858.1076	842.5895	838.1476	807.2509
SWIRL VELOCITY	443.2221	408.4647	405.8265	450.4034	488.3848	526.7711	513.6030	527.2887	565.0396
AXIAL VELOCITY	804.1525	766.3388	750.3546	630.0345	621.7886	674.2742	659.5517	640.1764	564.9538
WEIGHT FLOW	17.9258	11.8220	20.0442	27.3167	31.1914	27.1780	12.8054	5.4926	7.0429
CALCULATING PLANE									
ANGLE (DEG.)	29.0971	28.0165	27.9830	34.7004	36.5200	36.0809	36.3797	37.5746	43.3698
MACH NO.	0.7830	0.7535	0.7496	0.6758	0.7058	0.7752	0.7487	0.7489	0.7069
SWIRL VELOCITY	444.8660	409.7062	407.4080	451.5293	488.3848	522.8813	507.0260	520.2753	555.8805
AXIAL VELOCITY	798.3663	769.0157	765.7759	651.0868	658.5366	716.5558	687.2261	675.2146	587.4515
ABSOLUTE VELOCITY	915.0888	872.7280	868.8340	793.5136	820.6767	889.3444	858.1968	857.5864	814.0310
WEIGHT FLOW	17.9343	11.8300	20.0566	27.3338	31.2072	27.1840	12.7254	5.4977	6.9876
MERIDIONAL VELOCITY	798.6779	769.5830	766.3933	651.5244	658.5407	718.3944	691.4014	680.7325	593.6697
STATIC TEMPERATURE	569.2135	559.4969	559.1893	575.4707	563.3248	548.1555	546.1783	545.2112	550.9521
STATIC PRESS.(ALT.)	16.9555	17.2678	17.0822	17.2519	16.9197	16.6953	16.7503	16.4951	16.6002
MCL INCIDENCE	0.1084	-1.2428	-1.6144	3.7537	2.8702	1.9635	2.2108	3.3716	9.2189
SUC SUR INCIDENCE	-6.3128	-7.7634	-8.1769	-2.4895	-3.2399	-4.2290	-4.1802	-3.0953	2.6198
RADIUS RATIO	0.9766	0.9534	0.9295	0.8694	0.7839	0.6868	0.6223	0.5991	0.5810
STREAMLINE SLOPE	-1.6000	-2.2000	-2.2999	-2.1000	-0.2000	4.0999	6.2999	7.2999	8.3000

STATOR INCIDENCE PLOTS (UNIFORM INLET FLOW)

RDG NO= 113 PCT DES SPD=110.00 FAN INLET TOT TEMP= 518.688
OUTER WALL STATIC PRES= 18.550 HUB STATIC PRES= 18.380

PCT IM- MERSION	IN RADIUS	EX BL ANG	SOLIDITY	EX FLO ANG	INC ANG SS	IN VEL	IN TANG VELOCITY	IN STAT TEMP	IN STAT PRES	IN TOT PRES
.050	13.4800	-7.4000	1.0400	4.4800	-6.3100	915.0000	444.9000	569.2000	17.0000	25.4000
.100	13.1600	-7.5000	1.0600	4.8200	-7.8000	872.7000	409.7000	559.5000	17.2700	25.1500
.150	12.8300	-7.6000	1.0900	3.8200	-8.2000	868.8000	407.4000	559.2000	17.0800	24.7900
.282	12.0000	-8.4000	1.1700	2.7200	-2.5000	793.5000	451.5000	575.5000	17.2500	23.4200
.470	10.8200	-10.1000	1.3000	2.1900	-3.2400	820.7000	488.4000	563.3000	16.9200	23.5900
.689	9.4800	-9.8000	1.4700	-.1000	-4.2300	889.3000	522.9000	548.2000	16.7000	24.8300
.850	8.5900	-9.2000	1.6200	2.1700	-4.1800	858.2000	507.0000	546.2000	16.7500	24.2900
.900	8.2700	-9.1000	1.6700	1.9400	-3.1000	857.6000	520.3000	545.2000	16.5000	23.9200
.937	8.0200	-9.0000	1.7300	1.9800	2.6200	814.0000	555.9000	551.0000	16.6000	23.1700

PCT IMMERSION	EX RADIUS	EX TOT TEMP	EX TOT PRES
.0500	13.4700	627.7500	23.3900
.1000	13.1500	625.0800	24.6100
.1500	12.8400	621.9700	24.3100
.2822	11.9700	617.5200	23.0400
.4702	10.8300	612.3400	22.9300
.6887	9.5700	608.2400	24.2500
.8500	8.6700	603.3500	23.0900
.9000	8.4000	603.1100	22.6000
.9372	8.1200	604.4400	21.5200

PCT IMMERS	DIF FACT	LOSS COEF	LOSS PARAM	POLY EFF	DEV ANG	EX MACH NO	EX COR VEL	EX COR AX VELOCITY	EX COR TANG VELOCITY
.0500	.4446	.2393	.1147	.7862	8.8800	.5858	696.0035	693.8770	54.3656
.1000	.3106	.0685	.0322	.6763	9.3200	.6497	764.6463	761.9422	64.2499
.1500	.3285	.0623	.0285	.8072	8.4200	.6355	747.3465	745.6861	49.7899
.2822	.3798	.0616	.0263	2.5797	8.1200	.5690	671.6777	670.9210	31.8745
.4702	.4074	.0990	.0380	1.1559	9.2900	.5649	664.3681	663.8829	25.3878
.6887	.3647	.0713	.0243	1.1037	6.7000	.6387	742.4022	742.4010	-1.2957
.8500	.3864	.1592	.0491	.7753	8.3700	.5786	674.4707	673.9870	25.5385
.9000	.4225	.1779	.0532	.7375	8.0400	.5503	643.2714	642.9027	21.7766
.9372	.4952	.2511	.0725	.6137	7.9800	.4794	564.8905	564.5533	19.5173

PCT IMMERS	EX STAT PRES
.0500	18.5405
.1000	18.5314
.1500	18.5226
.2822	18.4978
.4702	18.4653
.6887	18.4294
.8500	18.4038
.9000	18.3961
.9372	18.3881

APPENDIX B

NOMENCLATURE

g	Gravitational acceleration, ft/sec^2 (m/sec^2)
K	Gladstone-Dale constant, cm^3/g
M	Mach number
msec	Millisecond
N	Rotational speed, rpm (rad/sec)
nsec	Nanosecond
n	Refractive index
P	Total pressure, psia (N/cm^2)
p	Static pressure, psia (N/cm^2)
S	Sensitivity of an interferometer in waves
T	Temperature, ^oF (^oK)
V	Air velocity, ft/sec (m/sec)
W	Airflow, lb/sec (kg/sec)
Z	Axial distance, in. (cm)
δ	Ratio of total pressure to NASA standard sea level pressure of 14.696 psia (10.133 N/cm^2)
η	Adiabatic efficiency

$$\text{rotor} = \frac{(P_{T9}/P_{T5})^{\gamma-1/\gamma} - 1}{(T_9/T_5) - 1}$$

$$\text{stage} = \frac{(P_{T12}/P_{T5})^{\gamma-1/\gamma} - 1}{(T_{12}/T_5) - 1}$$

λ	Wavelength of light

μ	Micron
μF	Capacitance, microfarads
μsec	Microsecond
ρ	Fluid density, lb/ft^3 (Kg/m^3)
∅	Angle of scattered light, deg
τ	Time, nsec
Ω	Electrical resistance, ohms

Subscripts/superscripts

5	Rotor inlet plane
9	Rotor exit plane
12	Stage exit instrumentation plane
i	Initial
f	Final
'	Relative to rotating part
des	Design

REFERENCES

1. Wuerker, R. F.; and Heflinger, L.O.: Pulsed Laser Holography, published in Robertson, E. R.; and Harvey, J. M.: The Engineering Uses of Holography, Cambridge University Press, 1970, pp. 104-110.

2. Wuerker, R. F.; Matthews, B. J.; and Briones, R. A.: Producing Holograms of Reacting Sprays in Liquid Propellant Rocket Engines, Final Report, JPL Contract No. 952023 (NAS 7-100), July 31, 1968.

3. Wuerker, R. F.; and Matthews, B. J.: Laser Holocamera Droplet Measuring Device, Final Technical Report, AFRPL-TR-69-204, Nov. 1969, pp. 1-12.

4. Heflinger, L. O.; and Brooks, R. E.: Holographic Instrumentation Studies, Final Report, NAS2-4992, Dec. 1970.

5. Wright, L. C.; Vitale, N. G.; Ware, T. C.; and Erwin, J. R.: High Tip Speed, Low-Loading Transonic Fan Stage - Part I Aerodynamic and Mechanical Design, NASA CR-121095, AiResearch 72-8421, April 1973.

6. Ware, T. C.; Kobayashi, R. J.; and Jackson, R. J.: High-Tip-Speed Low-Loading Transonic Fan Stage, Part II - Final Report, NASA CR-121263, AiResearch 73-9488, Feb. 1974

7. Wuerker, R. F.: Instruction Manual for Ruby Laser Holographic Illuminator, Report prepared under Contract F04611-69-C-0015, Feb. 1970.

8. Heflinger, L. O.; Wuerker, R. F.; and Brooks, R. E.: Holographic Interferometry, J. Appl. Phys., 37, 642-649, Feb. 1966.

9. Wuerker, R. F.: Holographic Interferometry, Proceedings of SPIE, Developments in Holography, Seminar-in-Depth, SPIE Seminar Proceedings, Vol. 25, Society of Photo-optical Instrumentation Engineers, Redondo Beach, CA., 1971.

10. O'Keefe, J. D.; Aprahamian, R.; Tierney, W. S.; and Wright, J. E.: Holographic Study of Electron Beam Induced Front Surface Effects, AT-72-3, Air Force Weapons Laboratory Contract F29601-71-C-0108, June 6, 1972.

11. McDowell, C. N.; et al.: Use of Laser-Triggered Spark Gap to Narrow a Q-Switched Laser Pulse, Rev. Sci. Instru., 42, 163-164, Jan. 1971.

DISTRIBUTION LIST

			Copies
1.	NASA-Lewis Research Center 21000 Brookpark Road Cleveland, Ohio 44135		
	Attention: Report Control Office	MS 5-5	1
	Technical Utilization Office	MS 3-19	1
	Library	MS 60-3	2
	Fluid System Components Div.	MS 5-3	1
	Compressor Branch	MS 5-9	5
	Dr. S. C. Himmel	MS 3-5	1
	R. S. Ruggeri	MS 5-9	1
	M. J. Hartmann	MS 5-9	1
	W. A. Benser	MS 5-9	1
	D. M. Sandercock	MS 5-9	1
	L. J. Herrig	MS 501-4	1
	T. F. Gelder	MS 5-9	1
	C. L. Ball	MS 5-9	1
	L. Reid	MS 5-9	1
	L. W. Schopen	MS 500-206	1
	S. Lieblein	MS 501-5	1
	C. L. Meyer	MS 60-4	1
	J. H. Povolny	MS 60-4	1
	W. L. Beede	MS 5-3	1
	C. H. Voit	MS 5-3	1
	E. E. Bailey	MS 5-9	3
	D. R. Buchele	MS 77-1	1
	N. C. Wenger	MS 77-1	1
	N. T. Musial	MS 500-311	1
2.	NASA Scientific and Technical Information Facility P. O. Box 33 College Park, Maryland 20740		
	Attention: Acquisitions Branch		10
3.	NASA Headquarters Washington, D. C. 20546		
	Attention: N. F. Rekos (RLC)		1
4.	U. S. Army Aviation Material Laboratory Fort Eustes, Virginia 23604		
	Attention: John White		1
5.	Headquarters Wright-Patterson AFB, Ohio 45433		
	Attention: J. L. Wilkins, SESOS		1
	S. Kobelak, APTP		1
	R. P. Carmichael, SESSP		1

		Copies
6.	Department of the Navy Naval Air Systems Command Propulsion Division, AIR 536 Washington, D. C. 20360	1
7.	Department of Navy Bureau of Ships Washington, D. C. 20360 Attention: G. L. Graves	1
8.	NASA-Langley Research Center Technical Library Hampton, Virginia 23365 Attention: Mark R. Nichols	1
	John V. Becker	1
9.	The Boeing Company Commercial Airplane Group Attention: G. J. Schott Organization: G-8410, M. S. 7314 P. O. Box 3707 Seattle, Washington 98124	1
10.	Douglas Aircraft Company 3855 Lakewood Boulevard Long Beach, California 90801 Attention: J. E. Merriman Technical Information Center C1-250	1
11.	Pratt & Whitney Aircraft Florida Research & Development Center P. O. Box 2691 West Palm Beach, Florida 33402 Attention: J. Brent	1
	H. D. Stetson	1
	W. R. Alley	1
	R. E. Davis	1
	R. W. Rockenbach	1
	B. A. Jones	1
	J. A. Fligg	1

		Copies
12.	Pratt & Whitney Aircraft 400 Main Street East Hartford, Connecticut 06108	
	Attention: R. E. Palatine	1
	T. G. Slaiby	1
	H. V. Marman	1
	M. J. Keenan	1
	B. B. Smyth	1
	A. A. Mikolajczak	1
	Library (UARL)	1
	W. M. Foley (UARL)	1
	W. G. Alwang	1
	R. J. Burr	1
	R. G. Hantman	1
	M. C. Williams	1
13.	Allison Division, GMC Department 8894, Plant 8 P. O. Box 894 Indianapolis, Indiana 46206	
	Attention: J. N. Barney U-26	1
	G. E. Holbrook T-22	1
	J. A. Korn T-26	1
	R. F. Alverson U-28	1
	Library S-5	1
	A. Medlock U-28	1
	P. Tramm J-23	1
14.	Northern Research and Engineering 219 Vassar Street Cambridge, Massachusetts 02139	
	Attention: K. Ginwala	1
15.	General Electric Company Flight Propulsion Division Cincinnati, Ohio 45215	
	Attention: W. G. Cornell K-49	1
	D. Prince H-79	1
	J. F. Klapproth H-42	1
	J. W. McBride H-44	1
	L. H. Smith H-50	1
	Technical Information Ctr. N-32	1
	Marlen Miller H-50	1
	C. C. Koch H-79	1

		Copies
16.	General Electric Company 1000 Western Avenue West Lynn, Massachusetts 01905	
	Attention: D. P. Edkins - Bldg. 2-40	1
	F. F. Ehrich - Bldg. 2-40	1
	L. H. King - Bldg. 2-40	1
	R. E. Neitzel - Bldg. 2-40	1
	Dr. C. W. Smith -- Library Bldg. 2-40M	1
17.	Curtiss-Wright Corporation Wright Aeronautical Wood-Ridge, New Jersey 07075	
	Attention: S. Lombardo	1
	G. Provenzale	1
18.	AiResearch Manufacturing Company 402 South 36th Street Phoenix, Arizona 85034	
	Attention: Robert O. Bullock	1
	W. F. Waterman	1
	Jack Erwin	1
	Don Seyler	1
	Jack Switzer	1
	G. L. Perrone	1
19.	AiResearch Manufacturing Company 2525 West 190th Street Torrance, California 90509	
	Attention: R. J. Kobayashi	1
	Bob Carmody	1
	Library	1
	R. Jackson	1
20.	Union Carbide Corporation Nuclear Division Oak Ridge Gaseous Diffusion Plant P. O. Box "P" Oak Ridge, Tennessee 37830	
	Attention: R. G. Jordan	1
	D. W. Burton, K-1001, K-25	1
21.	Avco Corporation Lycoming Division 550 South Main Street Stratford, Connecticut 06497	
	Attention: Clause W. Bolton	1

		Copies
22.	Teledyne CAE 1330 Laskey Road Toledo, Ohio 43601 Attention: Eli H. Benstein Howard C. Walch	 1 1
23.	Solar San Diego, California 92112 Attention: P. A. Pitt J. Watkins	 1 1
24.	Goodyear Atomic Corporation Box 628 Piketon, Ohio 45661 Attention: C. O. Langebrake	 2
25.	Iowa State University of Science and Technology Ames, Iowa 50010 Attention: Professor George K. Serovy Dept. of Mechanical Engineering	 1
26.	Hamilton Standard Division of United Aircraft Corporation Windsor Locks, Connecticut 06906 Attention: Mr. Carl Rohrbach Head of Aerodynamics and Hydrodynamics	 1
27.	Westinghouse Electric Corporation Small Steam and Gas Turbine Engineering B-4 Lester Branch P. O. Box 9175 Philadelphia, Pennsylvania 19113 Attention: Mr. S. M. DeCorso	 1
28.	Williams Research Corporation P. O. Box 95 Walled Lake, Michigan 48088 Attention: J. Richard Joy Supervisor, Analytical Section	 1
29.	Lockheed Missile and Space Company P.O. Box 879 Mountain View, California 94040 Attention: Technical Library	 1

Copies

30. The Boeing Company
224 N. Wilkinson
Dayton, Ohio 45402
Attention: James D. Raisbeck — 1

31. Chrysler Corporation
Research Office
Dept. 9000
P. O. Box 1118
Detroit, Michigan 48231
Attention: James Furlong (418-19-40) — 1
Ronald Paripreen (418-38-31) — 1

32. Elliott Company
Jeannette, Pennsylvania 15644
Attention: J. Rodger Shields
Director-Engineering — 1

33. Dresser Industries Inc.
Clark Gas Turbine Division
16530 Peninsula Boulevard
P. O. Box 9989
Houston, Texas 77015
Attention: R. V. Reddy — 1

34. California Institute of Technology
Pasadena, California 91109
Attention: Professor Duncan Rannie — 1

35. Massachusetts Institute of Technology
Cambridge, Massachusetts 02139
Attention: Dr. J. L. Kerrebrock — 1

36. Caterpillar Tractor Company
Peoria, Illinois 61601
Attention: J. Wiggins — 1

37. Penn State University
Department of Aerospace Engineering
233 Hammond Building
University Park, Pennsylvania 16802
Attention: Professor B. Lakshminarayana — 1

38. Texas A&M University
Department of Mechanical Engineering
College Station, Texas 77843
Attention: Dr. Meherwan P. Boyce P.E. — 1

Copies

39. General Electric Co.
Building 37, Room 304
P. O. Box 43
Schenectady, New York 12301
Attention: Misuru Kurosaki 1

40. Naval Postgraduate School
Department of Aeronautics
Monterey, California 93940
Attention: Dr. Allen E. Fuhs 1

41. Calspan Corporation
P. O. Box 235
Buffalo, New York 14221
Attention: Dr. A. L. Russo 1